AMBIENT RESONANCE OF ROCK ARCHES

by

Alison Margaret Starr

A thesis submitted to the faculty of
The University of Utah
in partial fulfillment of the requirements for the degree of

Master of Science

in

Geophysics

Department of Geology and Geophysics

The University of Utah

August 2015

The University of Utah Graduate School

STATEMENT OF THESIS APPROVAL

The thesis of **Alison Margaret Starr**

has been approved by the following supervisory committee members:

Jeffrey R. Moore	, Chair	**04/13/2015** Date Approved
Michael S. Thorne	, Member	**04/13/2015** Date Approved
Keith D. Koper	, Member	**04/13/2015** Date Approved

and by **John M. Bartley** , Chair/Dean of

the Department/College/School of **Geology and Geophysics**

and by David B. Kieda, Dean of The Graduate School.

ABSTRACT

Resonant frequencies of structural elements are related to fundamental material properties of mass and stiffness, and monitoring over time can thus serve as an indirect indictor of internal mechanical change. Until now, however, this methodology has not been applied to natural rock structures such as arches and towers. We evaluated the resonance characteristics of four rock arches in southeastern Utah, combining in-situ ambient vibration measurements with numerical modal analysis. At each location, we measured the spectral and polarization attributes of ambient vibrations using up to two broadband seismometers. Ambient vibration spectra measured on the arches showed clear peaks at distinct frequencies (typically between 1-10 Hz), which we interpret as resonant frequencies, as opposed to the relatively flat spectra recorded on nearby bedrock. Polarization analysis helped us identify the orientations of vibration and explore resonant mode shapes. We then verified the measured resonant frequencies through 3D finite-element numerical modal analysis, and in most cases we were able to match the fundamental along with several higher-order modes. Repeat occupation and short-term continuous ambient vibration monitoring were aimed at assessing daily and seasonal changes in resonant frequencies, which in turn may provide evidence of internal mechanical change; Mesa Arch in Canyonlands National Park served as the main focus for our repeat measurements. Results revealed that minor, reversible changes in resonant frequencies can be created by thermal effects, i.e., changes in bulk material stiffness as the arch expands and contracts on daily and seasonal time scales. No irreversible change in the resonant frequency of Mesa Arch was detected over the period of this study. Our research provides the first step towards monitoring the long-term structural health of natural rock arches as they change through time or in the wake of a damaging event. We have shown that the resonance properties of natural rock arches can be evaluated from ambient seismic noise measurements and confirmed through experimental and numerical modal analysis. We have also shown that minor variations in resonant frequencies, which are related to environmental effects, can be expected and must be characterized in order to identify permanent change associated with internal damage.

TABLE OF CONTENTS

Chapters

Appendices

ACKNOWLEDGMENTS

I would like to thank Dr. Jeffrey Moore for serving as my advisor and providing continual support, encouragement, and guidance that led to the success of this project. I am also grateful to Dr. Michael Thorne and Dr. Keith Koper for giving their time as creators of the programs utilized in this research and for serving as committee members. I would like to further express my gratitude to Dr. Thorne for providing significant guidance in helping me understand the execution and application of the programs. I thoroughly enjoyed working with all of you and appreciate everything that you have taught me over the last two years. I would also like to acknowledge the University of Utah Center of High Performance Computing (CHPC) for computer resources and support.

Thank you to my field assistants: Jordan Culp and Ben White for being fearless and playing a huge role in the success of this project. Thank you to my office mates: Yao Yao, Oner Sufri, Kevin Kwong, Stephanie Whittaker, Jared Stein, Chase Batchelor, and Brendon Quirk for their helpful comments and continued support. Last but not least, thank you to my husband, Ryan Starr, and my family for their unconditional love and support.

This research was supported by the *Funding Incentive Seed Grant Program* sponsored by the University of Utah Research Foundation.

CHAPTER 1

INTRODUCTION

There are several thousand known natural rock arches in southeastern Utah, many of which are situated within Arches National Park. These features formed from millions of years of erosion and continue to erode today. Foos (1999) identified three stages of arch formation: 1) Development: characterized by a small window opening. 2) Growth: characterized by thinner more fragile spans with deteriorating supports. 3) Destruction: collapsed arches with only closely spaced pinnacles remaining. We are fortunate to witness thousands of arches during the peak of their formation in the development and growth stages, but their destruction is also inevitable.

The unexpected collapse of Wall Arch on August 5, 2008 highlighted the transience of natural rock arches, and emphasized the need for further scientific research into the processes leading to their destruction. Situated along the popular Devil's Garden trail in Arches National Park, the arch was a common destination for visitors. Images of the arch before collapse showed a relatively thick but awkward span, lacking the familiar upward convexity that lends arches their structural stability (Figure 1.1). The first observable sign of failure occurred in 1969 when a large slab broke free, but other than a few fresh facets indicating recent rockfall, there was no indication of impending collapse. No scientific data were available to quantitatively assess structural stability, and since most in-situ sensing approaches are invasive or destructive, monitoring structural change

Figure 1.1 Wall Arch in Arches National Park, Utah before and after its collapse in 2008 (Connors, 2008).

of natural features is not common in the preserved wilderness areas of national parks.

Wall Arch, however, was not the feature most commonly identified by park visitors as being the most precarious or fragile. Landscape Arch, located along the same trail, is North America's longest arch and is remarkably slender, measuring less than 2 m at its thinnest part. On September 1, 1991 after several days of rain, a 22-m slab of rock detached explosively from the underside of the span. Anecdotal evidence suggested that the increased weight of water-saturated sandstone resulted in sagging, which compressed the underside of the abutments generating the failure. Two additional slab failures in 1995, with a combined length of over 23 m, resulted in permanent closure of the loop trail that once led underneath the arch (Graham, 2004).

Furthermore, the aptly named Delicate Arch sits precariously along the edge of a large rock bowl, and is the most recognized freestanding arch in Arches National Park, if not the world. Delicate Arch is not attached to a fin or cliff, like a majority of the arches within the park; rather it sits atop two thinning pedestals whose connection to the overlying ridge is interrupted by a plane of weakness featuring clay-rich strata. The result is a precarious appearance, which frequently incites visitors to question its longevity. In the 1950s, park officials considered reinforcing this plane of weakness with a silicone epoxy, but eventually decided against such modifications ("Arches National Park," 2007).

Managers and visitors alike recognize that collapse is part of the natural cycle of arch formation and destruction, and are keenly interested in their respective rates. However, there is no published method to evaluate the *structural health* of these features as they change through time or in the wake of a damaging event. The goal of our study is to combine in-situ ambient vibration measurements with time-dependent modal analysis (analyzing resonant frequencies and mode shapes over time) to monitor the resonance characteristics of natural rock arches. This information will provide a deeper understanding of the dynamics of these spectacular features and may eventually aid in visitor safety and hazard assessments.

The field of structural health monitoring (SHM) has grown significantly in the past few decades and has recently gained popularity in the area of natural hazards research. Measurements of ambient or forced vibrations and time-dependent modal analysis form the basis of most SHM systems (Sohn et al., 2002). The ambient vibration method enables collecting seismic data without an additional vibration source. This involves processing seismic noise to retrieve dynamic parameters of a structure, in particular its resonant frequencies (Stubbs and McLamore, 1973). The technique offers the advantage of easy, noninvasive recording and relatively simple data processing, making it ideal for monitoring delicate natural features.

SHM methods are now commonly used in analysis of civil structures, such as bridges and buildings (Sohn et al., 2002, Clinton et al., 2006). Recently, however, the same techniques have been applied to unstable rock slopes. Burjánek et al. (2010) and Moore et al. (2011) performed seismic noise measurements to detect resonant frequencies of unstable rock masses in the Swiss Alps. Lévy et al. (2010) studied an unstable rock column in the French Alps using ambient seismic noise; analysis revealed clear resonant frequencies and continued monitoring showed a significant drop (~27%) in the first resonant frequency (fundamental frequency, *f1*) a few weeks before the column collapsed. Data also showed *f1* fluctuating over time, with these reversible changes attributed to thermal effects. This unique study showed that evidence of internal mechanical change can be obtained by measuring vibration parameters over time, and the addition of long-term monitoring assists in differentiating reversible versus irreversible (damage-related) signals (the latter also highlighted by Bottelin et al., 2013).

This study aims to measure the resonance characteristics and understand factors influencing the dynamic response of 10 natural rock features located in Southern Utah: Corona Arch, Double O Arch, Landscape Arch, Mesa Arch, Balanced Rock, Delicate Arch, Double Arch, Gemini Bridges, North Window Arch, and Surprise Arch (Figure 1.2). Each site was instrumented with up to two broadband seismometers in multiple configurations to record and analyze the spectral and polarization attributes of ambient vibrations. The primary sensor configuration utilizes one seismometer placed on the arch or tower and the other located at a distance of ~100 m for reference. Another method involves both sensors placed directly atop the arch. Initial and repeat measurements, ranging in duration from 1 h to 3 d, were aimed at assessing short- and long-term changes in resonance characteristics and to search for evidence of internal mechanical change. In

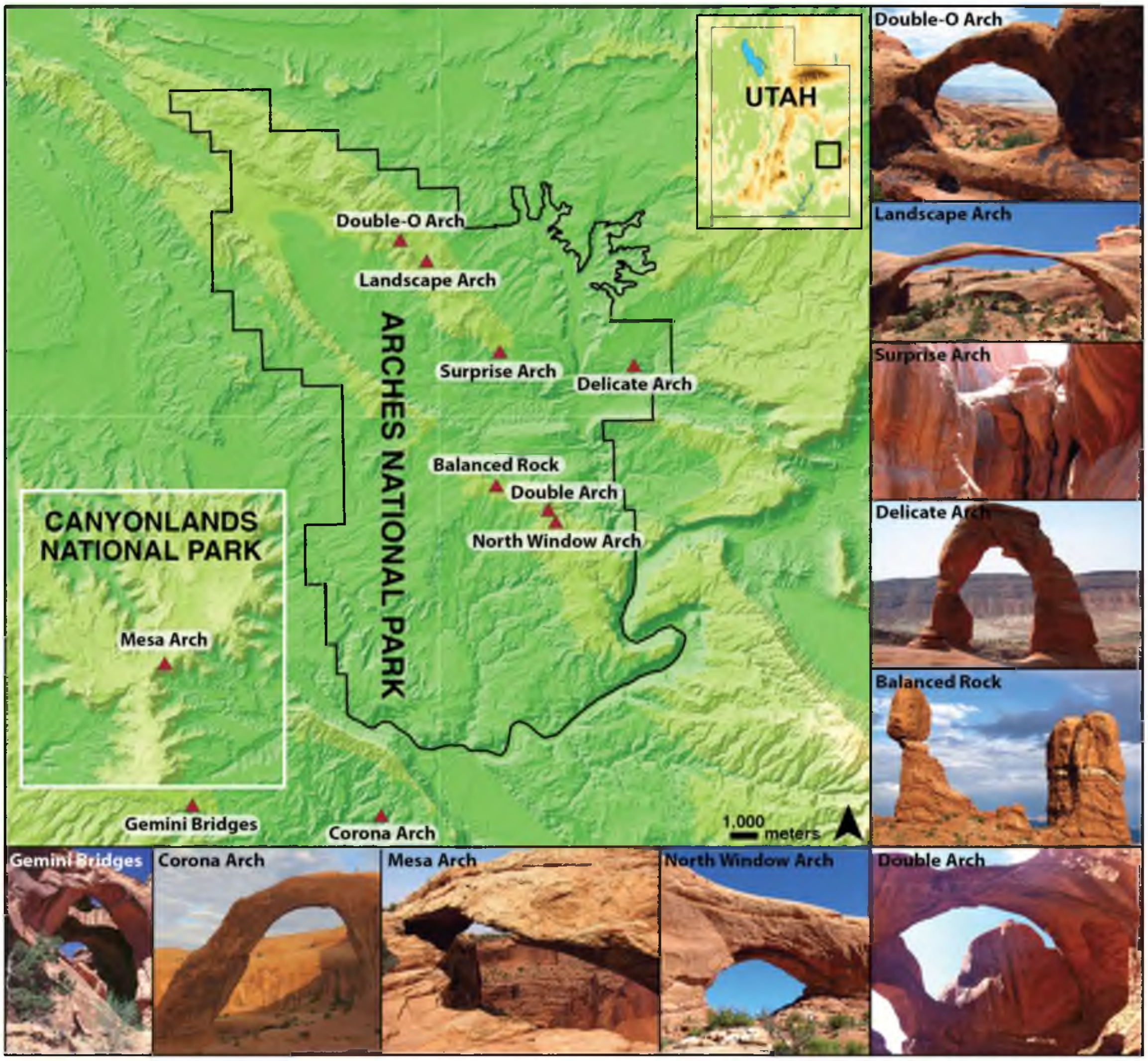

Figure 1.2 Map of the study region (location shown in inset) with surrounding images of the 10 study sites.

this thesis, I focus on four study sites where we generated optimal data sets: Corona Arch, Double O Arch, Landscape Arch, and Mesa Arch. Appendix A contains full data and analysis from all 10 study sites.

CHAPTER 2

STUDY AREA

The study area in southeastern Utah stretches from Arches National Park to Canyonlands National Park, with some sites on Bureau of Land Management land between the two parks (Figure 1.2). The geology of these sites is similar; they sit atop the Colorado Plateau with the Green River and the Colorado River cutting through the terrain, displaying the shared stratigraphic units (Table 2.1) as well as salt tectonic features (Foos, 1999).

2.1 Arches National Park

The greatest concentration of natural rock arches lies within Arches National Park. These features result from the area's climate, stratigraphy, and salt tectonics. The landscape is a result of a down-faulted basin, known as the Paradox Basin, which formed when deep-seated Precambrian faults ruptured during the Pennsylvanian (Baars, 1993). A shallow sea covered the region at this time and became trapped in the basin. As climate warmed, the sea evaporated, leaving behind 1200 to 2400 m thick salt deposits. The Paradox Basin is asymmetrical, with thicker deposits in the NE portion. This area is known as the Salt Valley Anticline and lies beneath Arches National Park (Cruikshank and Aydin, 1995). Overlying the salt deposits are Pennsylvanian and Permian aged sediments. Growth of salt structures, and the subsequent dissolution of salt, generated

Table 2.1 Description of the stratigraphic units of the Moab, Utah region (modified from Foos, 1999).

AGE	THICK. (m)	DESCRIPTION
Quaternary		Unconsolidated alluvium and terrace gravel, dune sand, and landslide deposits.
Tertiary		Quartz diorite porphyry.
Cretaceous	**61-366**	**Mancos Shale** Dark-gray to black fissile even-bedded shale containing fossiliferous sandy limestone in the lower part of unit. Forms a slope.
Cretaceous	**15-61**	**Dakota Sandstone** Brown massive to cross-bedded conglomerate and conglomeratic sandstone, locally contains green claystone lenses at base and dark-gray carbonaceous shale seams at top. Forms a cliff.
Unconformity		
Jurassic	**183-213**	**Morrison Formation** Varicolored shales and fine-grained sandstones, massive sandstones and shales. Forms a slope with scattered sandstone ledges.
Unconformity		
Jurassic		**Entrada Sandstone** Consists of the following three members:
	18-37	**Moab Tongue** Reddish-brown, thin-bedded, ripple-laminated muddy sandstones and siltstones. Forms a slope and short cliff.
	61-152	**Slick Rock** Pale orange, fine-grained massive, cross-bedded friable sandstone. Forms cliffs.
	12-72	**Dewey Bridge** Interbedded red siltstone and muddy sandstone.
Jurassic	**76-168**	**Navajo Sandstone** Pale orange, well sorted, fine- to medium-grained, massive, sandstone. Forms a cliff and hummocky knobs.
Triassic	**61-91**	**Kayenta Formation** Reddish-brown to lavender, fine- to medium-grained sandstone with subordinate siltstone, limestone, and shale interbeds. Divided into a lower cliff forming and an upper slope-forming unit.
Triassic	**76-137**	**Wingate Sandstone** reddish-brown, cross-bedded fine-grained, well-sorted sandstone. Forms a cliff.

Table 2.1 (continued)

AGE	THICK. (m)	DESCRIPTION
Triassic	**61-274**	**Chinle Formation** Variegated red, purple, green, and yellow bentonitic clayey sandstones and siltstones. Locally contains scattered ledges of conglomeratic sandstones. Generally forms a slope.
Unconformity		
Triassic	**0-396**	**Moenkopi Formation** Reddish-brown, evenly-bedded, ripple-marked, cross-laminated siltstones and fine-grained sandstones. Forms a slope with a few scattered sandstone ledges.
Unconformity		
Permian	**549-670**	**Cutler Group Undivided** Fluvial, red, arkosic sandstones and white marine sandstones, with interbedded red shales. Forms a series of alternating slopes and ledges. Contains the following formations:
	0-76	**White Rim Sandstone** Light gray to yellowish gray, fine-grained, cross-bedded sandstone. Forms overhanging and vertical cliffs.
	76-122	**Organ Rock Shale** Reddish-brown siltstone and shales. Forms a slope.
	61-366	**Cedar Mesa Sandstone** White to pale-reddish-brown, salmon, massive, cross-bedded sandstones interbedded with lenses of red, gray, green, and brown sandstones. Forms a cliff.
	122-457	**Elephant Canyon Formation** Gray, cherty, chalky limestones and dolomites interbedded with pale-red sandstones, blue-gray siltstones, and thin beds of anhydrite. Forms a cliff with some slopes.
Unconformity		
Pennsylvanian	**91-457**	**Honker Trail Formation** Dark-gray, thick-bedded limestones, interbedded with gray cherty limestones, and also blue, red, and gray shales and sandstones. Forms ledges and slopes.
Pennsylvanian	**152-1524**	**Paradox Formation** salt, anhydrite, and gypsum interbedded with euxinic black shales and limestones. Forms a slope.

NW-SE trending synclines, anticlines, and normal faults. The load of overlying sediments and the presence of deep-seated Precambrian faults caused plastic deformation as salt deposits flowed upwards into salt diapirs (Foos, 1999).

Rocks of Arches National Park range in age from Pennsylvanian (Paradox Formation) through Cretaceous (Mancos Shale); however, the Jurassic units, consisting of the Entrada sandstone and Navajo sandstone (Table 2.1), are the most prominent (Foos, 1999). The Entrada sandstone, which forms the majority of natural arches in the park, is divided into three members: the Moab Tongue, Slick Rock, and Dewey Bridge Members. The Moab Tongue is a thin-bedded, reddish-brown, muddy sandstone and siltstone (Foos, 1999). The Slick Rock Member, which makes up most of the arches in the Devils Garden area of Arches, is a massive, reddish-brown sandstone deposited in a coastal environment by wind and streams (Foos, 1999). The Dewey Bridge Member consists of red, interbedded, muddy sandstone and siltstone, making it more susceptible to erosion (Foos, 1999). This member is recognizable by its wavy and distorted bedding, and is found at the base of many overhangs and arches. Below the Dewey Bridge Member is the Navajo sandstone. This tan, cross-bedded sandstone was deposited by wind when the Colorado Plateau was covered by a vast desert (Foos, 1999). Navajo sandstone occurs as both cliffs and bluffs, with arches forming within the layer.

The multitude of natural rock arches within the park boundary is a result of a high concentration of fins and the presence of massive Slick Rock sandstone above the weaker, more friable Dewey Bridge Member. The fins formed as salt layers heaved upward and expanded, creating a systematic series of vertical joints in the massive sandstone, with the development of one joint domain influencing the development of subsequent sets (Cruikshank and Aydin, 1995). Erosion of these fractures enlarged the cracks, leaving behind thin walls of rock. Within these fins, the exposed Dewey Bridge Member was preferentially eroded, undermining the more massive Slick Rock sandstone and creating overhangs. The unsupported roofs of these overhangs enlarged, forming a cove, which continued to erode to form an arch (Foos, 1999). Not all arches, however, begin as fins, and there are several mechanisms of arch formation (see Foos, 1999).

2.2 Canyonlands National Park

The "Island in the Sky" district of Canyonlands National Park is a ~2000 m high mesa with a similar geology to that of Arches National Park. Like Arches, rocks in Canyonlands range in age from Pennsylvanian through Jurassic (Table 2.1). In Canyonlands, the Honaker Trail Formation, which is observable along the Colorado and Green rivers just north of the Confluence, overlies the Paradox Formation, a thick accumulation of salt deposits (Foos, 1999). Above this lie Permian rocks of the Cutler group (Stokes, 1986). The Triassic Moenkopi Formation, which represents a marine transgression across the Colorado Plateau, is separated from the Permian Chinle Formation by an unconformity. Overlying the Chinle Formation is the Wingate sandstone, an orange to brown, cross-bedded, cliff forming sandstone that borders the edges of the mesa and plateaus. The fluvial Kayenta Formation caps the cliffs of Wingate sandstone. In the northern part of Canyonlands, the cross-bedded aeolian Navajo sandstone forms cliffs and rounded domes (Foos, 1999).

2.3 Study Sites

Balanced Rock

Location: Arches National Park

A large block of Slick Rock sandstone balances on top of a layer of the Dewey Bridge Member of the Carmel Formation that rests above Navajo sandstone (Graham, 2004). The total height of Balanced Rock is about 39 m, with the large block that makes up the balancing rock standing 17 m tall.

Corona Arch

Location: Bureau of Land Management

A buttress type arch that eroded through a Navajo sandstone bench and has a span of 43 m, a height of 32 m, a thickness of 4 m, and a width of 3 m (Vreeland, 1976). Erosion has sculpted the arch into a slender, inverted half-catenary shape.

Delicate Arch

Location: Arches National Park

The Slick Rock Member of the Entrada sandstone forms the base and pedestals of this freestanding arch, while the Moab Member of the Curtis Formation forms the bridge (Graham, 2004). The contact between the two is a plane of weakness along an unconformity. The arch has a horizontal span of about 10 m, a vertical opening of 14 m, a thickness of 6 m, and a width of 1.5 m (Vreeland, 1977).

Double Arch

Location: Arches National Park

A pair of thin, shelter type natural arches, weathered in the lower Entrada and upper Carmel (Dewey Bridge Member) formations, which share the same foundation at both of their outer legs. The larger south opening has a span of 50 m, a height of 32 m, a thickness of 8 m, and a width of 9 m (Vreeland, 1977). The smaller north opening has a span of 18 m, a height of 19 m, a thickness of 20 m, and a width of 8.5 m (Vreeland, 1977).

Double O Arch

Location: Arches National Park

A slender, fin type natural arch with two openings stacked on top of one another. Double O Arch formed among a heavy concentration of fins and is made up of the Slick Rock Member of the Entrada sandstone (Vreeland, 1977). The larger (upper) opening has a span of 22 m, a height of 14 m, a thickness of 2 m, and a width of 3 m (Vreeland, 1977). The smaller opening has a span of 6 m and a height of 3 m (Vreeland, 1977).

Gemini Bridges

Location: Bureau of Land Management

A cave type double arch formed in the upper portion of the Windgate Formation (Vreeland, 1976). The outer (eastern) opening has a span of 13 m, a height of 26 m, a thickness of 5.5 m, and a width of 8 m (Vreeland, 1976). The inner opening has a span of 20 m, a height of 18 m, a thickness of 12 m, and a width of 8 m (Vreeland, 1976). The overall height of the arch is 31 m and the maximum distance between the two arcs is 3 m (Vreeland, 1976).

Landscape Arch

Location: Arches National Park

An extremely slender and long arc type natural arch in the Slick Rock Member of the Entrada sandstone. It is the longest arch in North America with a span of 88 m, a height of more than 32 m, and a width of 3 m (Wilbur, n.d.). At its thinnest point, the arch is only 2 m thick (Wilbur, n.d.). On September 1, 1991, a 22 m slab fell from the thinnest section of the span, reducing the thickness of the span from 5 m to 3 m (Graham, 2004). In June of 1995, two more slabs detached, reducing the thickness even further, and the short loop trail that went directly under the arch was closed (Graham, 2004).

Mesa Arch

Location: Canyonlands National Park

An alcove natural arch formed in Navajo Sandstone that spans 27 m across the top of a 150 m vertical cliff (Vreeland, 1987). It has a height of 1.5 m, a thickness of 1.4 m, and a width of 1.8 m. It is one of the most visited sites in Canyonlands National Park.

North Window Arch

Location: Arches National Park

A rock shelter type natural arch cutting a large fin made up of the lower Entrada and upper Carmel (Dewey Bridge Member) formations (Vreeland, 1977). North Window Arch has a span of 28 m, a height of 15.5 m, a thickness of 14 m, and a width of 9 m (Vreeland, 1977). A large vertical crack cuts the fin in half and is exposed along the underside of the arch where it has trapped a few large boulders.

Surprise Arch

Location: Arches National Park

Located within the Fiery Furnace section of the park, this slender and straight alcove type natural arch hangs above an isolated sandstone grotto. The arch formed from an eroded fin of Entrada sandstone and has a span of 19 m, a height of 17 m, a thickness of 1 m, and a width of 1 m (Vreeland, 1977).

CHAPTER 3

METHODS

3.1 Field Methods

Resonant frequencies for the studied arches were anticipated to range between 1 - 10 Hz. This enabled us to use compact 3-component broadband seismometers for ambient vibration measurements. Each 3-component sensor measures the arch's complete motion in three orthogonal directions: up-down (vertical), north-south (horizontal), and east-west (horizontal). We selected Nanometrics Trillium Compact broadband seismometers (flat frequency response between 0.05 and 100 Hz) with 24-bit Centaur digital recorders (Figure 3.1a,b). The loggers are equipped with a GPS clock and powered by 16 A-h rechargeable lithium-ion batteries. Sensors are covered after deployment with insulated plastic coolers to minimize thermal and wind disturbances (Figure 3.2).

Measurements were conducted using multiple configurations. With a limited number of sensors, the majority of our measurements were made using the site-to-reference configuration: one seismometer was placed on or very near the structure being assessed (here termed the active sensor) and the other was placed on stable bedrock at a distance of ~100 m for reference (Figure 3.2). This allowed us to distinguish local versus regional ground motion and target only signals of interest related to arch resonance. Other configurations included placing both sensors on top of the arch, separated by ~5 - 10 m, with no reference sensor. Collecting data simultaneously on top of the arch allowed us to

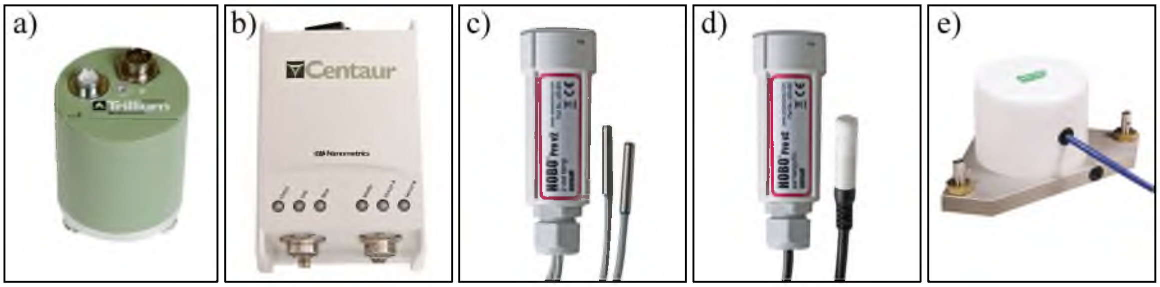

Figure 3.1 Equipment used to conduct field measurements: a) Nanometrics Trillium compact broadband seismometer used for ambient vibration measurements, b) Nanometrics 24-bit Centaur digital recorder, c) Onset HOBO U23 Pro External Temperature Data Logger with two external temperature probes, d) Onset HOBO U23 Pro External Temperature/Relative Humidity Data Logger, e) Jewell Instruments model 701-2(4x) precision biaxial weatherproof tiltmeter.

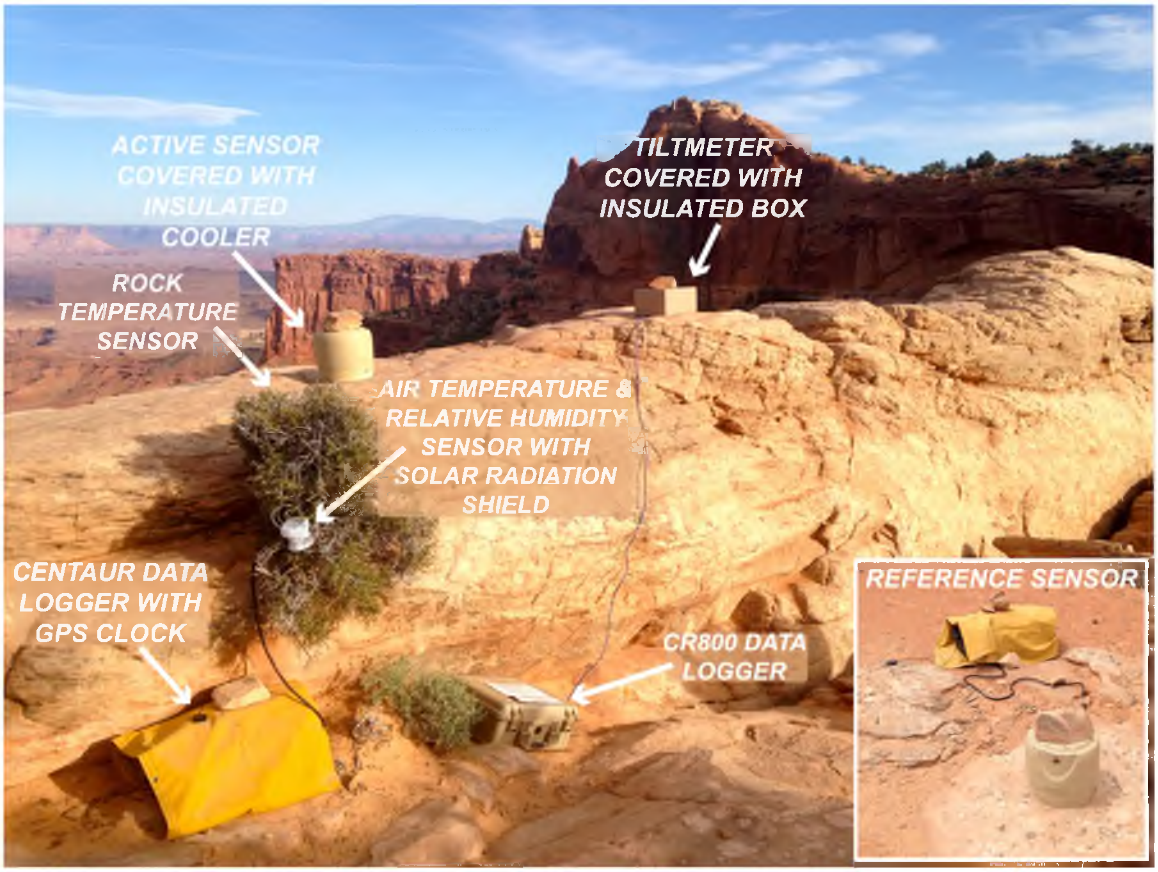

Figure 3.2 A standard deployment at Mesa Arch with the active sensor on top of the arch and the reference sensor at a stable position ~100 m from the arch.

compare the results from each sensor to validate or refute modal and polarization analysis results. We also made measurements with only one active sensor placed on or near the feature with no reference sensor. This was often due to time constraints or the lack of surrounding stable surfaces to place a reference sensor.

Rock and air temperature plus relative humidity sensors were also incorporated with each deployment to identify how the structure reacts to changes in ambient environmental conditions (Figure 3.2). We used an Onset HOBO U23 Pro External Temperature Data Logger with two external temperature probes for rock temperature, and an Onset HOBO U23 Pro Air Temperature/Relative Humidity Data Logger (Figure 3.1c,d). The latter was equipped with a radiation shield to ensure accurate air temperature measurements. The rock temperature sensors were temporarily affixed to the rock, while air temperature and relative humidity sensors were placed above ground, typically hanging from a nearby bush (Figure 3.2). These data helped us identify the environmental sensitivity of resonant frequency for each structure, in order to assist in differentiating reversible from irreversible resonant frequency shifts in repeat measurements.

For arch deformation measurements, we used a Jewell Instruments model 701-2(4x) precision biaxial weatherproof tiltmeter (Figure 3.1e). Sealed lead-acid batteries powered the sensor and a Campbell Scientific CR800 data logger. The sensor was covered with an insulated box to minimize thermal effects and was placed directly on the arch top surface (Figure 3.2). The position was determined using simplified numerical models to ensure we measured maximum tilt. These deformation data are crucial for evaluating the arch's response to thermal and hydrological perturbations, and investigating drivers of observed resonant frequency shifts. In this thesis, we show tilt measurements exclusively from a 3-day test at Mesa Arch.

3.2 Data Processing Methods

The ambient vibration technique involves processing seismic noise to retrieve resonant frequencies of the studied rock arches. Techniques used to process data were developed by Koper and Hawley (2010). The basis of this methodology is to gather fundamental information about the composition of seismic noise, such as polarization attributes, through eigen-decomposition of spectral covariance matrices.

Processing of the ambient vibration data begins by extracting 1 h of data from each sensor component, detrending, and removing the instrument response through spectral division using a trapezoidal frequency-domain taper with frequency limits of 0.001 – 0.002 Hz and 50 – 60 Hz. Each hour-long data block is divided into 10 subwindows that overlap one another by 50%. These subwindows are individually tapered with a Hanning function and processed with a fast Fourier transform (FFT). The diagonal elements of the resulting 3-by-3 spectral matrix are estimates of the power spectral density (PSD) for each component. The PSD is then averaged using a log10 based smoothing scheme explained by Sufri et al. (2013) to produce a clean spectrum from which we measure peak frequencies.

Subsequent eigen-decomposition of each matrix allows for polarization analysis. In this step, polarization information is extracted from the complex dominant eigenvector, as discussed by Park et al. (1987), to yield the horizontal azimuth and dip of particle motion, the degree of polarization, and the phase difference between horizontal-to-horizontal and vertical-to-horizontal components. Phase measurements allow us to determine whether the motions are linear or elliptical. Together these results help determine the modes of vibration at identified frequencies.

3.3 Numerical Modal Analysis

To validate and improve field data interpretations, 3D numerical modeling was performed for the four primary study sites using the finite-element software *COMSOL Multiphysics* (http://www.comsol.com). These models provided an increased understanding of the relevant eigenmodes, and ensured that the locations of the seismometers were optimized to capture these resonant modes.

Field measurements of the basic geometry of Corona Arch and Mesa Arch were collected using tape measurements and a hand-held laser rangefinder to collect the (X,Y,Z) coordinates of roughly 50 points. These were then used to generate a simplified 3D model using *SketchUp* software and imported into *COMSOL Multiphysics*. The 3D geometries for Double O Arch and Landscape Arch, on the other hand, were developed using ground-based, structure-from-motion photogrammetry (http://www.nature.nps.gov/ geology/monitoring/photogrammetry/index.cfm). A nearly complete view of the structure was required to create the 3D model, and photographs from a digital single reflex lens camera (DSLR) paired with GPS locations of camera positions were used to reconstruct each object by moving the camera around the object (Matthews, 2008). The simplified models assume isotropic and homogeneous material properties; required inputs are density, Young's modulus, and Poisson's ratio. These values are determined through trial and error; density and Young's modulus are adjusted in *COMSOL* to match the measured resonant frequencies, while Poisson's ratio remains constant throughout. Boundary conditions are also adjusted to find optimal agreement between the measured and modeled resonant frequencies. The simple geometry of Corona Arch, Double O Arch, and Landscape Arch were easy to match, while Mesa Arch was more difficult and required several trials to achieve good match to field data.

CHAPTER 4

RESULTS

4.1 Corona Arch

4.1.1 Site Description

Corona Arch is located on Bureau of Land Management land near Moab, Utah. It is a northwest trending (~345°) freestanding Navajo sandstone arch that extends perpendicular from a cliff (Figure 4.1a). It appears as a solid structure with little visible wear, i.e., few fresh cracks or newly fallen slabs (Figure 4.1b). Owing to its location on BLM land near Moab, the arch experiences significant recreational activity from climbers and rope swingers (Figure 4.1c). Future research is needed to quantify the influence that human activities have on the speed of damage and erosion, but the permanent bolts that climber's drill into the sandstone create visible damage (Figure 4.1d).

4.1.2 Measurement Overview

Two seismometers were deployed on Corona Arch for a period of ~17 h from August 16 – 17, 2013; the active sensor was located on top of the arch in a relatively flat, accessible position, while the reference sensor was placed ~100 m to the east on flat bedrock (Figure 4.2a). The active sensor was initially placed in a stable position (Position #1) in the center of the arch for ~4 h from 07:40 – 11:50 (all times MDT) (Figure 4.2b). It was deployed again for an overnight test in the same position from 20:40 – 06:00.

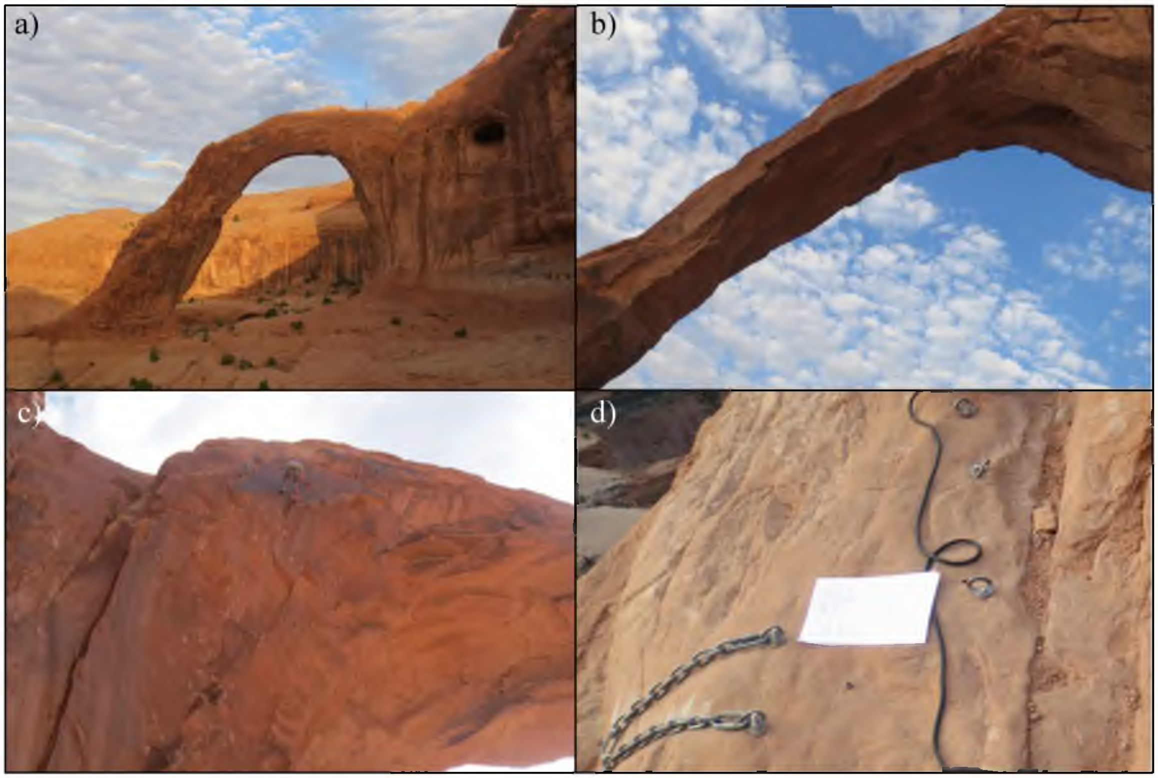

Figure 4.1 Corona Arch near Moab, Utah: a) Side view of Corona Arch showing it branching out from the side of a cliff. b) View from underneath the arch shows a lack of fresh facets. c) A climber descending from the arch. d) Bolts and chains permanently affixed to the top of the arch.

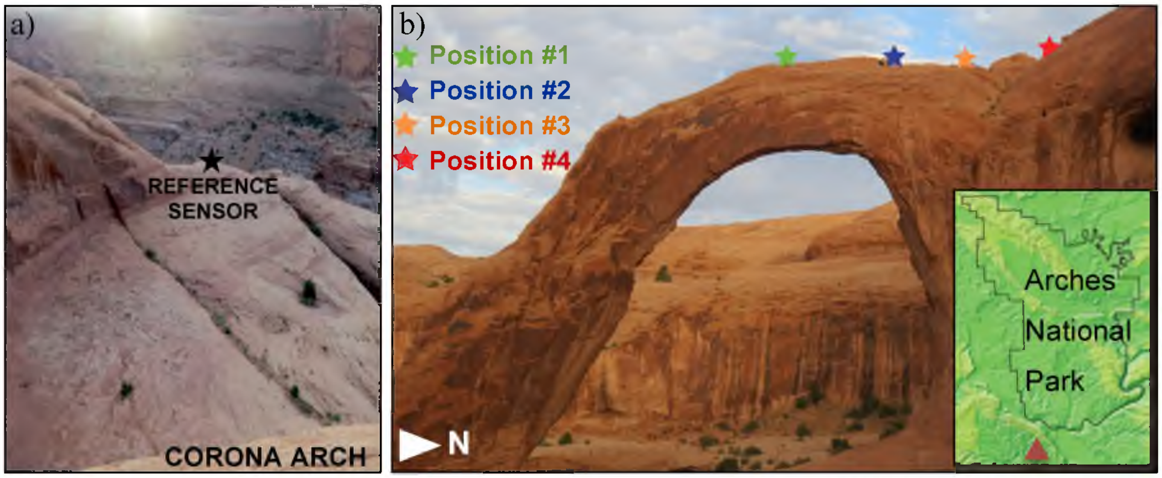

Figure 4.2 Corona Arch near Moab, Utah: a) View from the top of the arch showing the reference sensor located ~100 m to the east. b) Side view of Corona Arch showing the different locations of the active sensor (indicated by stars) as it was moved during the August 16, 2013 deployment. Only one sensor was atop the arch, but was moved during deployment.

To assess if the location of the active sensor affects our results, a moving test was conducted and data were collected for ~1 h at each location. At 06:10, the sensor was moved to Position #2, about 5 m NW from Position #1 (Figure 4.2b). At 07:20, it was moved in a similar fashion to Position #3, then again to Position #4 at 08:33 (Figure 4.2b). The test was completed at 09:34. During this test, we did not have access to the temperature and relative humidity sensors, but local weather stations show that the average temperature for the first morning test was ~27 °C, cooling to ~20 °C, then increasing to ~24 °C by 09:00 (Figure 4.3). The first morning was breezy, but the wind died down by the second deployment.

4.1.3 Ambient Vibration Spectra

Figure 4.4 shows 3-component power spectra from the active sensor, plus one component of reference sensor data for selected time blocks from both deployments. Results reveal several pronounced spectral peaks in ambient vibration data from the arch, which are not present on the reference sensor (other components of the reference are

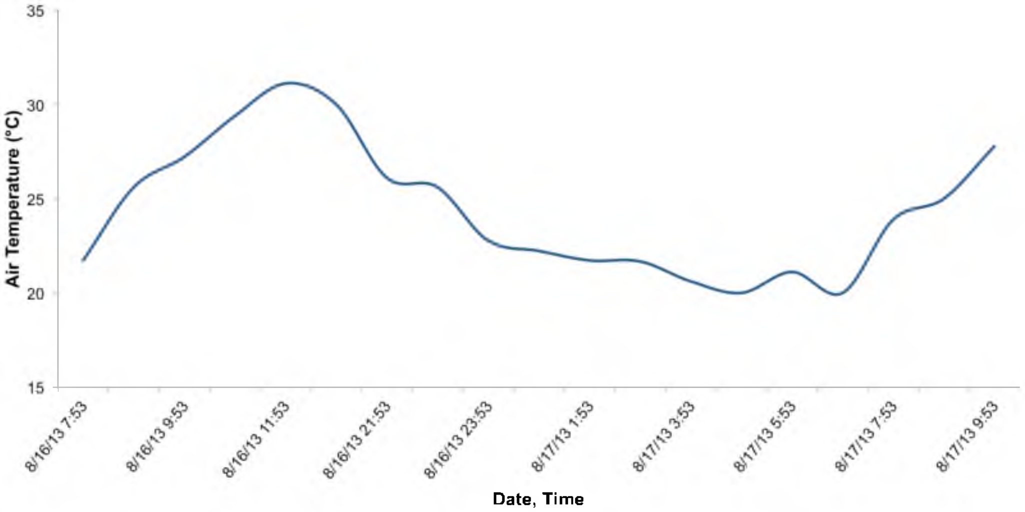

Figure 4.3 Plot of air temperature over the 2-day test. The average air temperature was 27 °C on the 16th and 21 °C on the 17th.

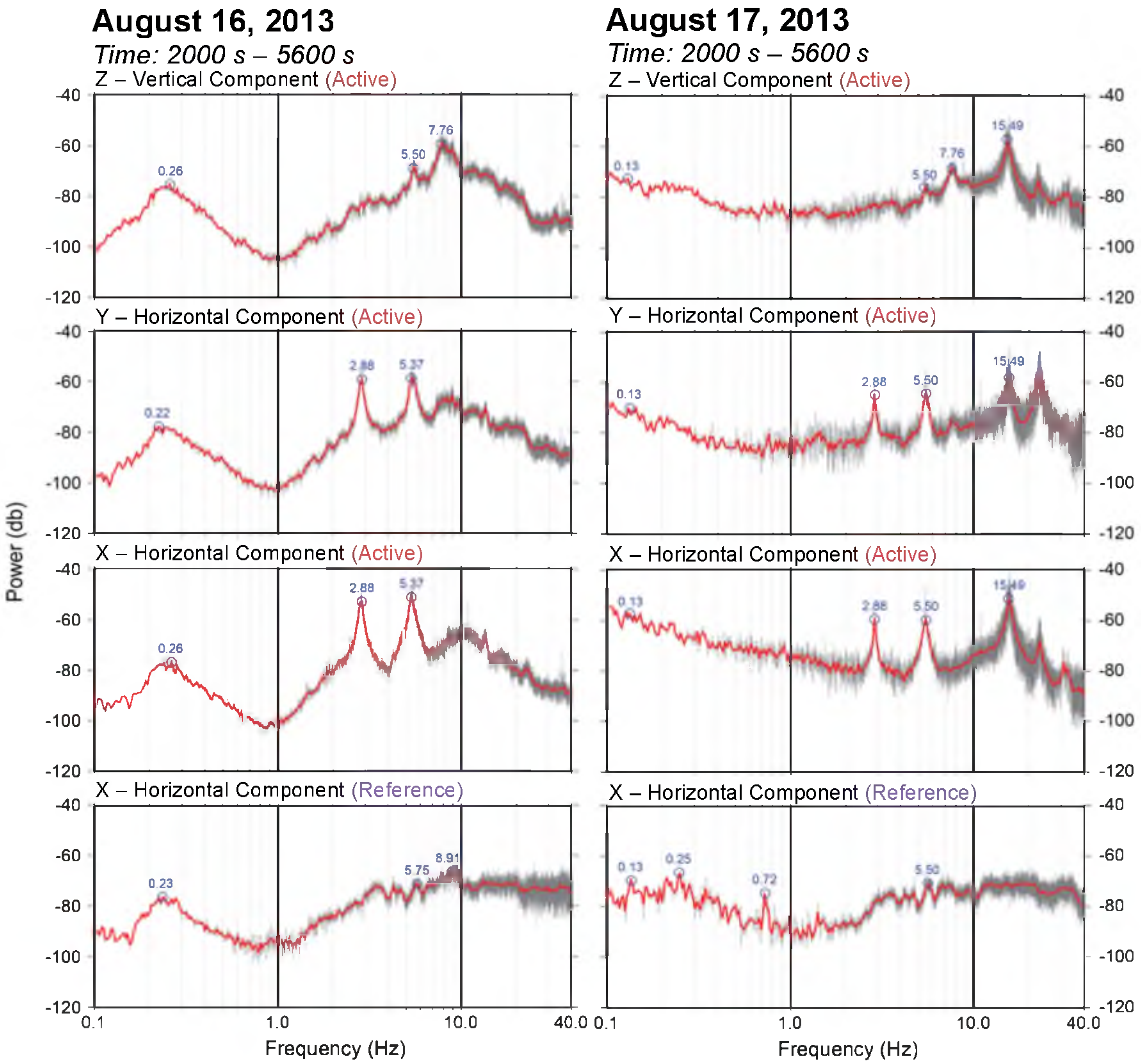

Figure 4.4 Absolute power spectra for 1 h of 3-component ambient vibration data for August 16th and the 17th, 2000 s after start time. Measures of power as a function of frequency are shown in units of $10\log_{10}(m^2s^{-4}Hz^{-1})$ for the vertical component (Z), north-south horizontal component (Y), and east-west horizontal component (X). The bottom plot is the east-west component of data from reference sensor. Gray traces show raw data, red are averaged.

similar to that shown). We measured strong peaks at 2.9 and 5.4 Hz on the horizontal components, and 7.8 Hz in the vertical direction. The lowest frequency peak (2.9 Hz) is the fundamental frequency (*f1*) of vibration for the arch. Both sensors measured a peak in the global 'microseism' at 0.24 Hz, which is earth noise created primarily by distant ocean waves (Zhang et al., 2009).

Rocks were placed on top of the insulated cooler, which we use to protect the active sensor from temperature fluctuations, to prevent the cooler and sensor from being swept off of the arch. We typically place one rock in a sturdy position on the cooler, but multiple rocks were stacked during this deployment. We speculate that the stacked rocks vibrated slightly in the wind, causing a discrepancy in power between the two days (Figure 4.4). This is inferred because we see the appearance of two high-frequency peaks at roughly 15 Hz and 25 Hz, which are not present in the other tests.

Further analysis of the spectra for each sensor location shows that, as long as the sensor is placed on top of the arch, the actual location is not significantly important (Figure 4.5). The center of the arch is ideal, but this test shows that if such a spot is inaccessible, the change in the spectra is not substantial; power simply reduces at more distant positions. The spectrogram for the east-west horizontal component also shows a continuation of each resonant frequency at the different sensor locations (Figure 4.6). The higher resonant frequency (~7.8 Hz), however, does show a slight increase in power at positions #2 and #3, which may be related to the geometry of vibration at this frequency.

4.1.4 Polarization Results

Polarization analysis results are shown in Table 4.1. Corona Arch trends roughly 345°, and our polarization analysis shows that the measured fundamental frequency (*f1*)

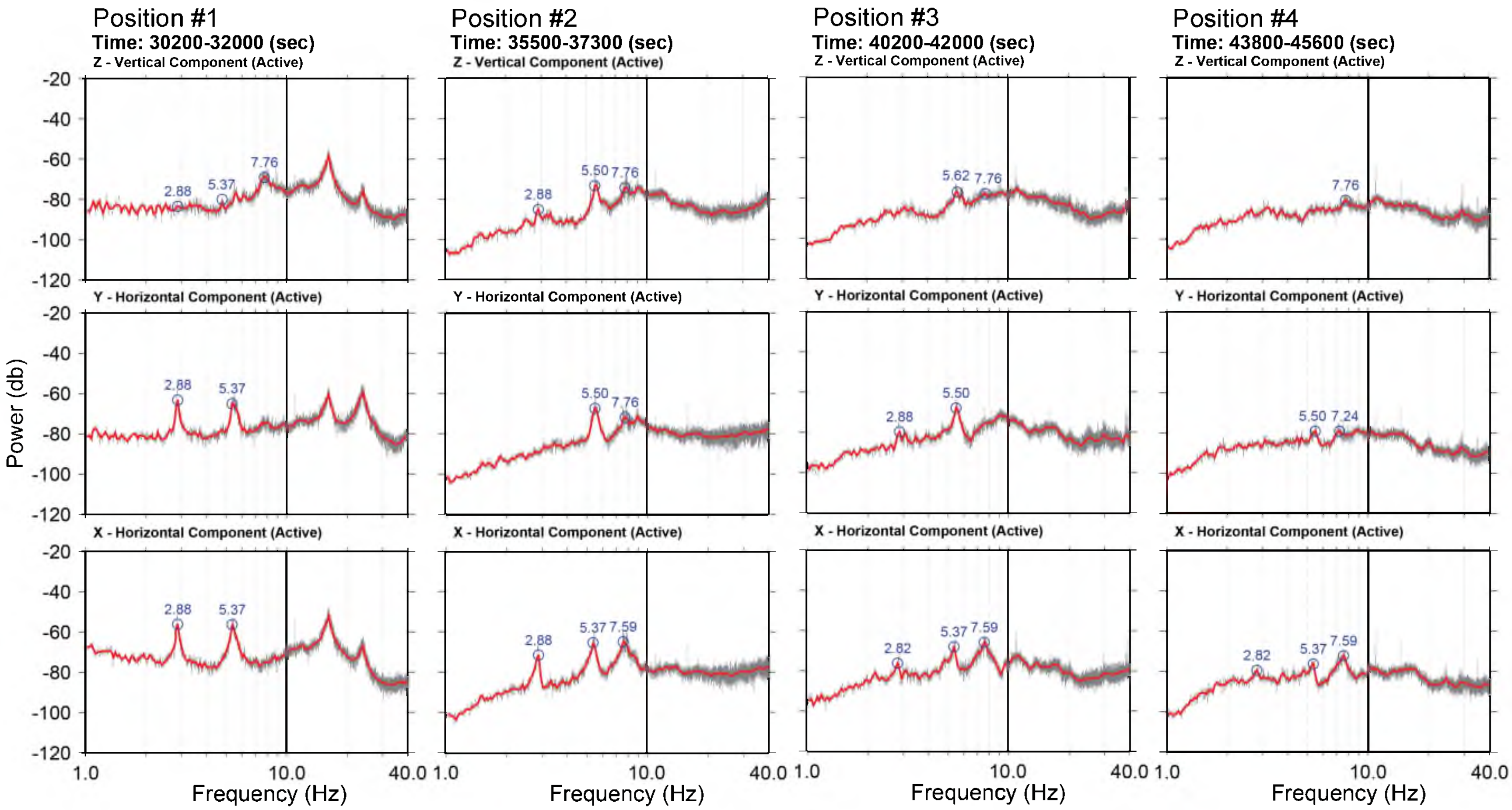

Figure 4.5 Absolute power spectra for 30 min of 3-component ambient vibration data for each sensor location. Measures of power as a function of frequency are shown in units of $10\log_{10}(m^2s^{-4}Hz^{-1})$ for the vertical component (Z), north-south horizontal component (Y), and east-west horizontal component (X). The bottom plot is the east-west component of data from reference sensor.

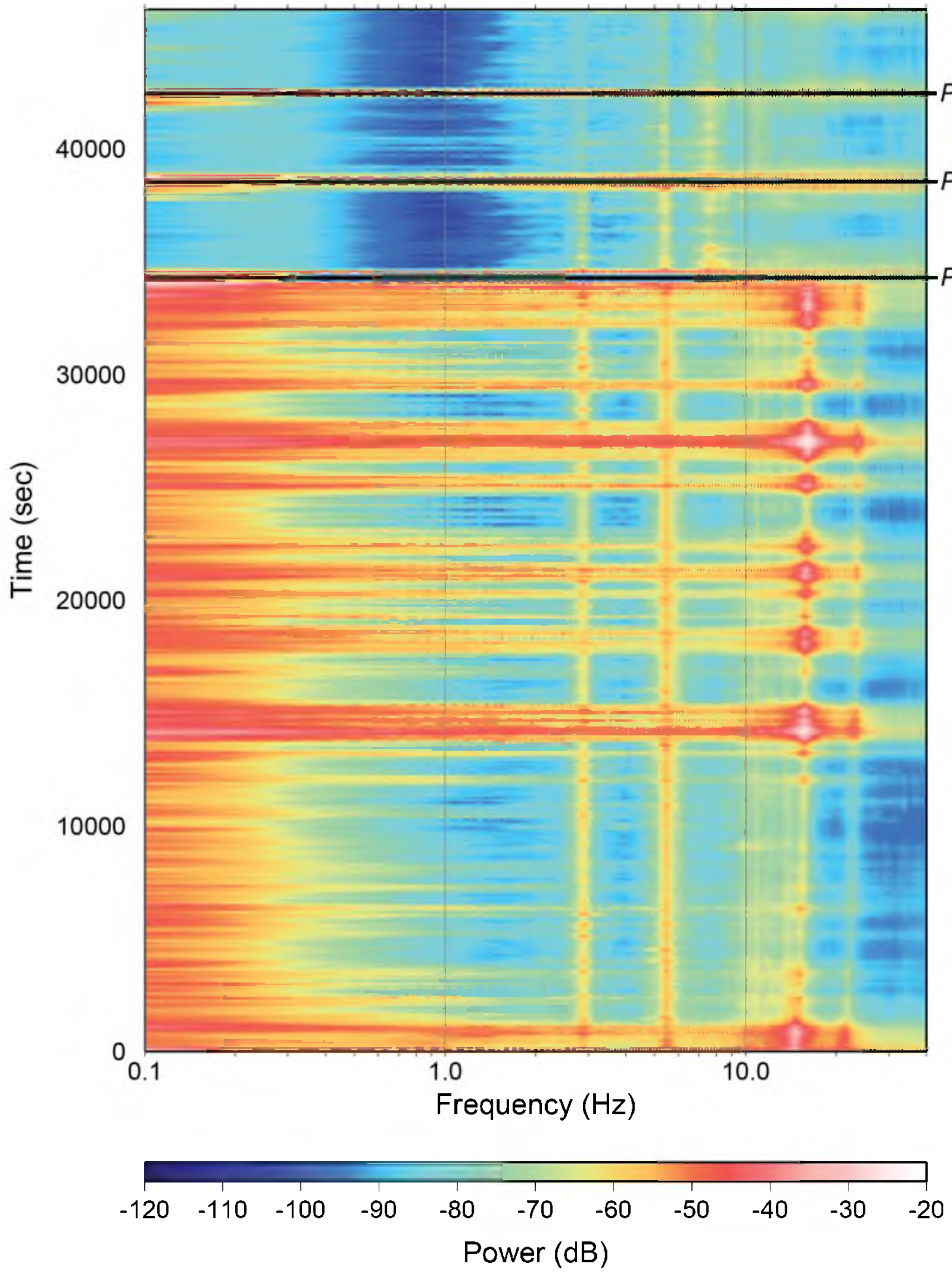

Figure 4.6 Spectrogram for the east-west horizontal component for the overnight and moving tests. Higher powers (indicated by the continuous vertical lines) represent Corona Arch's main resonant modes. Measures of power as a function of frequency are shown in units of $10\log_{10}(m^2s^{-4}Hz^{-1})$.

Table 4.1: Comparison of measured and modeled resonant frequencies and polarization for Corona Arch. DOP: degree of polarization.

Mode	Measured Frequency (Hz)	Modeled Frequency (Hz)	DOP [0-1]	Azimuth / Incidence Measured (°)	Azimuth / Incidence Modeled (°)
1	2.9	2.7	1.0	066 / 89	N/A
2	5.4	5.7	0.9	063 / 85	N/A
3	-	5.7	-	-	-
4	7.8	8.3	0.7	020 / 13	N/A
5	-	8.4	-	-	-

of 2.8 Hz has strongly polarized horizontal motion striking 066° (within ~10° of perpendicular to the arch), with an incidence angle of 89°. Our next measured frequency (*f2*) of 5.4 Hz shows a similar, strong horizontal, orthogonal ground motion, striking 063° with an incidence angle of 85°. The final predominant spectral peak (*f3*) measured at 7.8 Hz shows strong vertical ground motion, striking around 020° with an incidence angle of roughly 13°. See Appendix A for supporting polarization analysis figures.

4.1.5 Numerical Modal Analysis

Figure 4.7 shows the results of preliminary modal analysis. We generated a simplified geometric model of the arch from field measurements, and assumed uniform material composition with density of ρ = 2000 kg/m^3, Young's modulus of E = 3 GPa, and Poisson's ratio of ν = 0.3 determined to best match field data through trial and error.

The first five resonant mode shapes and frequencies are shown in Figure 4.7 and in Table 4.1. We accurately matched the first two predominant spectral peaks measured from field data, and likely the third with less precision, and polarization analysis supports our interpretations. The modeled fundamental mode at 2.7 Hz represents out-of-plane bending in the orthogonal direction, which matches well with our measured fundamental

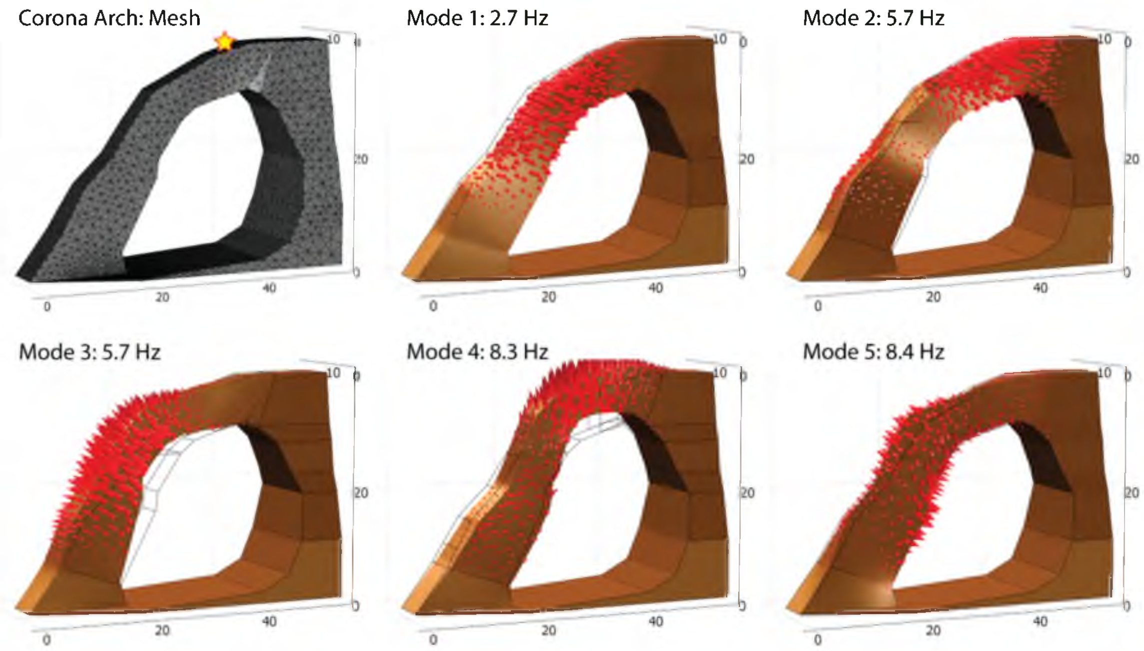

Figure 4.7 Modal analysis for Corona Arch: the first five resonant modes and frequencies are shown along with the model geometry and mesh. Units are meters. The arch is oriented 345°, with north to the right side of the images. Arrows indicate displacement direction and are scaled by magnitude. Deformed body shape shown with original body wireframe. Field data were taken from the position indicated by the star.

frequency of 2.8 Hz with horizontal perpendicular polarization. (Note: we define in- or out-of-plane with respect to the plane of the arch span). Mode 2 is the second out-of-plane bending mode modeled at 5.7 Hz, again with strong horizontal, orthogonal ground motion, and matching well with our measured peak at 5.4 Hz. Mode 3 is the first in-plane bending mode, and being nearly identical in frequency to mode 2, likely does not appear in our measurements (possibly on the vertical component, see Figure 4.4); the predicted amplitude of ground motion for mode 2 is greater at our sensor location than for mode 3 and likely dominates our measurements. Mode 4 as modeled is the second in-plane bending mode, and produces strong vertical ground motion at 8.3 Hz at our sensor location. Our predominant measured vertical spectral peak was at 7.7 Hz, which is close to that predicted. Mode 5 is the first torsion mode, and again appears at a nearly identical frequency as its predecessor with weak motion predicted at our sensor location.

4.1.6 Interpretation and Discussion

Ambient vibration data from Corona Arch show clear and strong spectral peaks. We find good agreement between measured data and model results, and are able to satisfactorily match the first three predominant spectral peaks measured. Analysis of sensor placement via the moving test validated that precise sensor placement is not critical, as long as the instrument is placed on top of the arch. The position in the center of the arch (Position #1) shows the strongest peaks, but the values of measured resonant frequencies remains uniform throughout the tests. Further repeat measurements and analysis are necessary to assess any changes in the structural integrity of Corona Arch. Preliminary results, however, are promising and show that the feature is an ideal candidate for future analysis.

4.2 Double O Arch

4.2.1 Site Description

Double O Arch is located in the Devils Garden section of Arches National Park. It is a northwest trending (~320°) fin type natural arch formed in the Slick Rock Member of the Entrada sandstone, with two openings on top of one another (Figure 4.8a). It appears as a solid structure with few visible cracks or newly fallen slabs. Double O Arch is an ideal feature for performing ambient vibration tests; the top of the arch is relatively easy to access and the long, slender structure produces clear resonant frequencies.

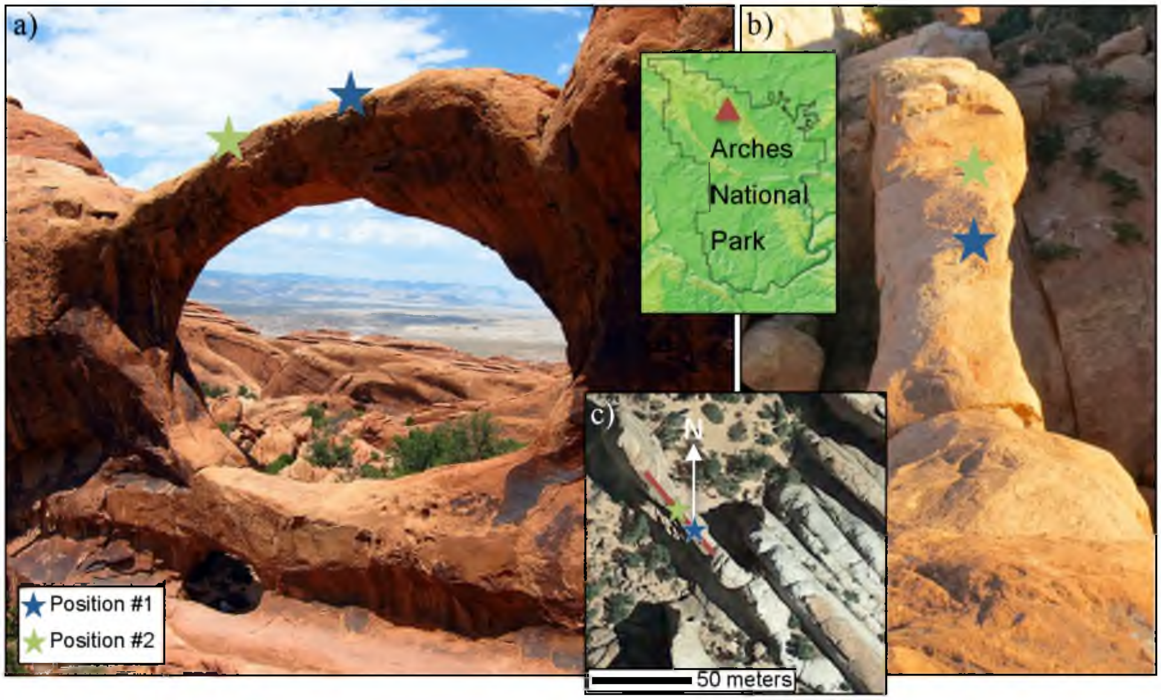

Figure 4.8 Double O Arch in Arches National Park, Utah: a) Two locations of the sensors are indicated by stars. b) View of the top of the arch showing the two sensors. c) Aerial view of Double O Arch with the two sensor locations indicated. The arch is north-west/south-east trending.

4.2.2 Measurement Overview

Two tests were conducted at Double O Arch. The first was performed on October 25, 2013 and the second on May 20, 2014. The area surrounding the arch is filled with a high concentration of fins, leaving no suitable location for a reference sensor. Therefore, both seismometers were placed on top of the arch for a period of ~2 h for the 2013 test, while just one sensor was utilized for the 3 h test in 2014 (Figure 4.8b). For this second test, the sensor was placed in the western position (position #2). Rock and air temperature, plus relative humidity during the two tests are shown in Figure 4.9. The average rock temperature on October 25, 2013 was 20.79 °C and the average air temperature was 17.72 °C, while the average rock temperature on May 20, 2014 was 35.99 °C and the average air temperature was 27.48 °C.

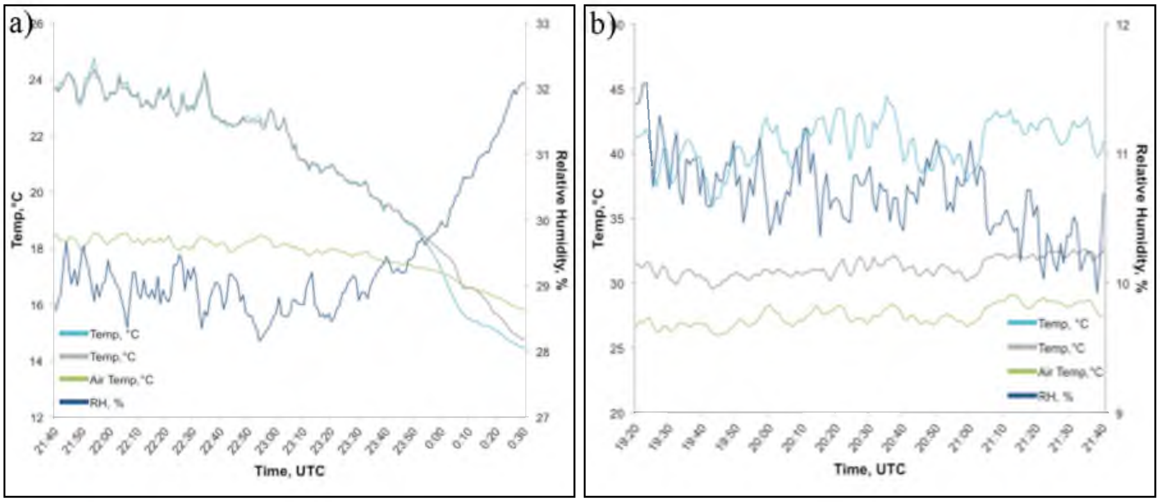

Figure 4.9 Temperature and relative humidity plots for Double O Arch: a) Plot of rock temperature, air temperature, and relative humidity for the test of October 25, 2013. b) Plot of rock temperature, air temperature, and relative humidity for the test of May 20, 2014.

4.2.3 Ambient Vibration Spectra

Figure 4.10 shows 3-component power spectra from all sensors for both deployments. The 2014 data show slightly clearer spectral peaks, so we use these to analyze the spectral characteristics of the arch. We measured strong peaks at frequencies of 2.6 Hz, 5.4 Hz, 6.5 Hz, and 9.8 Hz on all 3 components. Another higher peak at 11.2 Hz is strongest on the vertical component. The lowest spectral peak (2.6 Hz) represents the fundamental frequency of vibration for the arch.

4.2.4 Polarization Results

Tables 4.2 and 4.3 show polarization results for both tests. Double O Arch trends roughly 320°, and polarization analysis from the May test (Table 4.3) shows that the measured fundamental frequency at 2.6 Hz has polarized horizontal motion striking 037°, with an incidence angle of 84°. It is predominant on all components, but strongest on the two horizontal components. The second measured frequency is 5.4 Hz and shows similar,

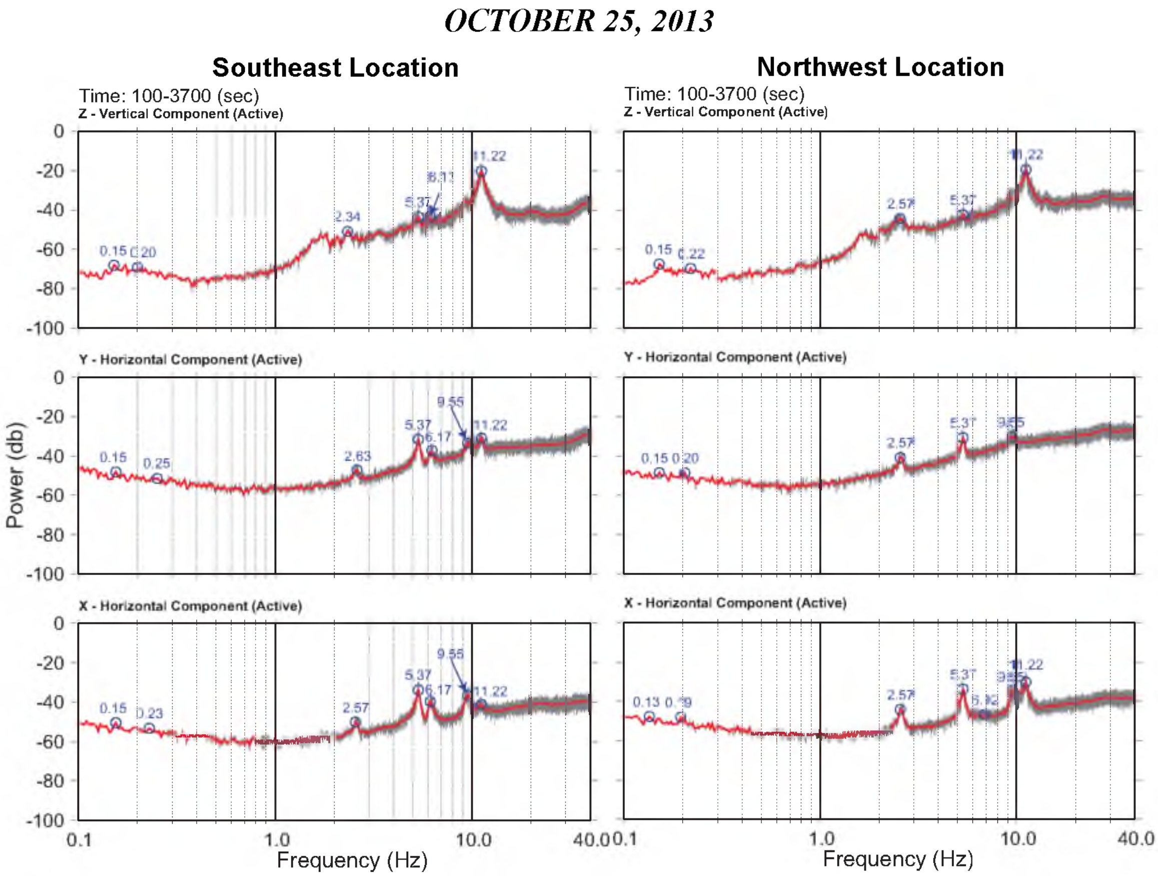

Figure 4.10 Absolute power spectra for 1 h of 3-component ambient vibration data for October 25, 2013 and May 20, 2014. The October spectra begin 100 s after start time and the May spectra begin 3000 s after the start time. Measures of power as a function of frequency are shown in units of $10\log_{10}(m^2s^{-4}Hz^{-1})$ for the vertical component (Z), north-south horizontal component (Y), and east-west horizontal component (X). Gray traces show raw data, red are averaged.

MAY 20, 2014

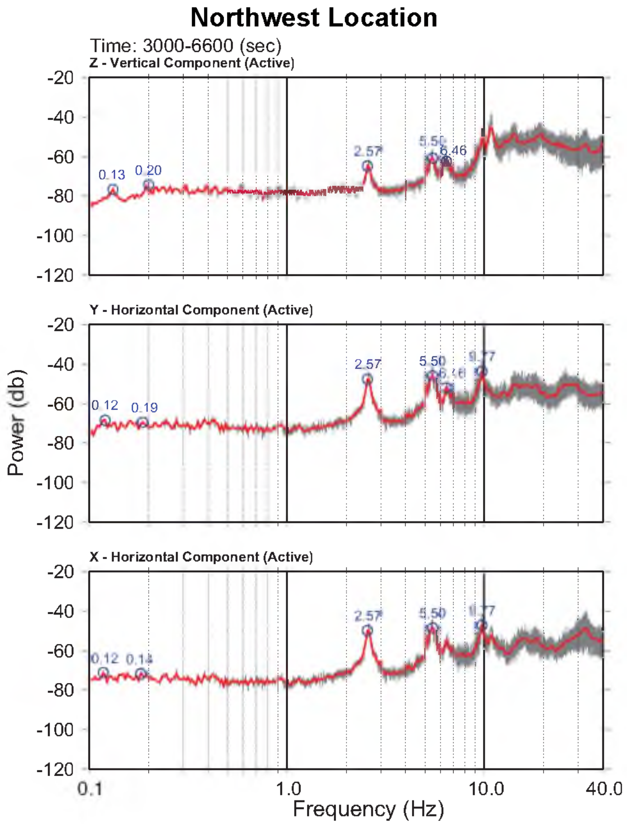

Figure 4.10 (continued)

Table 4.2: Measured spectral peaks for both locations with predominant polarization orientation noted for the ***October 25, 2013*** test.

Southeast Location			
Measured Frequency (Hz)	**DOP [0-1]**	**Azimuth* (°)**	**Incidence** (°)**
2.6	0.7	037	78
5.4	0.9	038	80
6.2	0.7	040	72
9.5	0.6	040	71
Northwest Location			
2.6	0.75	030	73
5.4	0.8	035	70
6.9	0.9	010	66
9.5	0.9	031	66

**Azimuth angle measured in degrees clockwise from magnetic North*

***Incidence angle measured from vertical. 0° = vertical motion, 90° = horizontal motion*

Table 4.3: Measured spectral peaks with predominant polarization orientation noted for the ***May 20, 2014*** test.

Measured Frequency (Hz)	DOP [0-1]	Azimuth* (°)	Incidence** (°)
2.6	1.0	037	84
5.4	1.0	036	82
6.5	0.9	035	77
9.8	1.0	033	68

**Azimuth angle measured in degrees clockwise from magnetic North*
***Incidence angle measured from vertical. 0° = vertical motion, 90° = horizontal motion*

consistent horizontal motion across all data, striking 036° with an incidence angle of 82°. It is also strongest on the two horizontal components. The third measured frequency at 6.5 Hz is the least stable out of all of the modes, shifting slightly for each of the 3 measurements. The peak is relatively uniform in amplitude for all 3 components. It displays motion with an incidence angle of 77° and has a similar azimuth to the preceding peaks of 035°. The fourth measured frequency of 9.8 Hz is present on all 3 components, but is clearest on the two horizontals. The lack of amplitude on the vertical component is likely due to the overpowering 11.2 Hz frequency following this peak. Motion ranges from horizontal to vertical, with an azimuth of 033° and an incidence angle of 68°. See Appendix A for supporting polarization analysis figures.

4.2.5 Numerical Modal Analysis

Figure 4.11 shows the results of modal analysis for Double O Arch. The 3D model was developed using ground-based photogrammetry. We were unable to match the full spectrum of resonant frequencies in the same model, but successfully matched the first three (Table 4.4). Best-fitting material properties in the uniform model were: assumed density of $\rho = 2200$ kg/m^3, Young's modulus of $E = 3$ GPa, and Poisson's ratio of $\nu = 0.3$. The modeled fundamental mode at 2.6 Hz represents the first out-of-plane

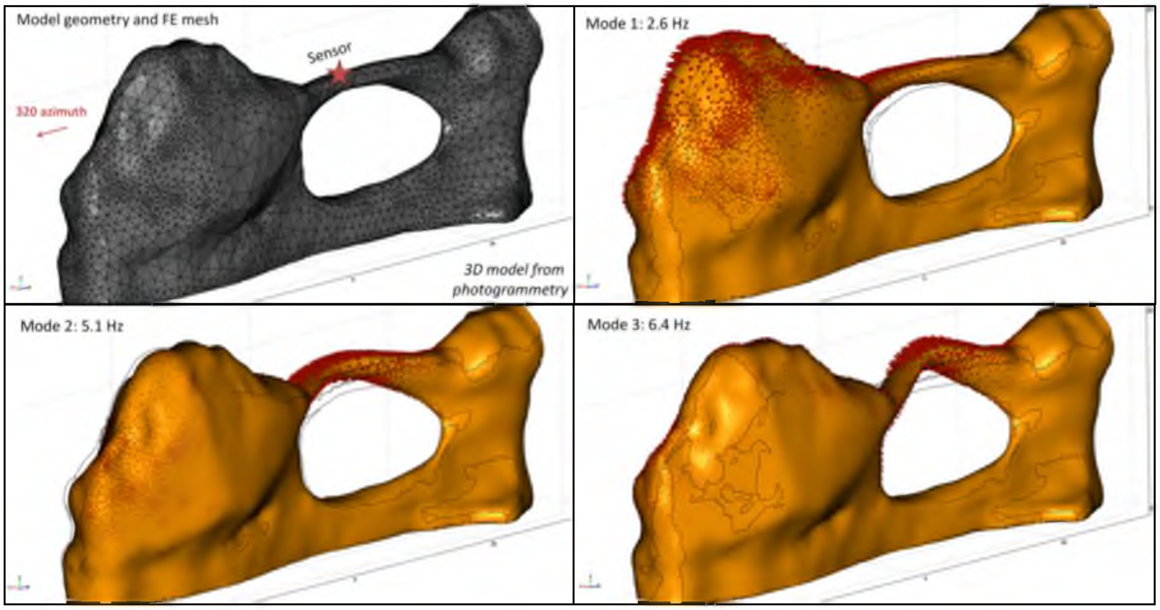

Figure 4.11 Modeled mode shapes and frequencies for the first three resonant modes of Double O Arch from the May 20, 2014 deployment. Arrows indicate displacement direction and are scaled by magnitude. Deformed body shape shown with original body wireframe. Units are meters. The arch is oriented 320°, with north to the left side of the images. Field data were taken from the position indicated by the star.

Table 4.4: Comparison of measured and modeled resonant frequencies and polarization for Double O Arch from the May 20, 2014 deployment. DOP: degree of polarization.

Mode	Measured Frequency (Hz)	Modeled Frequency (Hz)	DOP [0-1]	Azimuth / Incidence Measured (°)	Azimuth / Incidence Modeled (°)
1	2.6	2.6	1.0	037 / 84	040 / 85
2	5.4	5.1	1.0	036 / 82	040 / 82
3	6.2	6.4	0.9	035 / 77	044 / 66
?	9.8	-	1.0	033 / 68	-

bending in the orthogonal direction and includes the large adjoining rock tower, which supports our measured frequency showing horizontal polarization. (Note: we define in- or out-of-plane with respect to the plane of the arch span.) Mode 2 represents the second out-of-plane bending mode modeled at 5.1 Hz, again with strong horizontal, orthogonal ground motion, and matching well with our measured peak of 5.4 Hz. Mode 3 shows slightly in-plane bending with a greater vertical component of motion modeled at 6.4 Hz, matching well with our measured peak of 6.5 Hz.

4.2.6 Interpretation and Discussion

Data from Double O Arch show clear and strong spectral peaks. We find good agreement between measured data and model results, and are able to satisfactorily match the first three predominant spectral peaks measured. The inability to match the higher order frequencies may be a deficiency of the assumed uniform model composition. Further analysis and repeat measurements are necessary to quantifiably assess any changes in the structural integrity of Double O Arch. Preliminary results, however, show promise and make this site an ideal candidate for future analysis.

4.3 Landscape Arch

4.3.1 Site Description

Landscape Arch is located in the Devils Garden section of Arches National Park. It is a northwest trending (~325°) arc type natural arch formed in the Slick Rock Member of the Entrada sandstone (Figure 4.12a,b). It is the longest arch in North America with a span of 88 m. In September 1991, a 22 m slab fell from the thinnest section of the span.

Figure 4.12 Landscape Arch in Arches National Park, Utah: a) Our sensor was located at the base of the arch (indicated by the white arrow). b) View from underneath the arch.

4.3.2 Measurement Overview

A single test was conducted at Landscape Arch on May 21, 2014. The area surrounding the arch is filled with a high concentration of fins, leaving no suitable location for a reference sensor, and the top of the arch is currently inaccessible. Therefore, one seismometer was placed at the base of the arch for a period of ~3.5 h (Figure 4.13a). Rock and air temperature, plus relative humidity during the test are shown in Figure 4.13b.

4.3.3 Ambient Vibration Spectra

Figure 4.14 shows 3-component power spectra indicating multiple pronounced spectral peaks in ambient vibration data from the arch. We measured strong peaks at 1.9 Hz, 2.5 Hz, 3.3 Hz, 4.6 Hz, and 5.6 Hz on the horizontal components and 1.8 Hz, 2.5 Hz, 3.0 Hz, 4.2 Hz, and 5.6 Hz on the vertical component. The lowest peak (1.8 – 1.9 Hz) is

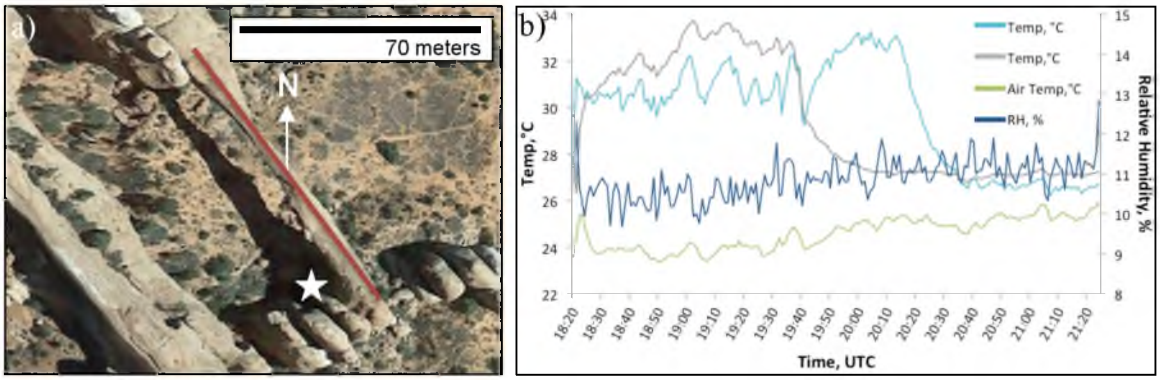

Figure 4.13 Further analysis of Landscape Arch: a) Aerial view of Landscape Arch with sensor location indicated by the white star. The arch is north-west/south-east trending. b) Temperature, air temperature, and relative humidity (RH) for the test. The average rock temperature was 29.59 °C and the average air temperature was 24.59 °C.

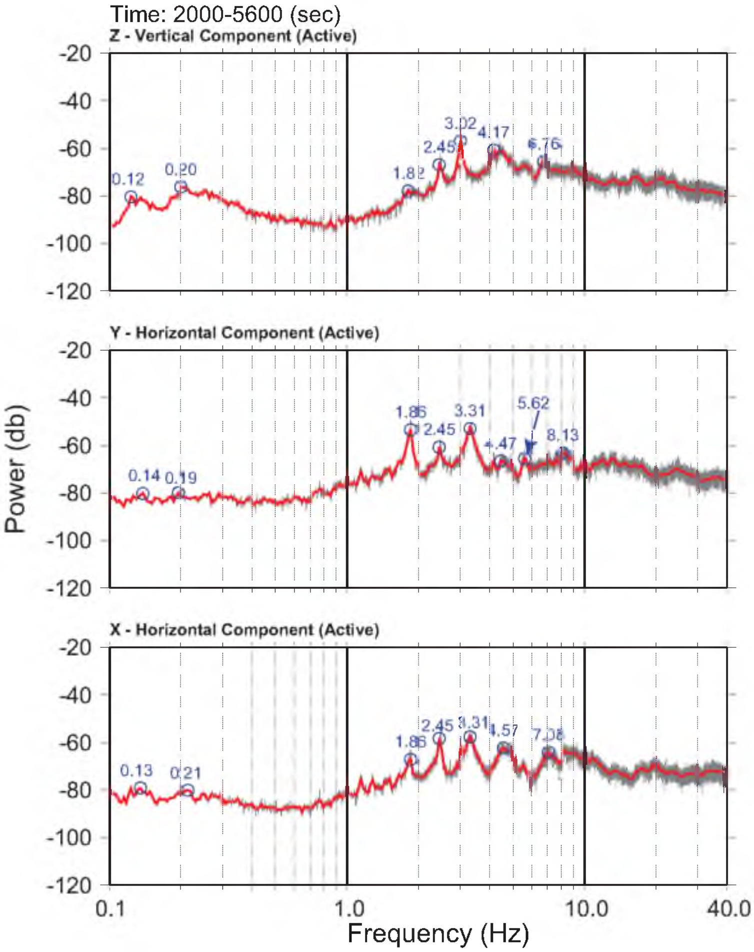

Figure 4.14 Absolute power spectra for 1 h of 3-component ambient vibration data (18:53 – 19:53). Z is vertical vibration, Y is north-south horizontal, X is east-west horizontal. Gray traces show raw data, red are averaged.

interpreted as the fundamental frequency of vibration for the arch. The sensor was placed at the base of the structure, making it likely that some of the peaks measured may be attributed to surrounding features, in addition to the arch itself.

4.3.4 Polarization Results

Polarization analysis is shown in Table 4.5. Landscape Arch trends roughly 325°, and our analysis shows that the measured fundamental frequency at 1.9 Hz has strongly polarized horizontal motion striking 013° with an incidence angle of 90°. The second measured frequency of 2.5 Hz has more inclined motion, striking 053° with an incidence angle of 73°. The third measured frequency at 3.0 Hz only appears on the vertical component and shows weakly polarized vertical motion striking 034° with an incidence angle of 22°. The fourth measured frequency of 3.3 Hz is present only on the two horizontal components, with an azimuth of 030° and an incidence angle of 89°. The fifth measured frequency of 4.2 Hz is present mainly on the vertical component; motion has an azimuth of 150° and an incidence angle of 30°. The sixth measured frequency of 4.6 Hz is present on all 3 components, but is strongest on the east-west horizontal component. It has an azimuth of 121° and a more inclined incidence angle of 46°. The seventh and final measured frequency of 5.6 Hz appears strongest on the north-south horizontal and vertical components, with motion striking 030° and an incidence angle of 49°.

4.3.5 Numerical Modal Analysis

The 3D models for modal analysis were developed using ground-based photogrammetry. Material properties were selected to best match field data through trial and error. We used uniform values of: ρ = 2200 kg/m^3 for density, E = 8 GPa for

Table 4.5: Comparison of measured and modeled resonant frequencies and polarization for Landscape Arch. DOP: degree of polarization.

Mode	Measured Frequency (Hz)	Modeled Frequency (Hz)	DOP [0-1]	Azimuth Measured (°)	Incidence Measured (°)	Azimuth / Incidence Modeled (°)
1	1.9	1.7	1.0	013	90	026 / 82
2	2.5	2.5	0.9	053	73	045 / 81
?	3.0	-	0.4	?	88	-
3	3.3	3.4	0.9	030	89	036 / 79
4	4.2	4.1	0.7	150	30	023 / 70
?	4.6	-	0.8	121	46	-
5	5.6	5.6	0.7	030	49	307 / 54

**Azimuth angle measured in degrees clockwise from magnetic North*
***Incidence angle measured from vertical. 0° = vertical motion, 90° = horizontal motion*

Young's modulus, and $v = 0.3$ for Poisson's ratio. The first five resonant mode shapes and frequencies are shown in Figure 4.15 and in Table 4.5. Two frequencies that we were unable to match showed poor polarization results, making it less likely that those frequencies are attributed to the arch. The modeled fundamental mode at 1.9 Hz represents the first out-of-plane bending mode in the orthogonal direction, which supports our measured frequency showing vertical polarization and horizontal motion. (Note: we define in- or out-of-plane with respect to the plane of the arch span.) Mode 2 represents the first in-plane bending mode modeled at 2.5 Hz, with predominately vertical vibration, and matching well with our measured peak of 2.5 Hz. Mode 3 is second out-of-plane bending modeled at 3.4 Hz, matching well with our measured peak of 3.3 Hz. Mode 4 is akin to second in-plane bending mode modeled at 4.1 Hz with predominately vertical motion, matching well with our measured peak of 4.2 Hz. The final mode, mode 5, modeled at 5.6 Hz shows horizontal motion that may be described as inclined out-of-plane bending. This frequency matches well with our measured peak of 5.6 Hz. Overall, polarization measurements match well with model predictions for the first three modes,

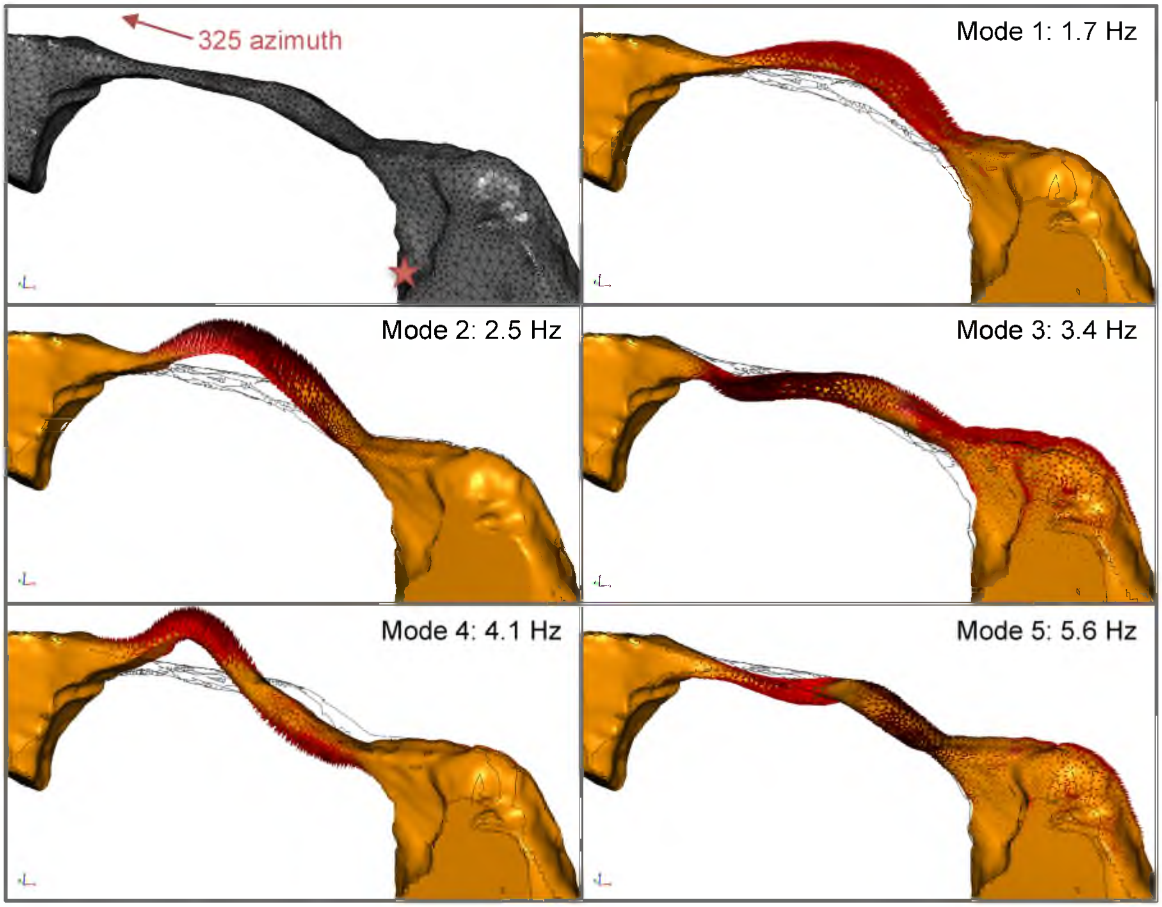

Figure 4.15 Modeled mode shapes and frequencies for the first five predicted resonant modes of Landscape Arch. Arrows indicate displacement direction and are scaled by magnitude. Deformed body shape shown with original body wireframe. Units are meters. The arch is oriented 325°, with north to the left side of the images. Field data were taken from the position indicated by the star.

while discrepancies appear more pronounced at modeled modes 4 and 5 (Table 4.5).

4.3.6 Interpretation and Discussion

Data from Landscape Arch show clear, strong spectral peaks. We find good agreement between measured data and model results, and are able to satisfactorily match five out of the seven predominant spectral peaks measured. Without placing a sensor directly on top of the arch, however, we are unable to conclusively state that the measured spectral peaks are representative entirely of Landscape Arch. This is the only arch where we measured clear spectral peaks when placing the sensor at the base of the structure, which is likely a result of the geometry and size of the long, slender arch producing strong vibration amplitudes. The substantially lower *f1* measured at Landscape Arch compared to other arches studied is similarly related to the great size of the structure; material properties assumed in our model are similar to other arches. Further analysis and repeat measurements are necessary to assess any changes to the structural integrity of Landscape Arch, but our preliminary results suggest that the site is an ideal candidate for future analysis.

4.4 Mesa Arch

4.4.1 Site Description

Mesa Arch is located in the Island in the Sky district of Canyonlands National Park, and is among one of the primary tourist attractions in the park. The geometry of the arch is unique in the sense that it is a pothole arch, perched along the side of a cliff and connected to a slab that is separating from the cliff face. The arch trends roughly north (0° in the center and bending to ~10° where it is attaches to the cliff) and is composed of

Navajo sandstone (Figure 4.16a-d). Incremental failure is predicted to occur as slabs detach from the underside of the cracked and partly undermined northern abutment. Outward deflection and crack opening are also likely, resulting in possible toppling. The top of the arch is easy to access, making it attractive for visitors to climb (Figure 4.16b). Park regulations, however, no longer permit visitor access to the top of the arch.

4.4.2 Measurement Overview

A series of 10 tests were conducted at Mesa Arch between September 2013 and October 2014, ranging in duration from 1 h to 3 d. Data were collected using multiple sensor configurations. The majority of the measurements were made using the site-to-reference configuration: one active sensor and one reference sensor, with the active sensor placed in a position that is safe to access throughout the year (Figure 4.16a). Other measurements were made with both sensors placed atop the arch simultaneously, or just one sensor placed on the arch with no reference. Temperature and relative humidity data were collected during every test, and relative rock surface tilt was measured during the May 5 - 8, 2013 test.

4.4.3 Ambient Vibration Spectra

Figure 4.17 shows 3-component power spectra from the active sensor for all 10 deployments. The active sensor was placed in the same position on the arch for most tests, with the exception of October 28, 2014, when the sensor was placed in the center of the arch. Figure 4.17 shows spectra from the E-W horizontal component of motion, which best displays the pertinent resonant frequencies.

Results reveal several pronounced spectral peaks in ambient vibration data from

Figure 4.16 Mesa Arch in Canyonlands National Park, Utah: a) Deployment showing the active sensor and tiltmeter. b) Visitors on top of the arch. c) View of the arch from the southeast. d) Side view of the arch showing it peeling from the cliff. e) Aerial view of Mesa Arch with active sensor location indicated by the blue star. f) Deployed reference sensor.

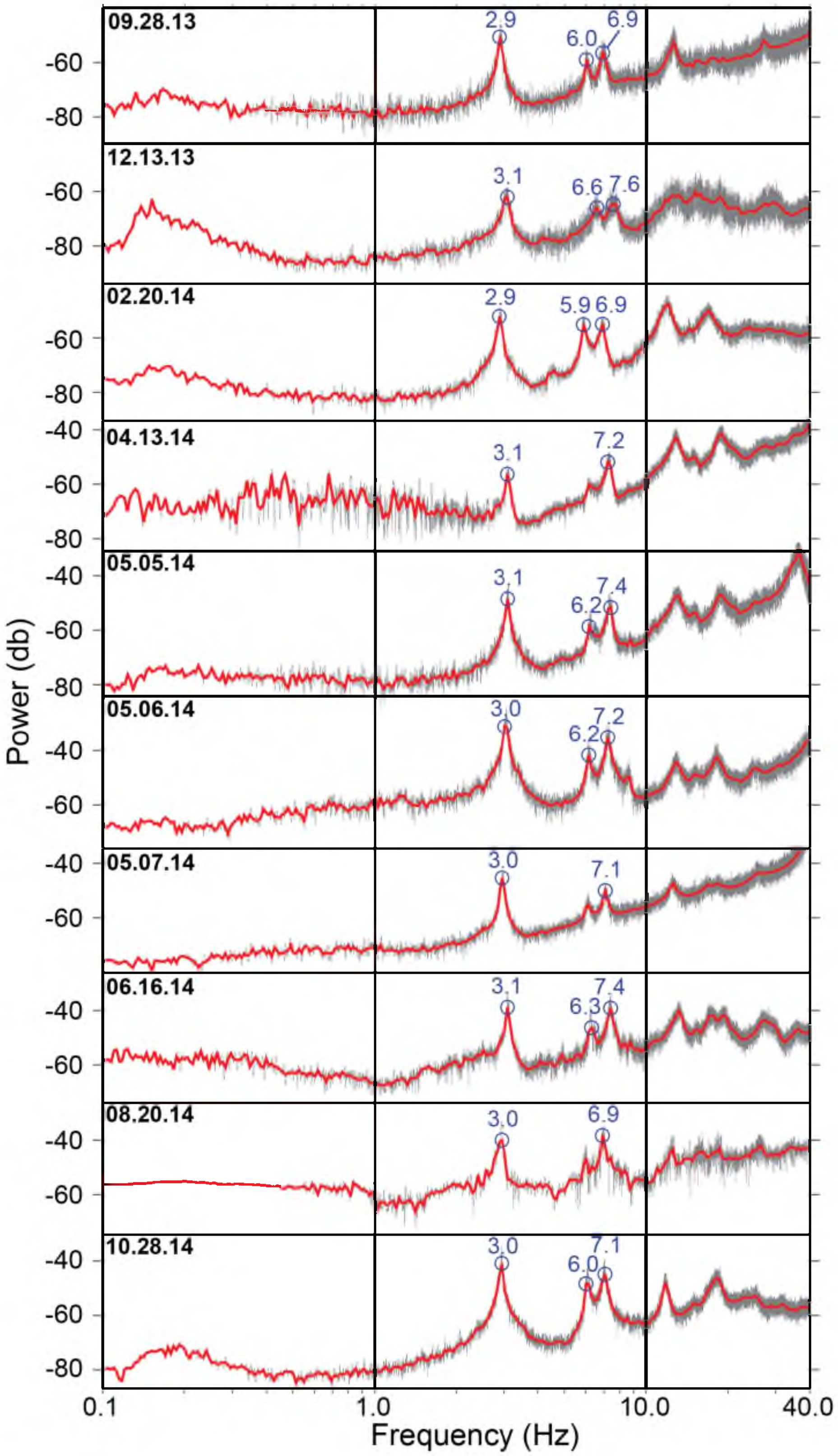

Figure 4.17 Hour-long power spectral density (PSD) plots for the horizontal (east-west) component from each test at Mesa Arch. Gray traces show raw data, red are averaged.

the arch. We measured strong peaks ranging from 2.9 – 3.1 Hz, 5.9 – 6.6 Hz, and 6.9 – 7.6 Hz on the horizontal components, and between 8.3 – 8.7 Hz in the vertical direction. The lowest peak (~3 Hz) is the fundamental frequency of vibration for the arch. Both the active and reference sensors measured a peak in the global 'microseism' at 0.24 Hz, which is earth noise created primarily by distant ocean waves (Zhang et al., 2009).

Further analysis was conducted to determine if the location of the sensor affects the model frequencies (see October 28, 2014 in Figure 4.17). Moving the sensor to the center of the arch showed more pronounced frequency peaks, and better-defined peaks on the vertical component, but the measured frequencies remained the same. In addition, this test allowed for a more complete polarization analysis to validate our modeled results.

Figure 4.18 shows temperature data plotted versus time, along with the four resonant frequencies, to analyze the relationship between resonant frequency shifts and rock temperature fluctuations. Temperature data are averaged and frequencies are normalized to display the percent deviation from the mean. Resonant frequencies correlate directly with temperature (i.e., as temperature increases, frequency increases), with the exception of December 13, 2013 when data were collected during below freezing temperatures. This relationship was further analyzed during the 3-day continuous monitoring test (Figure 4.19). Figure 4.20a shows variation in the first four resonant frequencies, indicating diurnal as well as multiday trends, while Figure 4.20b shows the relationship between the rock surface temperature, *f1* on the east-west horizontal component, and northward relative tilt. Results validate observations from the repeat tests, showing a direct correlation between resonant frequencies, temperature, and tilt.

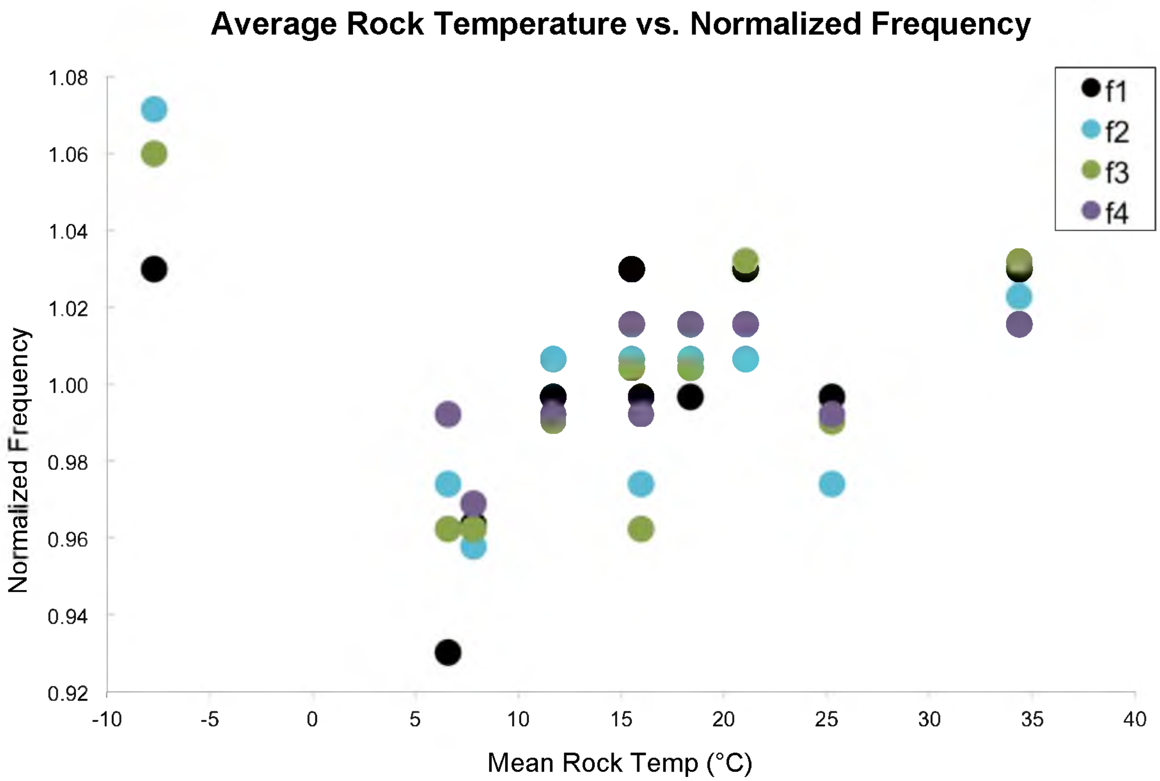

Figure 4.18 Data from September 2013 to October 2014. Plot showing changes in resonant frequencies correlating with changes in rock temperature. Frequencies are normalized to display the percent deviation from the mean.

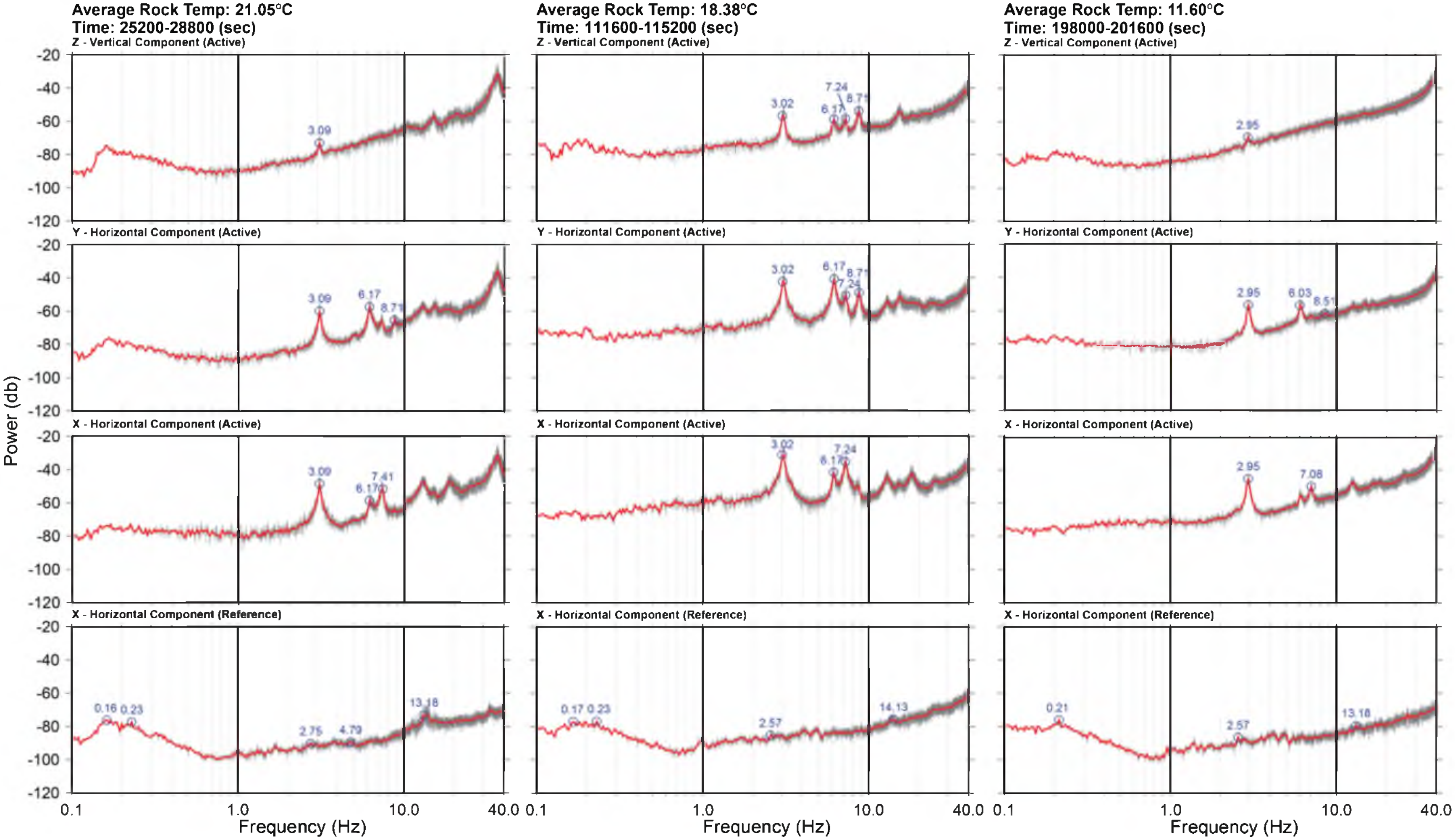

Figure 4.19 Hour-long PSD plots from varying times during the 3-day test at Mesa Arch. The top three plots show the 3 components from the active sensor, while the bottom plot shows the east-west horizontal component from the reference sensor.

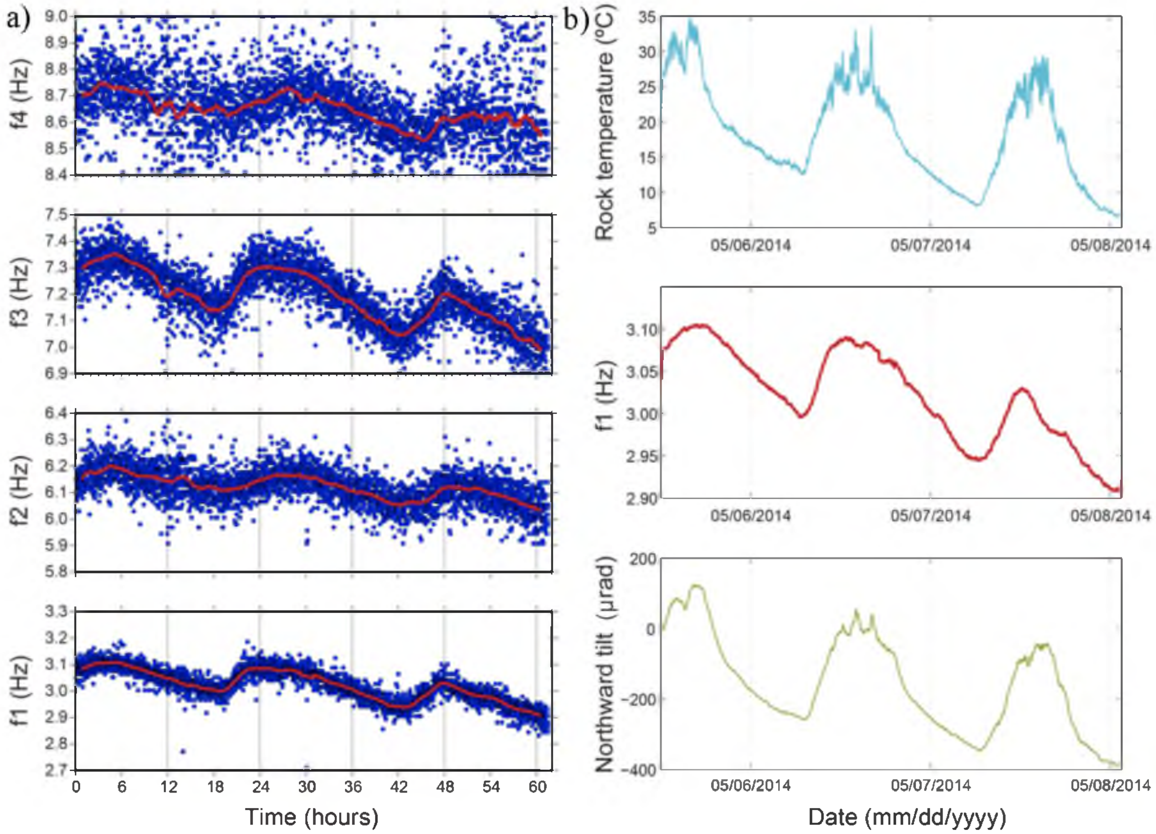

Figure 4.20 Data from the 3-day test at Mesa Arch: a) Plot showing daily and multiday trends in the four predominant resonant frequencies of Mesa Arch. b) Trend between rock surface temperature (top), *f1* on the east-west horizontal component (middle), and northward relative tilt (bottom).

4.4.4 Polarization Results

Mesa Arch trends roughly 0° in the center of the arch but bends to approximately 10° at the accessible sensor position. Polarization analysis (Table 4.6) revealed that the measured fundamental frequency ranging from 2.9 – 3.1 Hz has strongly polarized horizontal motion striking 090° – 108°, which is perpendicular to the trend of the arch, with incidence angles from 85° – 88°. The second measured frequency varies between 5.9 – 6.6 Hz and shows consistent horizontal motion across all data, typically in the range of 15° to 30° greater in azimuth than the first frequency. It is prominent on the north-south component. The third measured frequency ranges from 6.9 – 7.6 Hz. It is typically greatest on the east-west component and sometimes visible on the vertical component. This frequency shows strong horizontal motion (incidence angles from 80° – 89°) and is polarized nearly perpendicular to strike of the arch with azimuth ranging from 93° – 102°). The fourth measured frequency ranges from 8.3 – 9.1 Hz and is dominant on the north-south and vertical components; hence, it is rarely visible in Figure 4.17. This peak has lower amplitude than the previous three, potentially causing error in its measurement. The motion has azimuth ranging from 220° – 278° with incidence angles from 55° – 83° at the normal sensor position. See Appendix A for supporting polarization analysis figures.

4.4.5 Numerical Modal Analysis

Figure 4.21 shows the results of the modal analysis. The simplified geometric model of the arch was generated from field measurements, and we applied uniform material properties with density of $\rho = 2000$ kg/m^3, Young's modulus of $E = 5.5$ GPa, and Poisson's ratio of $\nu = 0.3$.

Table 4.6: First four resonant frequencies of Mesa Arch measured during each test with key polarization data, rock and air temperature noted. DOP: degree of polarization.

Date	Frequency (Hz)	DOP	Dominant Azimuth* (°)	Incidence Angle** (°)	Avg. Rock Temp (°C)	Avg. Air Temp (°C)
First Peak (f1)						
9/28/13	2.8	1.0	106	87	6.59	6.37
12/13/13	3.1	0.9	104	89	-7.72	-6.06
2/20/14	2.9	1.0	089	88	7.83	3.68
4/13/14	3.1	0.9	110	89	15.51	14.20
5/6/14	3.1	1.0	105	87	21.05	20.86
5/7/14	3.0	1.0	106	87	18.38	18.13
5/8/14	3.0	1.0	106	87	11.69	11.60
6/16/14	3.1	1.0	108	86	34.35	---
8/20/14	3.0	1.0	099	86	15.97	14.90
10/28/14	3.0	1.0	102	83	25.24	14.96
Second Peak (f2)						
9/28/13	6.0	0.8	126	85	6.59	6.37
12/13/13	6.6	0.9	118	84	-7.72	-6.06
2/20/14	5.9	0.9	111	86	7.83	3.68
4/13/14	6.2	0.7	135	80	15.51	14.20
5/6/14	6.2	1.0	139	85	21.05	20.86
5/7/14	6.2	1.0	136	85	18.38	18.13
5/8/14	6.2	0.7	146	83	11.69	11.60
6/16/14	6.3	0.7	142	83	34.35	---
8/20/14	6.0	0.8	128	82	15.97	14.90
10/28/14	6.0	1.0	049	31	25.24	14.96
Third Peak (f3)						
9/28/13	6.9	0.9	096	86	6.59	6.37
12/13/13	7.6	0.9	086	89	-7.72	-6.06
2/20/14	6.9	1.0	083	88	7.83	3.68
4/13/14	7.2	0.9	102	80	15.51	14.20
5/6/14	7.4	1.0	099	89	21.05	20.86
5/7/14	7.2	1.0	099	86	18.38	18.13
5/8/14	7.1	0.8	100	89	11.69	11.60
6/16/14	7.4	1.0	101	85	34.35	---
8/20/14	6.9	1.0	093	52	15.97	14.90
10/28/14	7.1	0.9	115	61	25.24	14.96
Fourth Peak (f4)						
9/28/13	8.5	0.7	247	83	6.59	6.37
12/13/13	---	---	---	---	-7.72	-6.06
2/20/14	8.3	0.4	242	68	7.83	3.68
4/13/14	8.7	0.4	227	68	15.51	14.20
5/6/14	8.7	0.3	240	55	21.05	20.86
5/7/14	8.7	0.8	220	65	18.38	18.13
5/8/14	8.5	0.6	228	58	11.69	11.60
6/16/14	8.7	0.5	220	60	34.35	---
8/20/14	8.5	0.3	220	62	15.97	14.90
10/28/14	8.5	0.9	166	45	25.24	14.96

**Azimuth angle is measured in degrees clockwise from magnetic North.*

***Incidence angle is measured from vertical. 0° = vertical motion, 90° = horizontal motion*

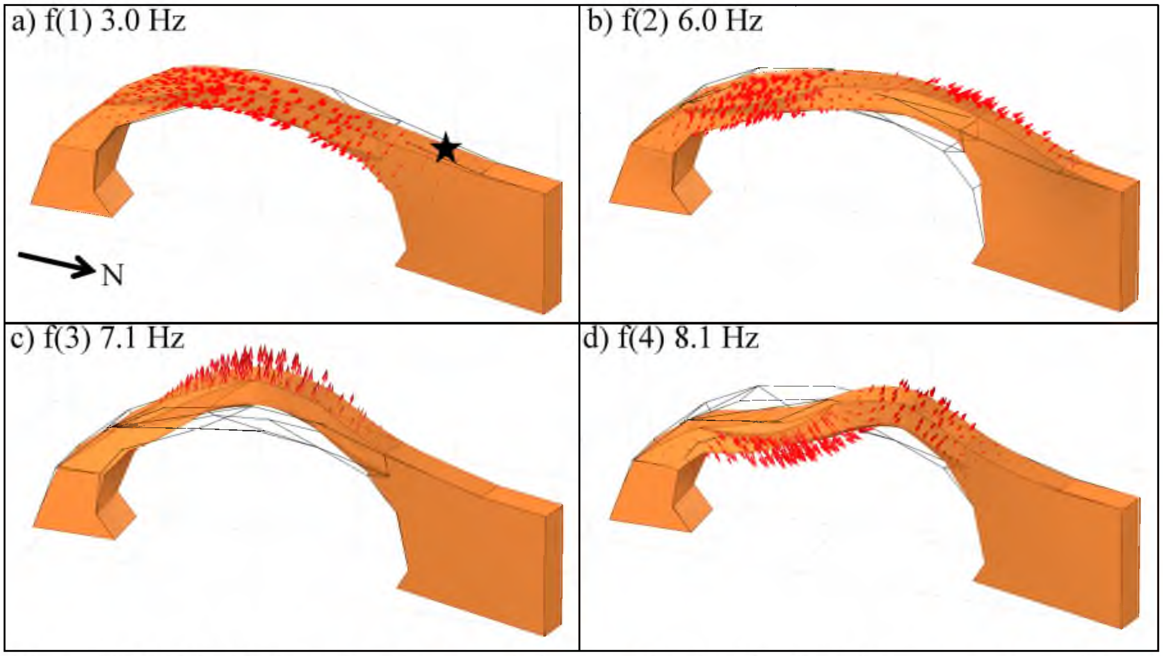

Figure 4.21 Modeled mode shapes and frequencies for the first four resonant modes of Mesa Arch. Arrows indicate displacement direction and are scaled by magnitude. The arch is oriented ~0°, with north to the right side of the images. Field data were taken from the position indicated by the star. a) First out-of-plane bending, b) Second out-of-plane bending, c) First in-plane bending, d) Second in-plane bending mode.

The first four resonant mode shapes and frequencies are shown in Figure 4.21 and in Table 4.7. We effectively matched the four predominant spectral peaks measured, and polarization analysis supports our interpretations (Figure 4.22). The modeled fundamental mode at 3.0 Hz represents the first out-of-plane bending mode in the orthogonal direction, which supports our measured frequency showing horizontal polarization. (Note: we define in- or out-of-plane with respect to the plane of the arch span.) Mode 2 represents the second out-of-plane bending mode modeled at 6.0 Hz, again with strong horizontal, orthogonal ground motion, and matching well with our measurements. Mode 3, the first in-plane bending mode modeled at 7.1 Hz, shows strong vertical motion, and Mode 4, the second in-plane bending mode modeled at 8.1 Hz, shows vertical and north-south motion, which matches well with our measurements.

Table 4.7: Comparison of measured and modeled resonant frequencies and polarization for Mesa Arch from the normal sensor position on the arch. DOP: degree of polarization.

Mode	Measured Frequency (Hz)	Modeled Frequency (Hz)	DOP [0-1]	Azimuth Measured (°)	Incidence Measured (°)	Azimuth / Incidence Modeled (°)
1	2.9 – 3.1	3.0	0.9 – 1.0	099 – 108	86 – 89	102 / 89
2	5.9 – 6.6	6.0	0.7 – 1.0	111 – 146	83 – 86	106 / 90
3	6.9 – 7.6	7.1	0.8 – 1.0	083 – 102	85 – 90	034 / 59
4	8.3 – 8.7	8.1	0.3 – 0.8	220 – 242	55 – 83	238 / 80

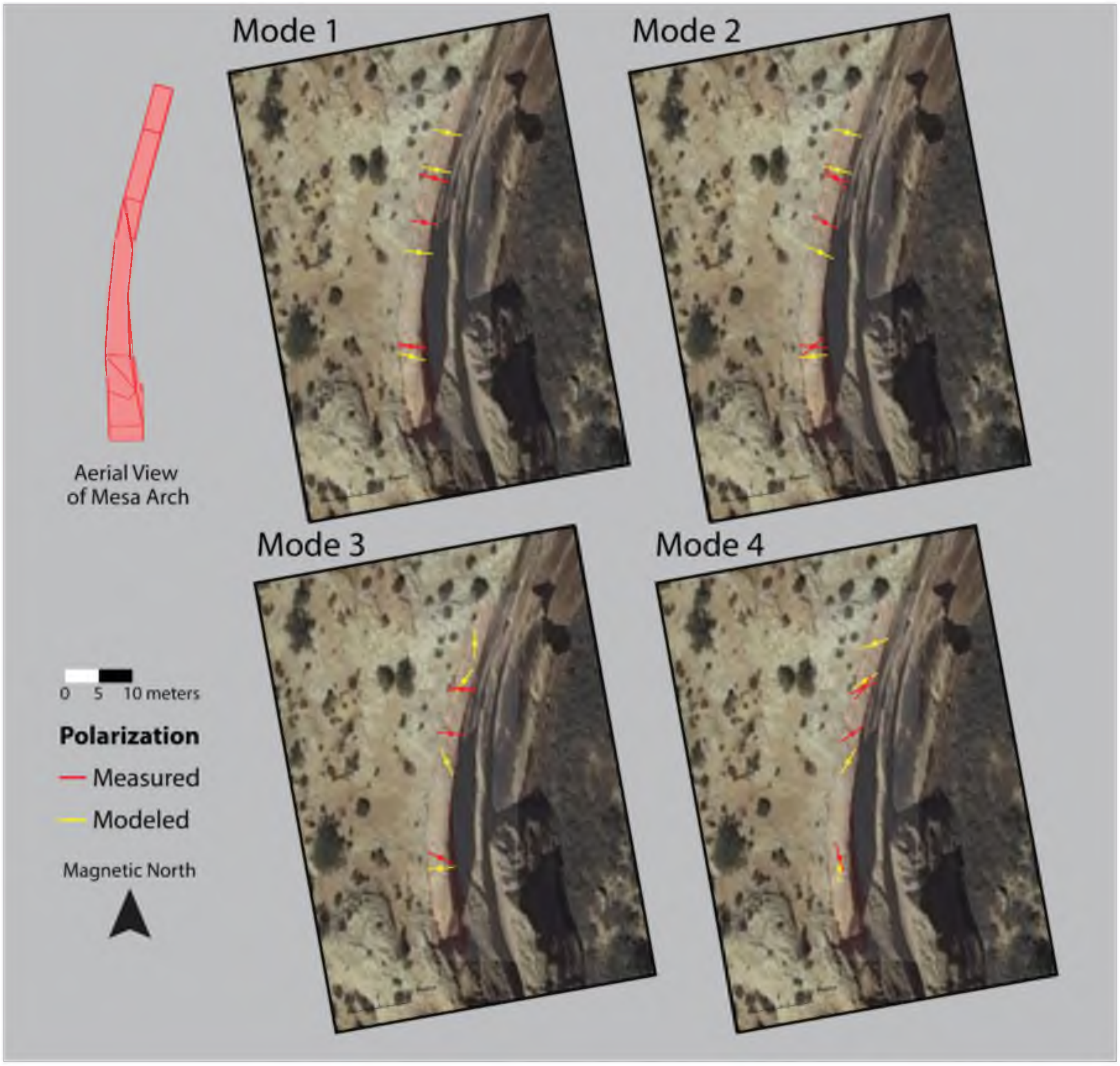

Figure 4.22 Comparison of measured polarization azimuths with model predictions.

4.4.6 Interpretation and Discussion

Mesa Arch is our most analyzed arch and the repeat measurements have proven invaluable for our research. The trend in Figure 4.18 shows that resonant frequency is directly correlated with rock temperature: an increase in temperature causes an increase in resonant frequency, with the third frequency showing the largest overall shift. The exception to this trend appears during times of extreme cold (below 0°C), where we see a large increase in fundamental frequency despite falling temperatures. This is interpreted as resulting from ice formation in the rock pore space, causing an increase in bulk material stiffness and making the arch vibrate at a higher frequency (as also in Bottelin et al., 2013). Future monitoring during the winter will support or refute this interpretation. Figure 4.18 and Figure 4.20 together demonstrate that minor variations in resonant frequencies are predominantly controlled by thermal effects, i.e., changes in bulk material stiffness as the rock expands and contracts. This mechanism is stress-stiffening. Tilt data from our 3-day test support this reasoning, showing daily deformations caused by thermo-elastic stresses that correlate well with resonant frequency shifts (Figure 4.20).

Overall, we find good agreement between measured data and model results, with modes 1, 2, and 4 matching all of the measured values. Only mode 3 appears not ideally represented in our model, as polarization results from some points do not match field measurements. With respect to frequency values, precise sensor placement has no measureable effect as long as the instrument is located on top of the arch. However, sensor placement does affect polarization measurements, and different locations can be selected to further explore and validate model predictions.

CHAPTER 5

CONCLUSION

5.1 Summary of Work and Results

The natural arches of Southern Utah continually undergo deterioration from harsh environmental conditions. In 2008, one of the arches unexpectedly collapsed. Without a means to quantitatively assess changes in the integrity of the arch, there was no way to predict this collapse. Research performed in this thesis is aimed at establishing the foundations of new methodology for monitoring the changing integrity of these natural landmarks. The approach builds on the concept of structural health monitoring, now commonly employed in civil engineering.

The four sites analyzed in detail here exhibited clear resonant frequencies ranging from ~2 - 10 Hz. The first resonant frequency *f1*, or fundamental frequency, was measured at each site and confirmed using 3D numerical modal analysis. It is noteworthy that most of the studied arches had very similar fundamental resonant frequencies, which is related to similar material properties and overall volume. Campaign-style monitoring with 10 measurements over more than a year at Mesa Arch did not reveal any irreversible variations in resonant frequency that may be linked to permanent damage. These repeat measurements, supplemented by short-term continuous monitoring, did, however, identify reversible resonant frequency fluctuations that we propose are related to temperature variations through a mechanism of thermal stiffening. We believe a similar mechanism operates at Mesa Arch during periods of prolonged cold weather, when small amounts of interstitial ice cause the rock to stiffen, increasing resonant frequencies.

Other key findings of this study include:

- Resonant properties of natural arches can be measured from ambient seismic data.
- Optimal results are achieved when the seismometer is placed directly on top of the structure being assessed. The ideal location of the sensor is in the center of the arch span, but minor variations in placement have little effect on the spectral content of ambient noise. Therefore, in repeat measurements, the sensor does not need to be placed in the exact same location during each deployment.
- The addition of tilt data was effective in supporting investigation of thermo-elastic effects; observed deformation confirms the temporal variation of thermal stresses and allows comparison with measured frequency shifts.
- Variations in resonant frequencies at some arches are controlled by thermal stiffening, i.e., changes in rock mass stiffness as the rock expands and contracts. This effect may be maximized when the arch is constrained against thermal expansion on both ends.
- Freezing temperatures can cause a measurable increase in resonant frequency, which we propose is caused by frozen water in the sandstone pore space, causing the arch to stiffen slightly.
- Numerical modal analysis is dependent on the assumed elastic modulus, density, and only slightly dependent on Poisson's ratio. Mechanical boundary conditions of the model (i.e., fixed and free locations) can be difficult to assess for some sites.

- Simplified 3D models appear to be generally sufficient for modal analysis in capturing the important resonance characteristics observed in measured data.
- Minor, reversible fluctuations in resonant frequency can be expected, related to environmental effects, which must be carefully quantified to assess the potential for detecting permanent change from resonant frequency monitoring.

5.2 Suggestions for Continued Research

Numerous opportunities exist for further research stemming from this study. These research possibilities develop from the successful moving tests and the 3-day measurement at Mesa Arch. First, additional seismometers were recently purchased, and deploying multiple sensors along the span of the arch will greatly help assessment of the different mode shapes of vibration. This will also aid in improved modal analysis by providing additional polarization constraints to verify the model. Second, performing additional continuous monitoring deployments would expand our understanding of reversible and irreversible changes exhibited by each arch. Visitor access to the top of the arches is no longer permitted in the parks, so Double O Arch and Landscape Arch are ideal candidates for long-term measurements, since the sensors are scarcely visible at these locations. While Corona Arch and Mesa Arch are also prime candidates for continuing measurements, there is no secure place to permanently position the sensors. However, 3-day tests at such locations multiple times throughout the year may prove sufficient. Each continuous deployment should incorporate tilt measurements to assist in further investigation of the arch’s response to thermal and hydrological perturbations at daily and annual time scales. The addition of permanent continuous monitoring will also provide real-time monitoring of the structures and may ultimately aid in visitor safety assessments. Continuation of this research has the potential to provide a wealth of future data to explore the dynamic life and demise of natural arches in southern Utah.

APPENDIX A

SITE DESCRIPTIONS AND RESULTS

A.1 Corona Arch

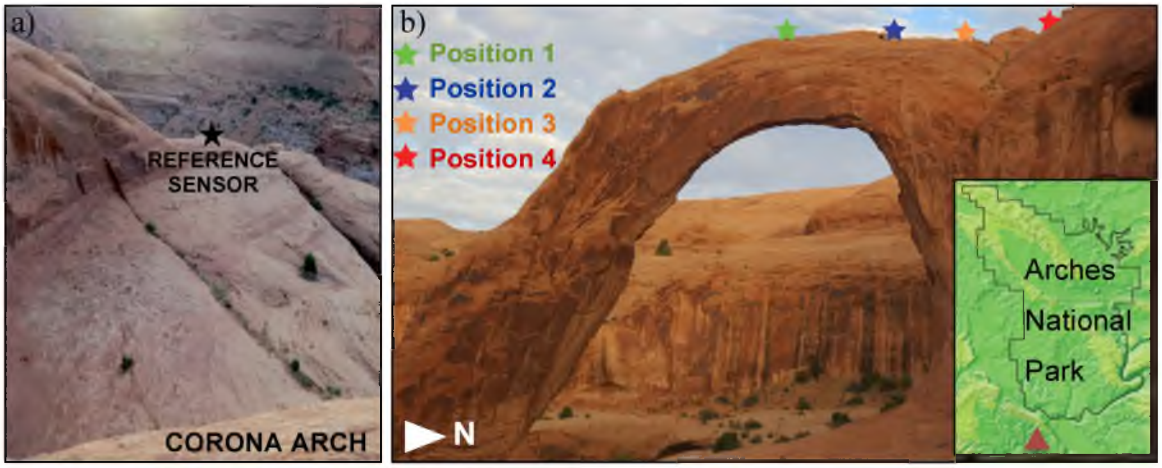

Figure A.1 Corona Arch near Moab, Utah: a) View from the top of the arch showing the reference sensor located ~100 m to the east. b) Side view of Corona Arch showing the different locations of the active sensor (indicated by stars) as it was moved during the August 16, 2013 deployment. Only one sensor was atop the arch, but was moved during deployment.

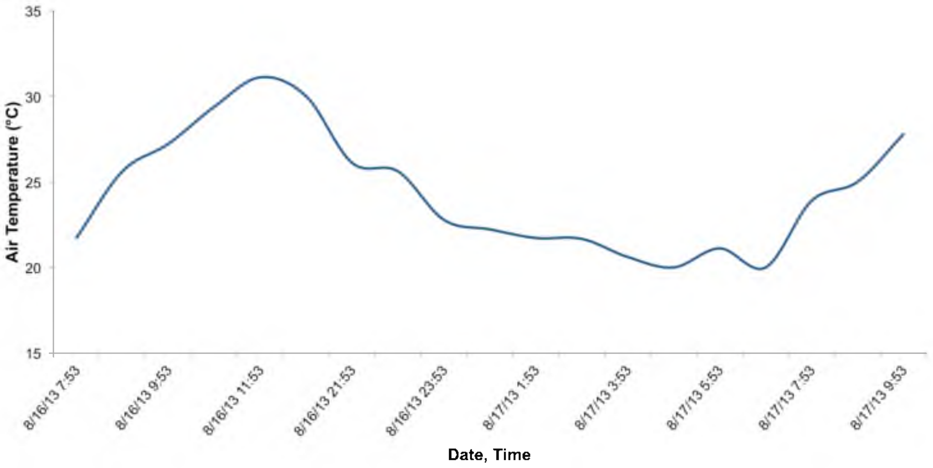

Figure A.2 Plot of air temperature over the 2-day test. The average air temperature was 27 °C on the 16th and 21 °C on the 17th.

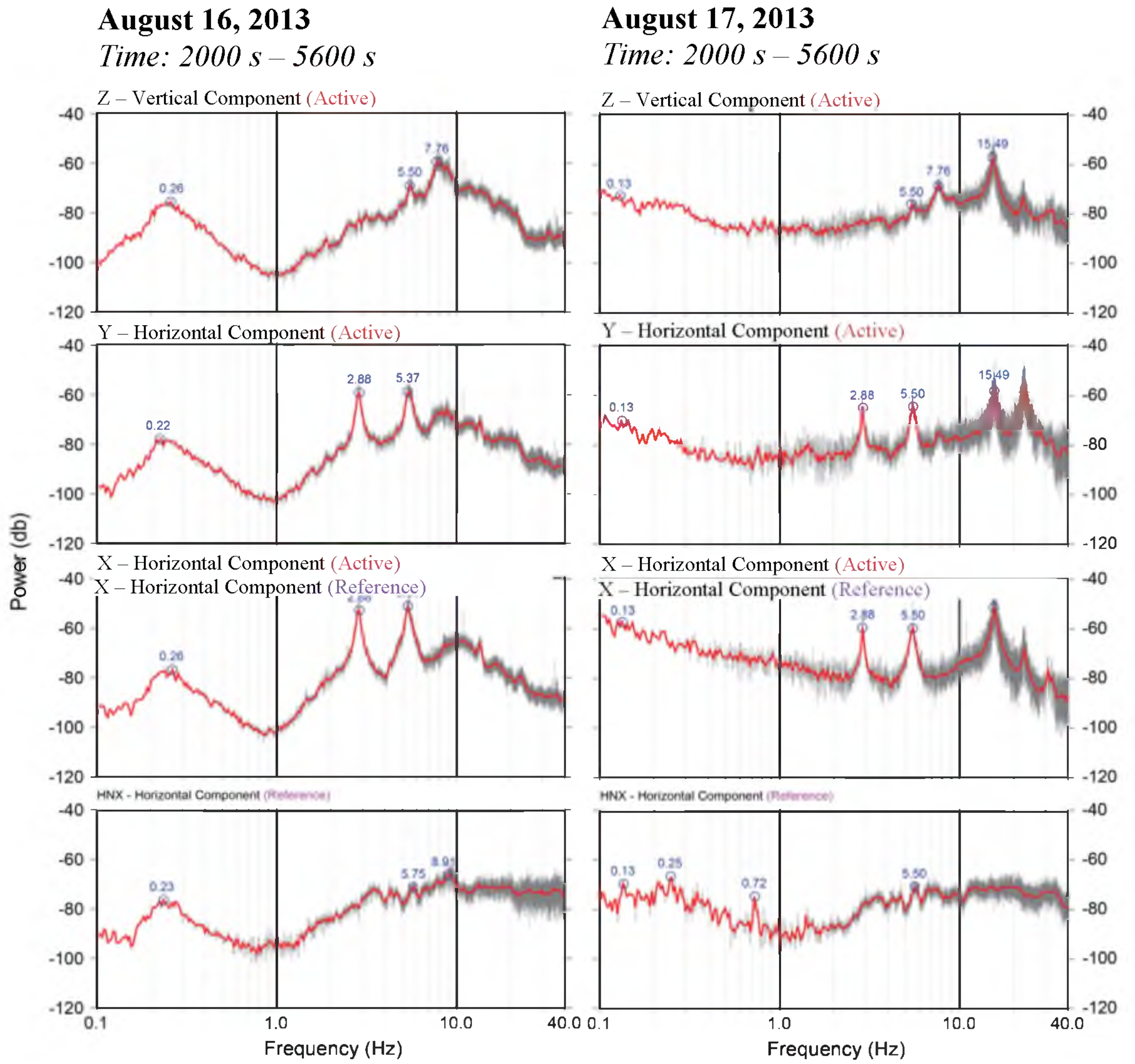

Figure A.3 Absolute power spectra for 1 h of 3-component ambient vibration data for the 16th and the 17th, 2000 s after start time; Z is vertical vibration, Y is north-south horizontal, X is east-west horizontal. The bottom plot is the east-west component of data from reference sensor. Gray traces show raw data, red are averaged.

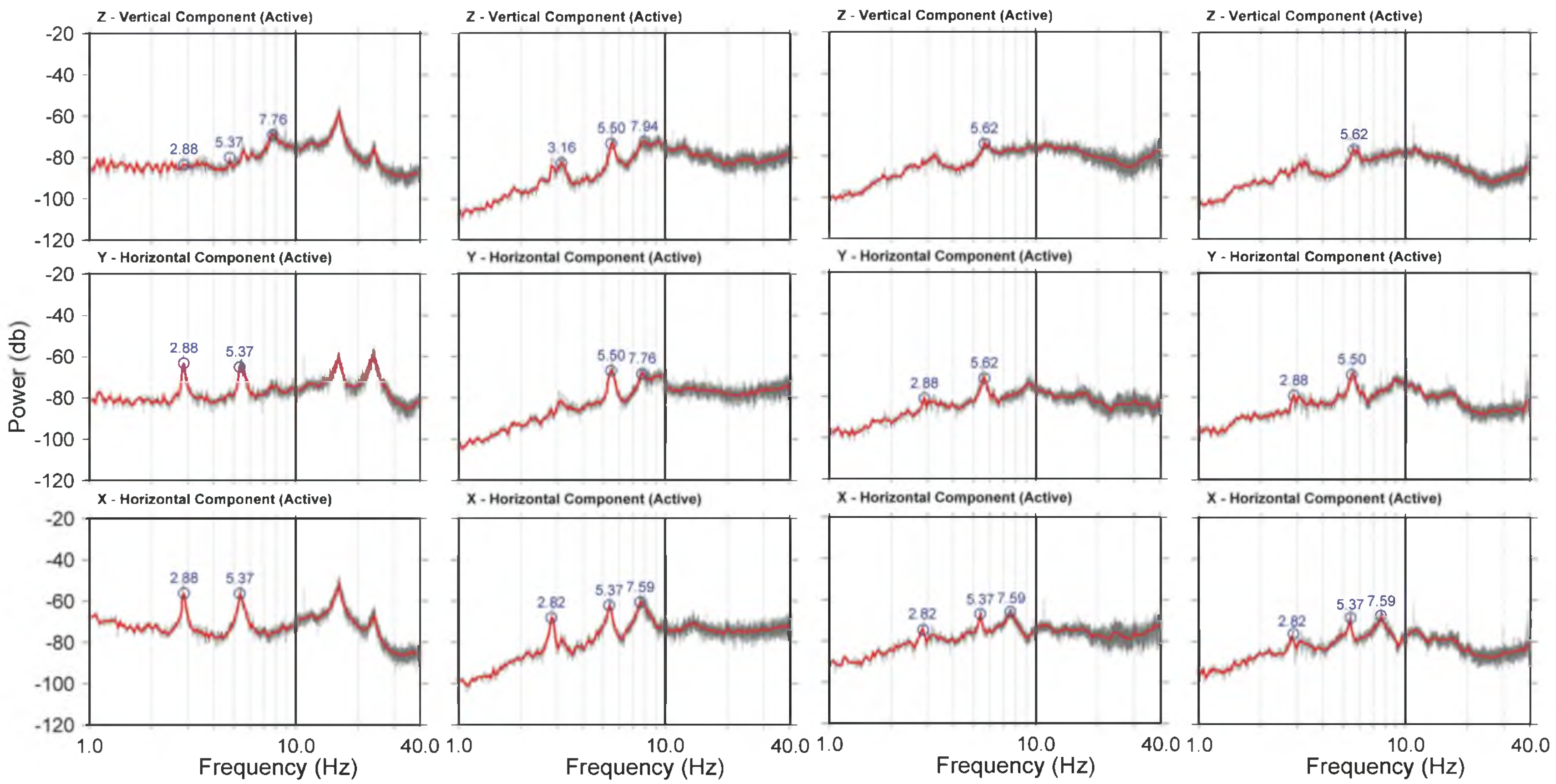

Figure A.4 Absolute power spectra for 30 min of 3-component ambient vibration data for each sensor location. Measures of power as a function of frequency are shown in units of $10\log_{10}(m^2s^{-4}Hz^{-1})$ for the vertical component (Z), north-south horizontal component (Y), and east-west horizontal component (X). The bottom plot is the east-west component of data from reference sensor.

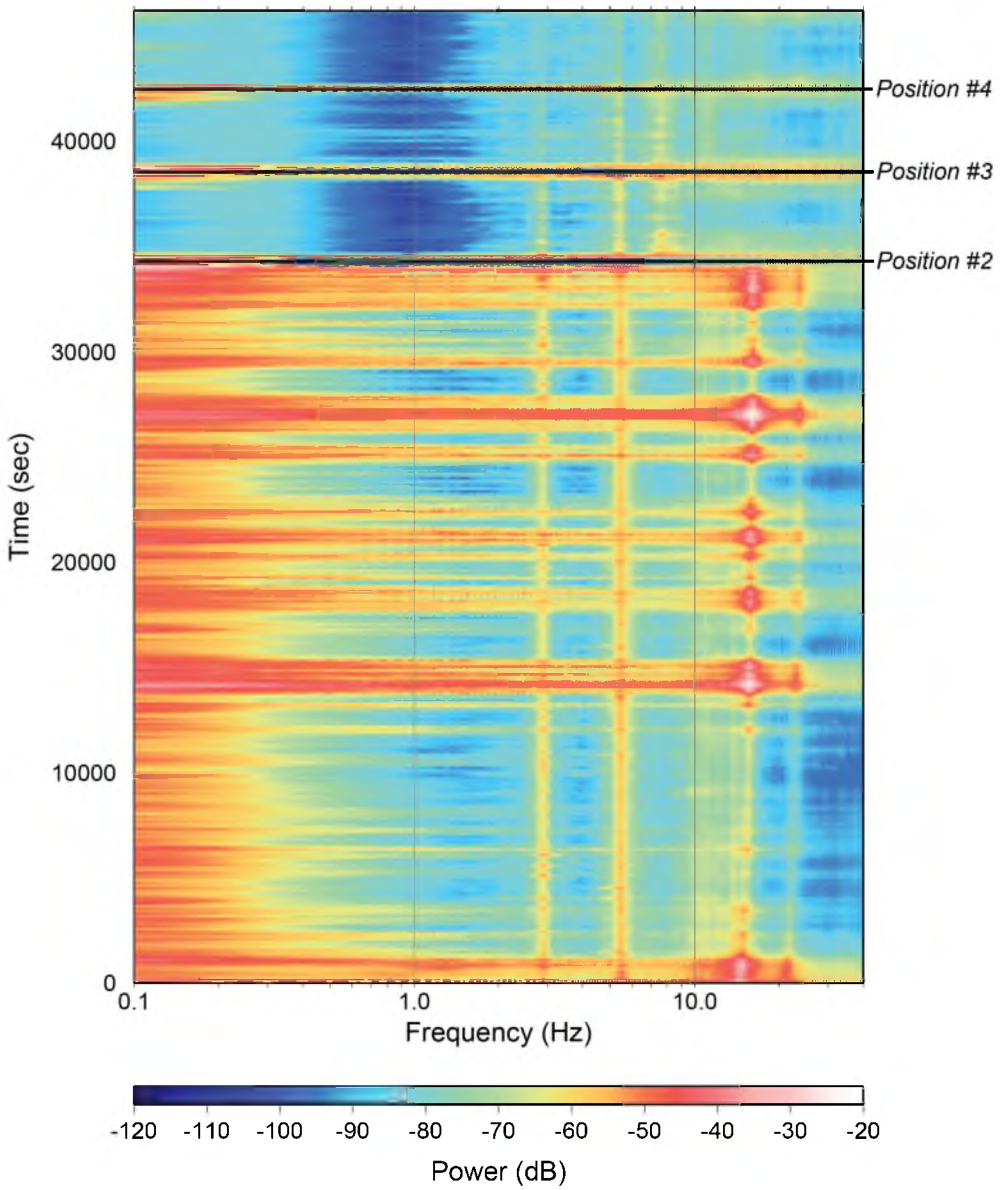

Figure A.5 Spectrogram for the east-west horizontal component for the overnight and moving tests. Higher powers (indicated by the continuous vertical lines) represent Corona Arch's main resonant modes. Measures of power as a function of frequency are shown in units of $10\log_{10}(m^2s^{-4}Hz^{-1})$.

Table A.1: Measured spectral peaks with predominant polarization orientation noted.

Measured Frequency (Hz)	**Degree of Polarization**	**Dominant Azimuth*** (°)	**Incidence Angle**** (°)
2.8	1.0	066	89
5.5	0.9	063	85
7.7	0.7	025	15

**Azimuth angle measured in degrees clockwise from magnetic North*

***Incidence angle measured from vertical. 0° = vertical motion, 90° = horizontal motion*

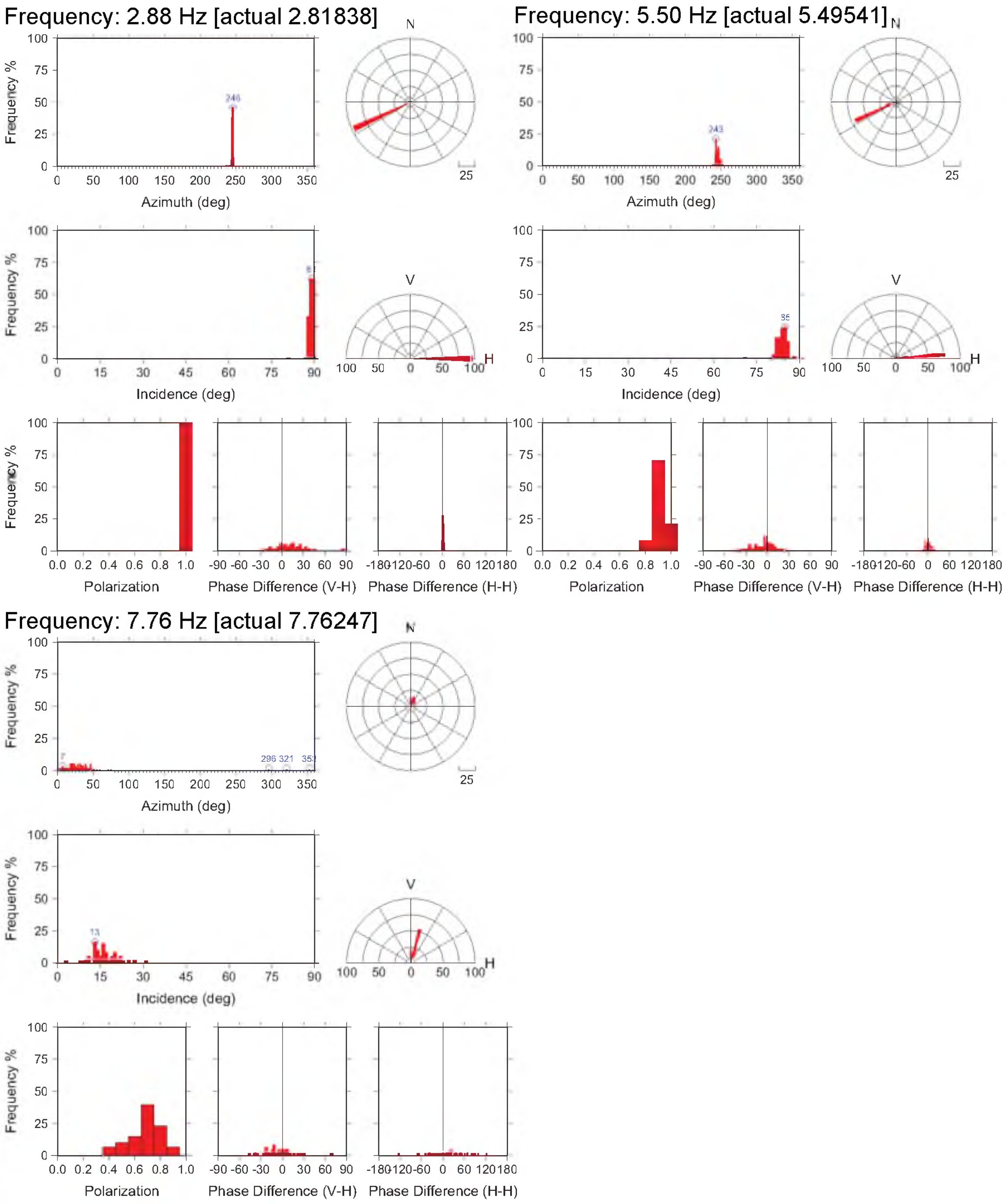

Figure A.6 Polarization plots for each measured frequency at Corona Arch. The data are taken from the hour-long segment (2000 s – 5600 s) from August 16, 2013, but are representative of the entire dataset. The plots display the azimuth, incidence angle, polarization, and phase difference between the vertical and horizontal and the two horizontal components.

A.2 Double O Arch

October 25, 2013

Figure A.7 Double O Arch in Arches National Park, Utah: a) The two locations of the sensor (indicated by stars) during the test. Both sensors were atop the arch the entire time. b) View of the top of the arch showing the two sensors.

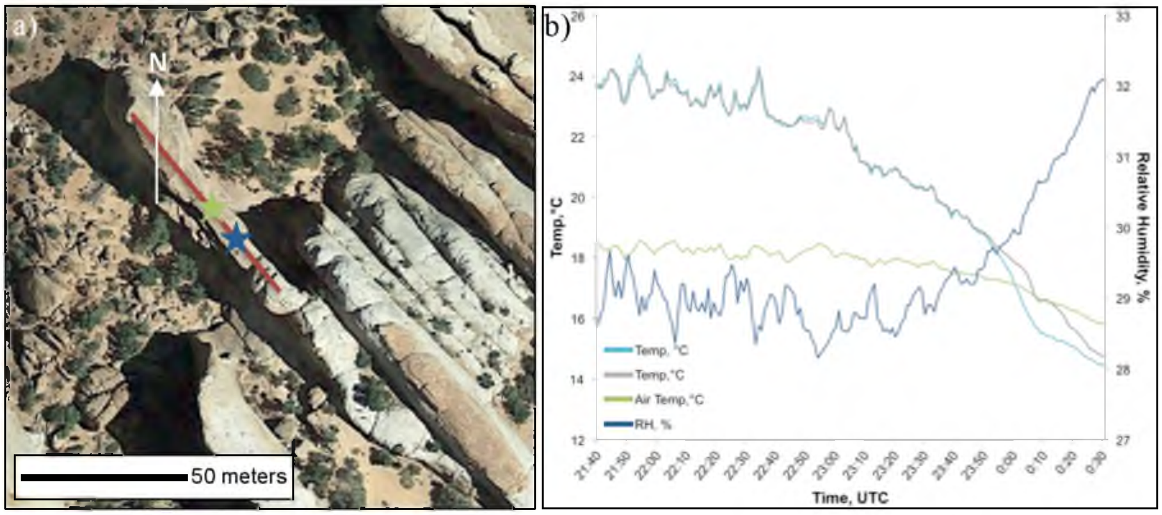

Figure A.8 Further analysis of Double O Arch: a) Aerial view of Double O Arch with the two sensors. The arch is north-west/south-east trending. b) Plot of the rock temperature, air temperature, and relative humidity for the entire test.

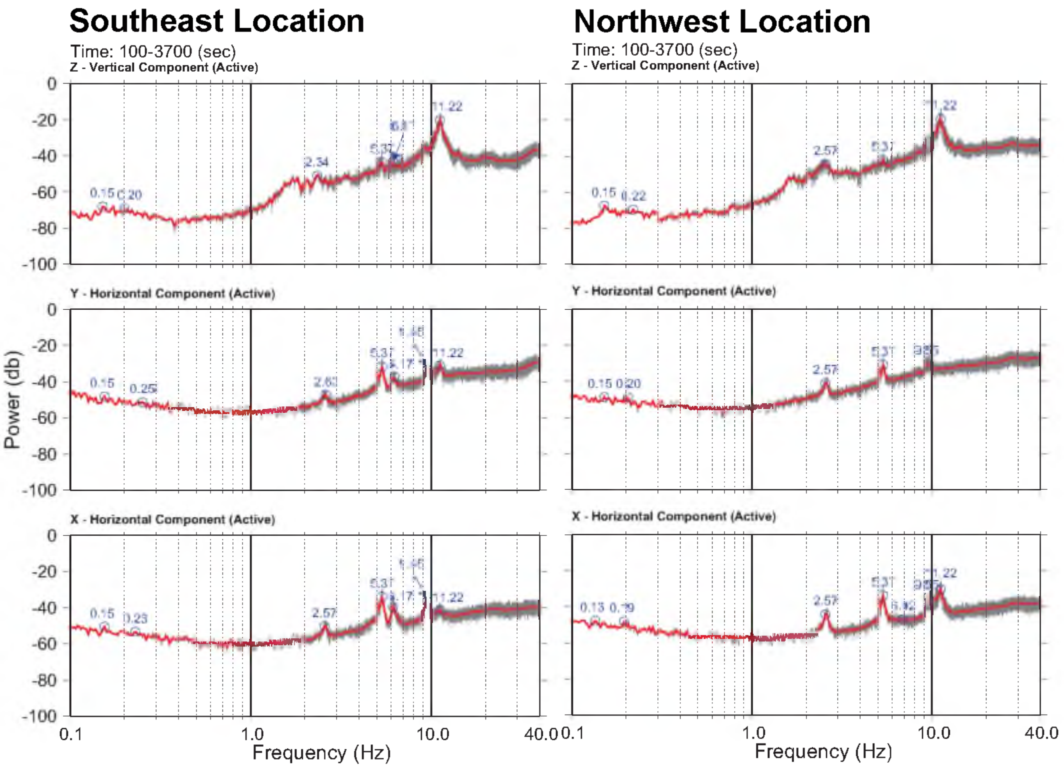

Figure A.9 Absolute power spectra for 1 h of 3-component ambient vibration data 100 s after start time. Measures of power as a function of frequency are shown in units of $10\log_{10}(m^2s^{-4}Hz^{-1})$ for the vertical component (Z), N-S horizontal component (Y), and E-W horizontal component (X). Gray traces show raw data, red are averaged.

Table A.2: Measured spectral peaks for southeast location.

Measured Frequency (Hz)	Degree of Polarization	Dominant Azimuth* (°)	Incidence Angle** (°)
2.6	0.7	037	78
5.4	0.9	038	80
6.2	0.7	040	72
9.5	0.6	040	71

Table A.3: Measured spectral peaks for northwest location.

Measured Frequency (Hz)	Degree of Polarization	Dominant Azimuth* (°)	Incidence Angle** (°)
2.6	0.75	030	73
5.4	0.8	035	70
6.9	0.9	010	66
9.5	0.9	031	66

**Azimuth angle measured in degrees clockwise from magnetic North*

***Incidence angle measured from vertical. 0° = vertical motion, 90° = horizontal motion*

a) *Southeast Location*

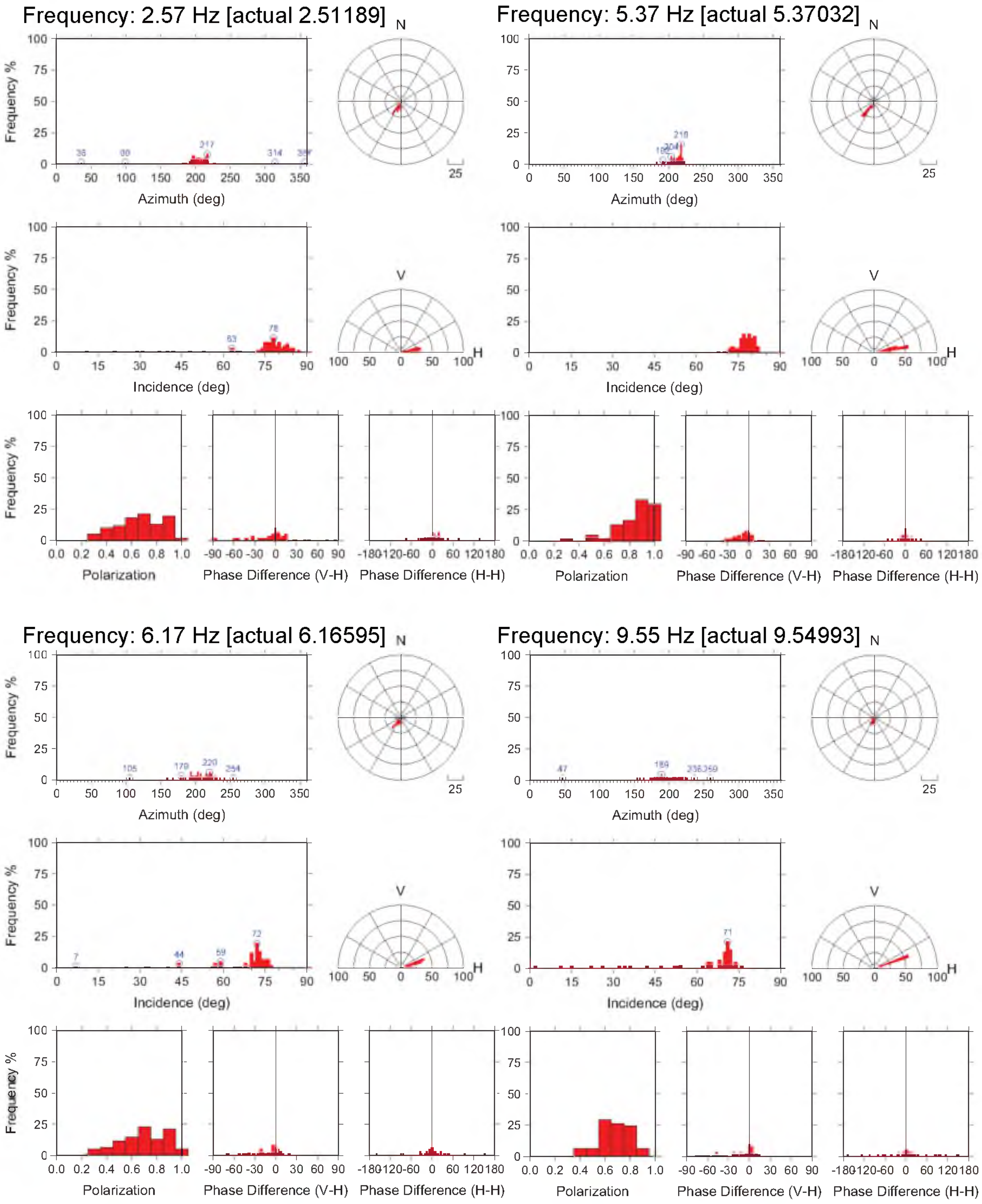

Figure A.10 Polarization plots for each measured frequency at Double O Arch. a) Data from the hour-long segment (100 s – 3700 s) from the southeast location. b) Data from the hour-long segment (100 s – 3700 s) from the northwest location. The plots display the azimuth, incidence angle, polarization, and phase difference between the vertical and horizontal and the two horizontal components.

b) *Northwest Location*

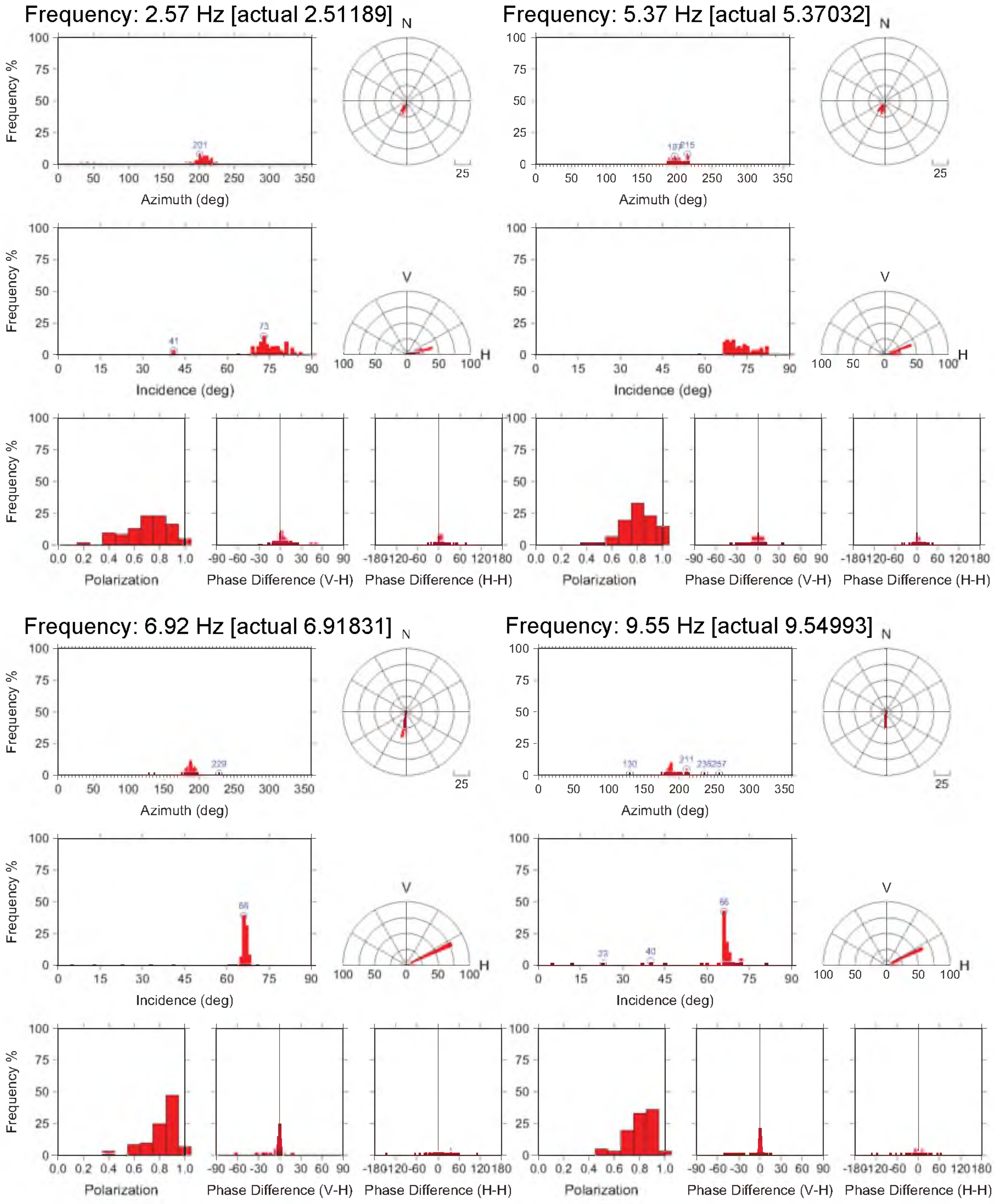

Frequency: 2.57 Hz [actual 2.51189]

Frequency: 5.37 Hz [actual 5.37032]

Frequency: 6.92 Hz [actual 6.91831]

Frequency: 9.55 Hz [actual 9.54993]

Figure A.10 (continued)

May 20, 2014

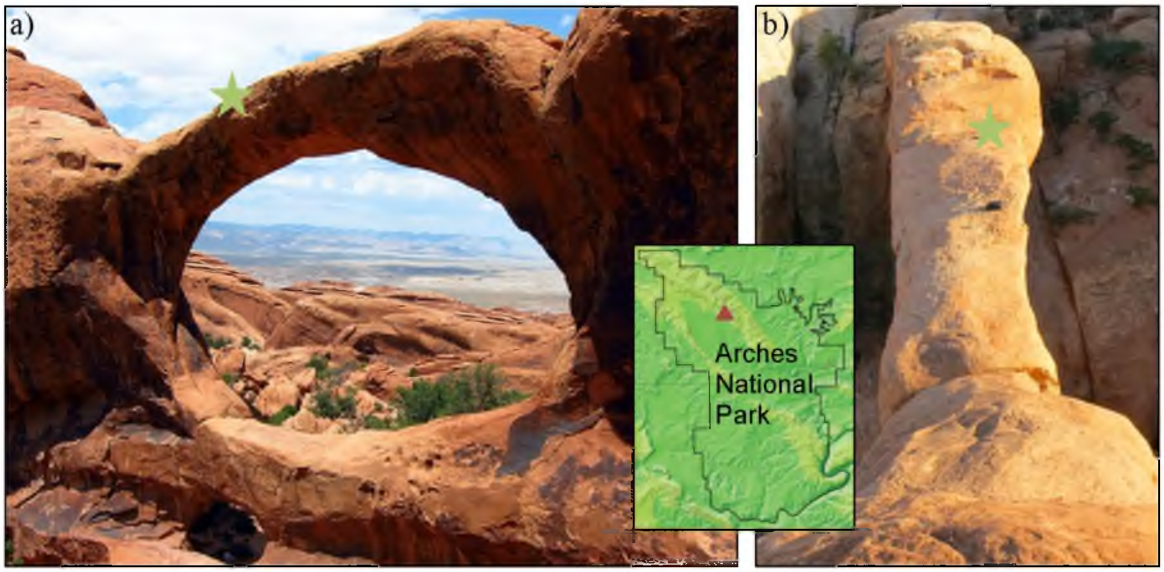

Figure A.11 Double O Arch in Arches National Park, Utah: a) The location of the sensor (indicated by green star) during the test. b) View of the top of the arch.

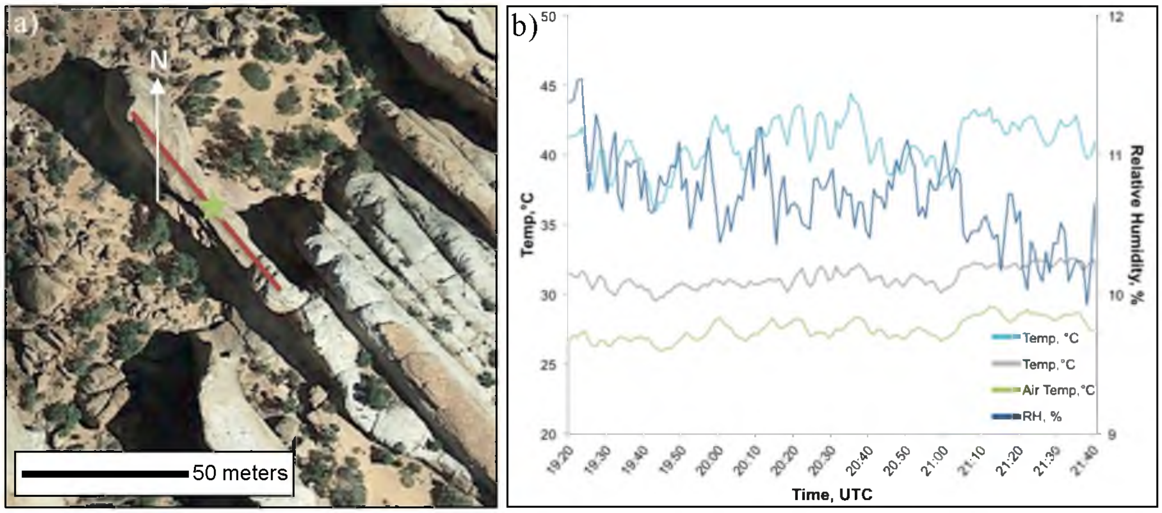

Figure A.12 Further analysis of Double O Arch: a) Aerial view of Double O Arch with the sensor location. The arch is north-west/south-east trending. b) Plot of the rock temperature, air temperature, and relative humidity for the entire test.

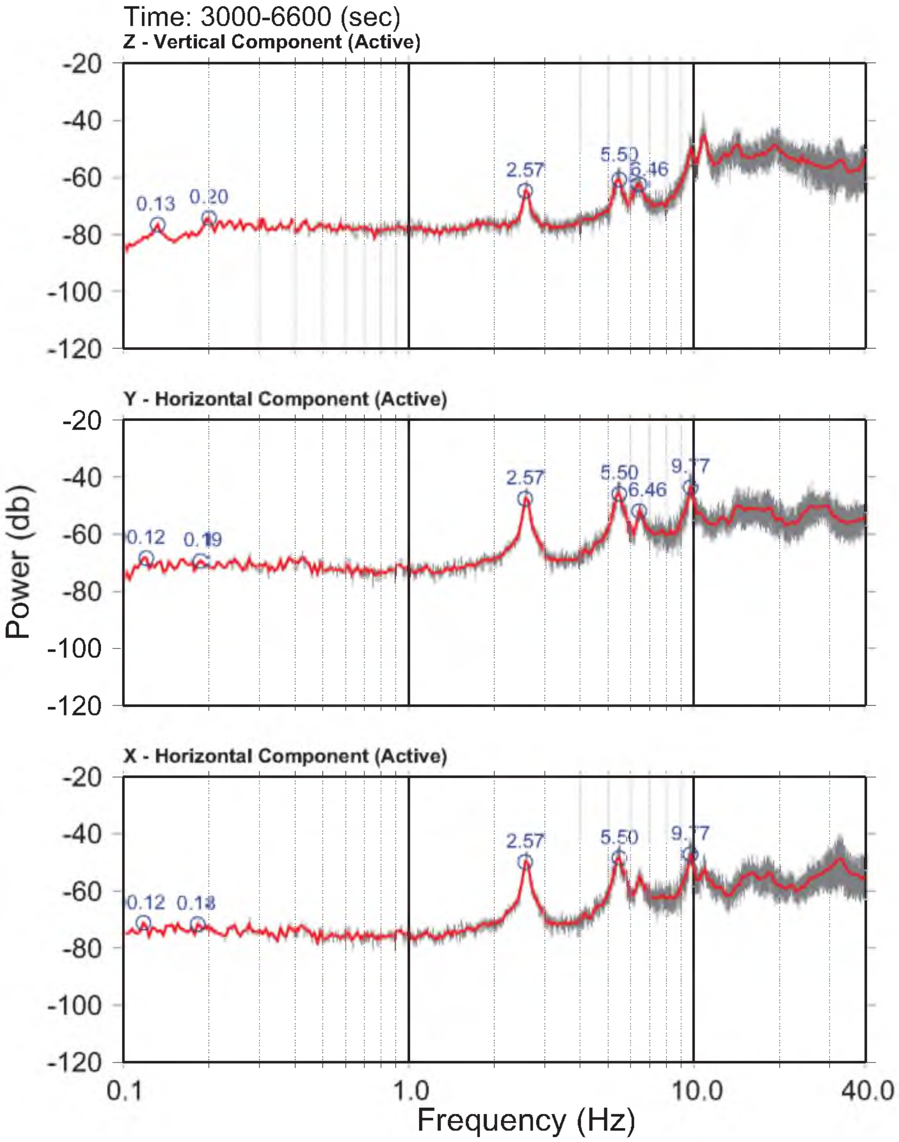

Figure A.13 Absolute power spectra for 1 h of 3-component ambient vibration data 3000 s after the start time. Measures of power as a function of frequency are shown in units of $10\log_{10}(m^2s^{-4}Hz^{-1})$ for the vertical component (Z), N-S horizontal component (Y), and E-W horizontal component (X). Gray traces show raw data, red are averaged.

Table A.4: Measured spectral peaks with predominant polarization orientation noted.

Measured Frequency (Hz)	Degree of Polarization	Dominant Azimuth* (°)	Incidence Angle** (°)
2.6	1.0	037	84
5.4	1.0	036	82
6.5	0.9	035	77
9.8	1.0	033	68

**Azimuth angle measured in degrees clockwise from magnetic North*

***Incidence angle measured from vertical. 0° = vertical motion, 90° = horizontal motion*

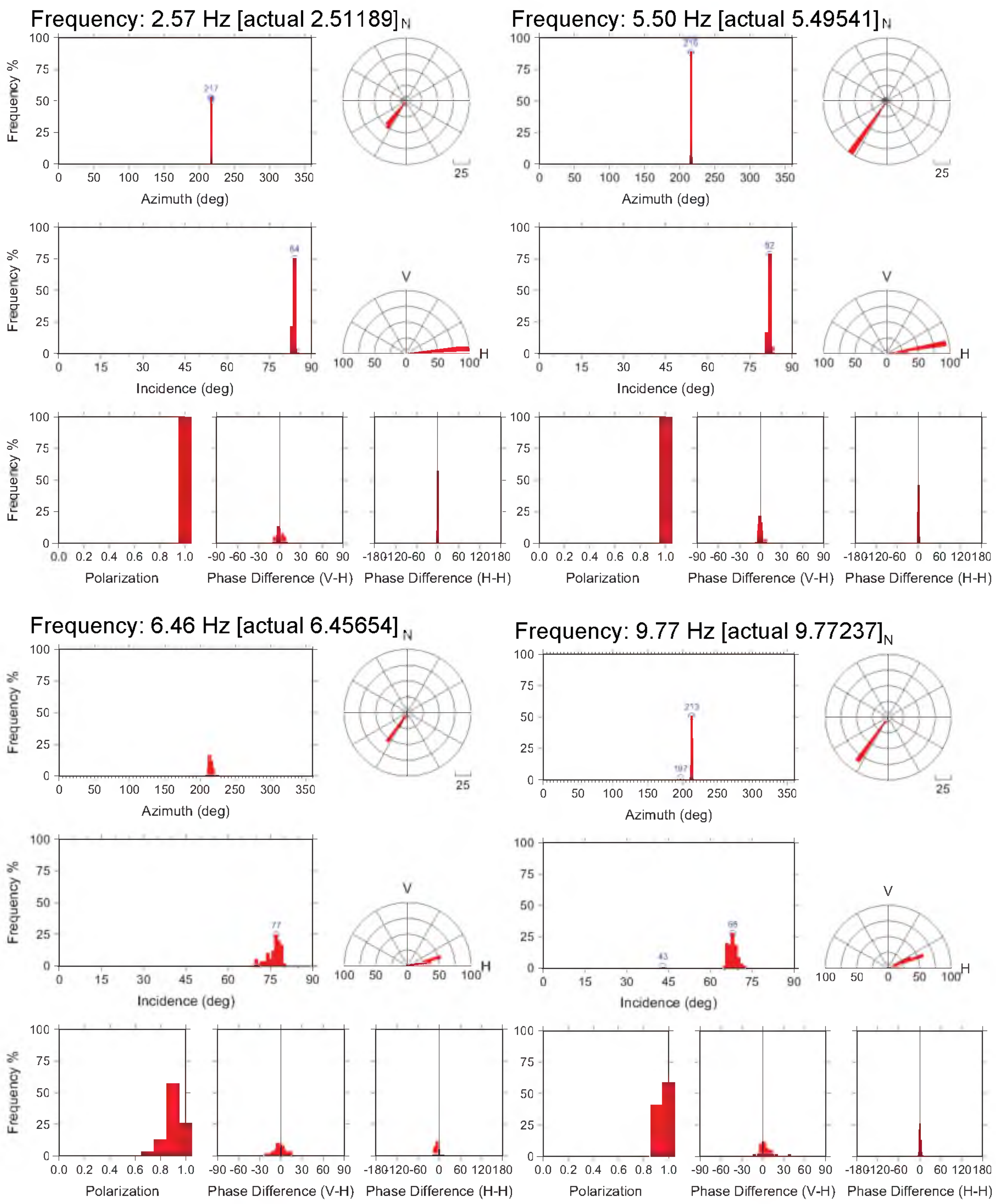

Figure A.14 Polarization plots for each measured frequency at Double O Arch from the hour-long segment (3000 s – 6600 s). The plots display the azimuth, incidence angle, polarization, and phase difference between the vertical and horizontal and the two horizontal components.

A.3 Landscape Arch

Figure A.15 Landscape Arch in Arches National Park, Utah: Our sensor was located at the base of the arch (indicated by the white arrow). b) View from underneath the arch.

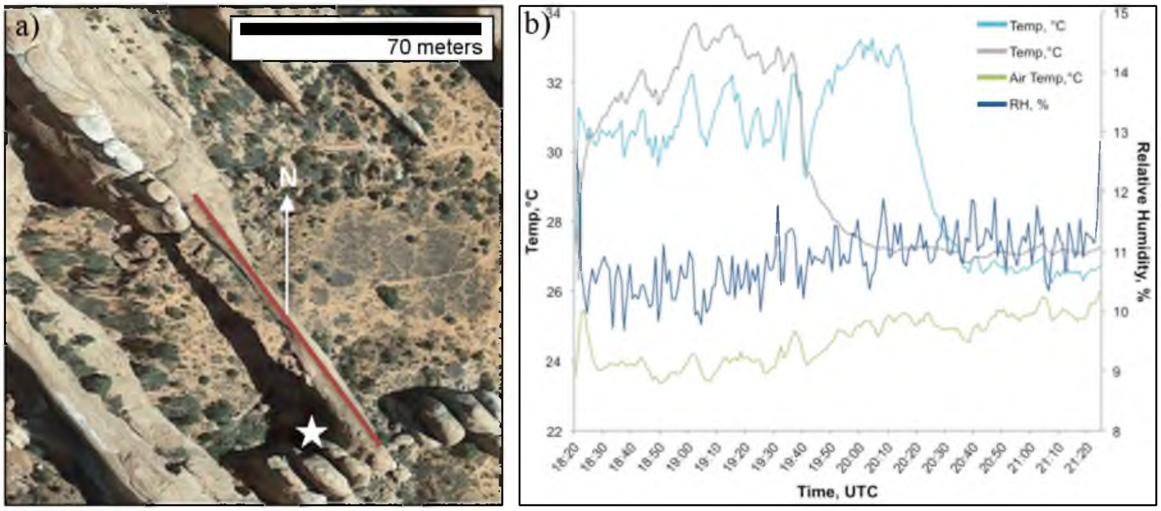

Figure A.16 Further analysis of Landscape Arch: a) Aerial view of Landscape Arch with the sensor location indicated by the white star. The arch is north-west/south-east trending. b) Plot of the rock temperature, air temperature, and relative humidity for the entire test.

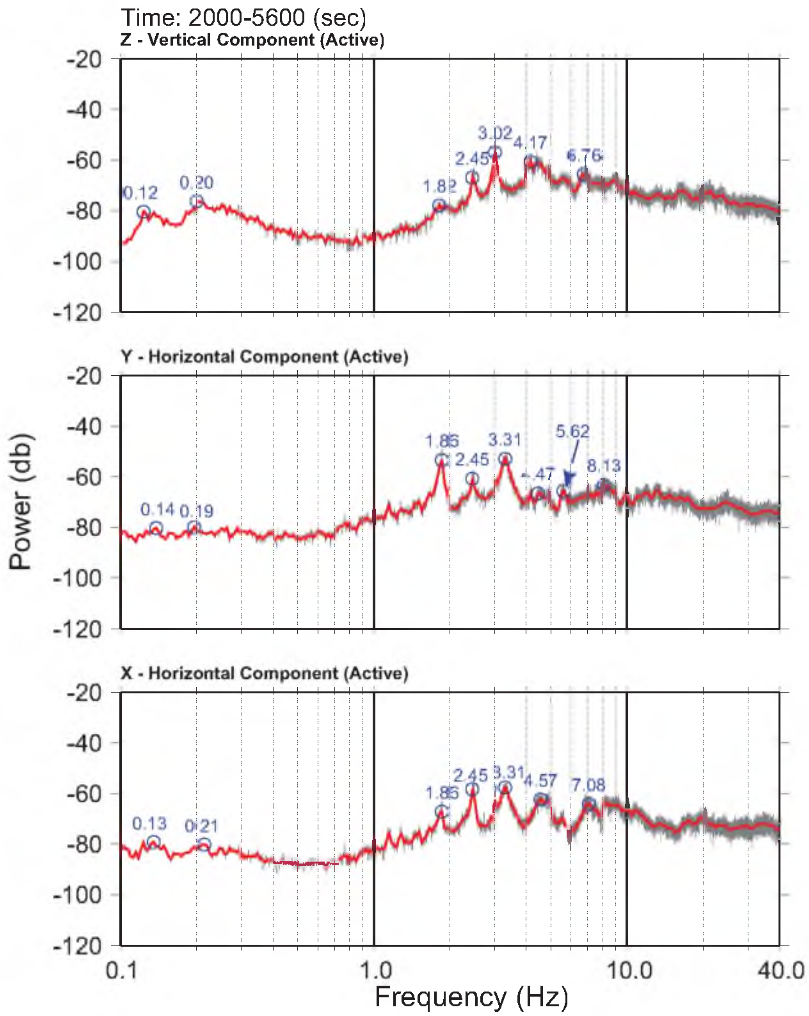

Figure A.17 Absolute power spectra for 1 h of 3-component ambient vibration data (18:53 – 19:53). Z is vertical vibration, Y is north-south horizontal, X is east-west horizontal. Gray traces show raw data, red are averaged.

Table A.5: Measured spectral peaks with predominant polarization orientation noted.

Measured Frequency (Hz)	Degree of Polarization	Dominant Azimuth* (°)	Incidence Angle** (°)
1.9	1.0	013	90
2.5	0.9	053	73
3.0	0.4	034	22
3.3	0.9	030	89
4.2	0.7	150	30
4.6	0.8	121	46
5.6	0.7	030	49

**Azimuth angle measured in degrees clockwise from magnetic North*

***Incidence angle measured from vertical. 0° = vertical motion, 90° = horizontal motion*

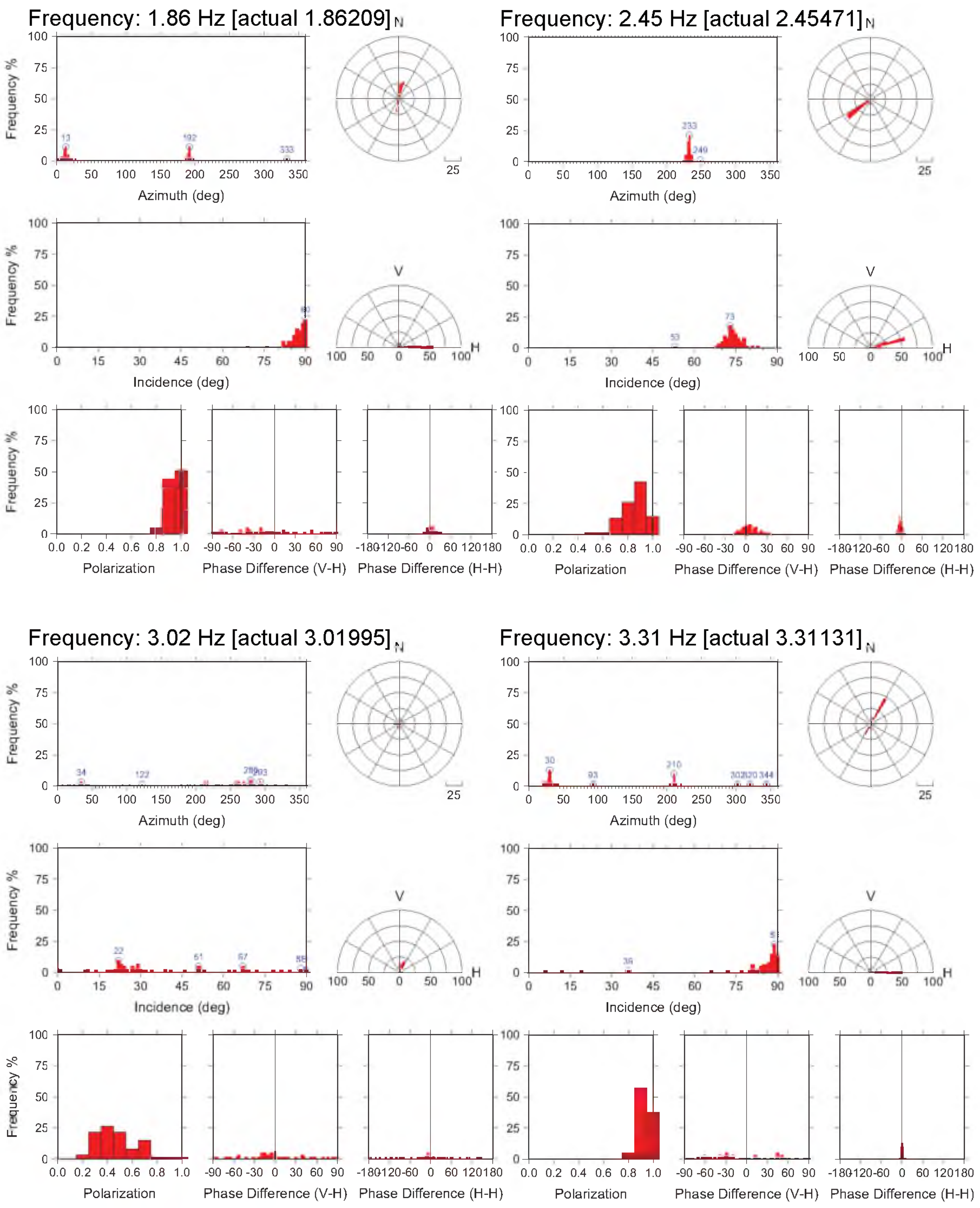

Figure A.18 Polarization plots for each measured frequency at Landscape Arch from the hour-long segment (2000 s – 5600 s). The plots display the azimuth, incidence angle, polarization, and phase difference between the vertical and horizontal and the two horizontal components.

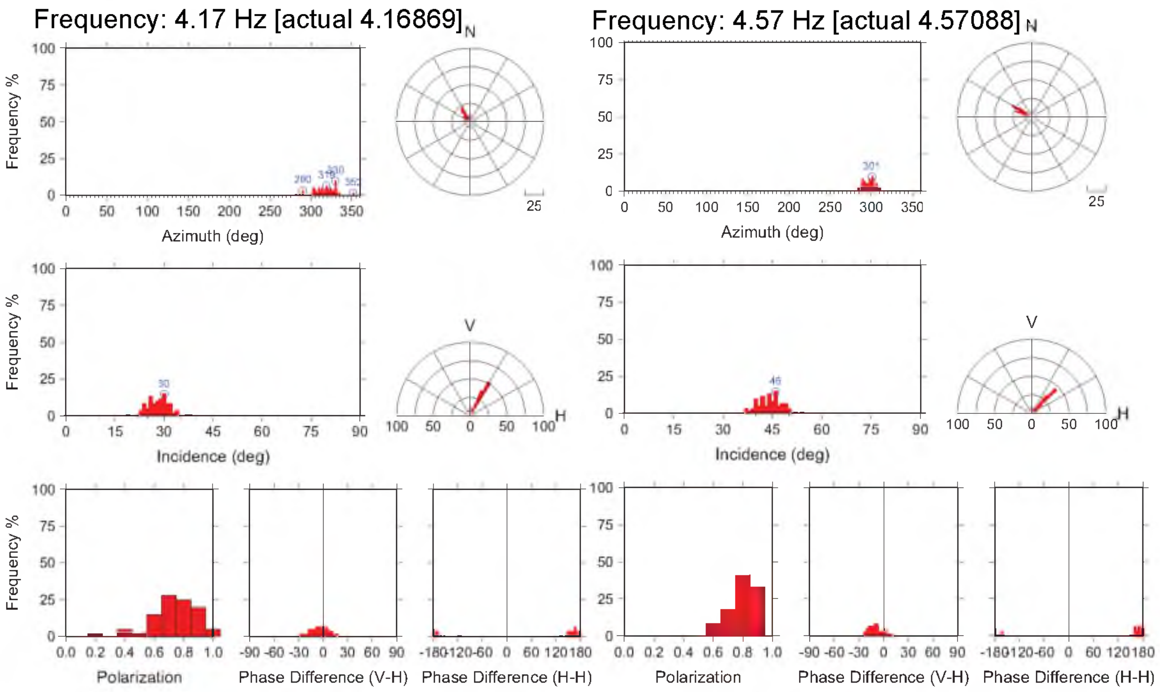
Frequency: 4.17 Hz [actual 4.16869]

Frequency: 4.57 Hz [actual 4.57088]

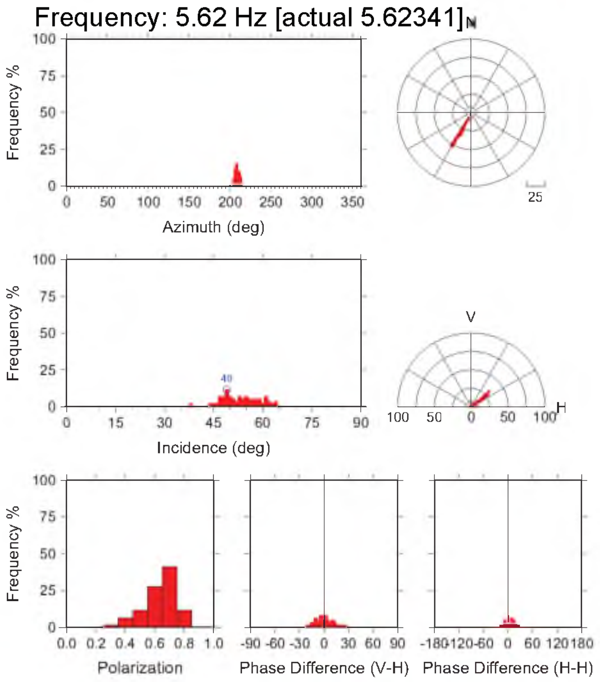
Frequency: 5.62 Hz [actual 5.62341]

Figure A.18 (continued)

A.4 Mesa Arch

September 28, 2013

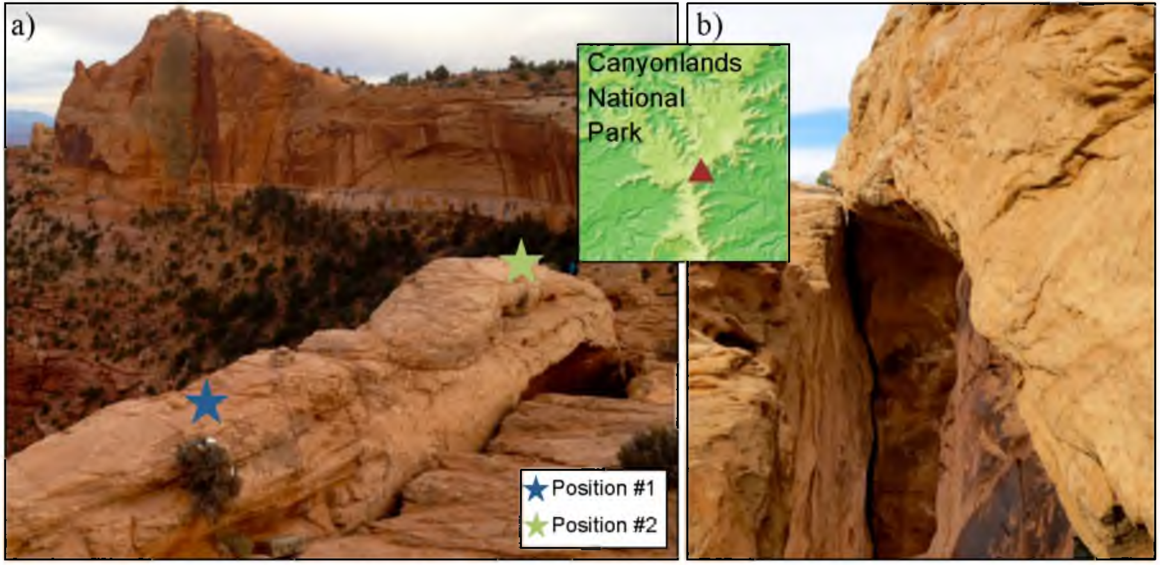

Figure A.19 Mesa Arch in Canyonlands National Park, Utah: a) Different locations of the active sensor (indicated by stars) as it was moved during the September 28, 2013 deployment. Only one sensor was atop the arch, but was moved during deployment. b) Side view of the arch showing it peeling away from the cliff.

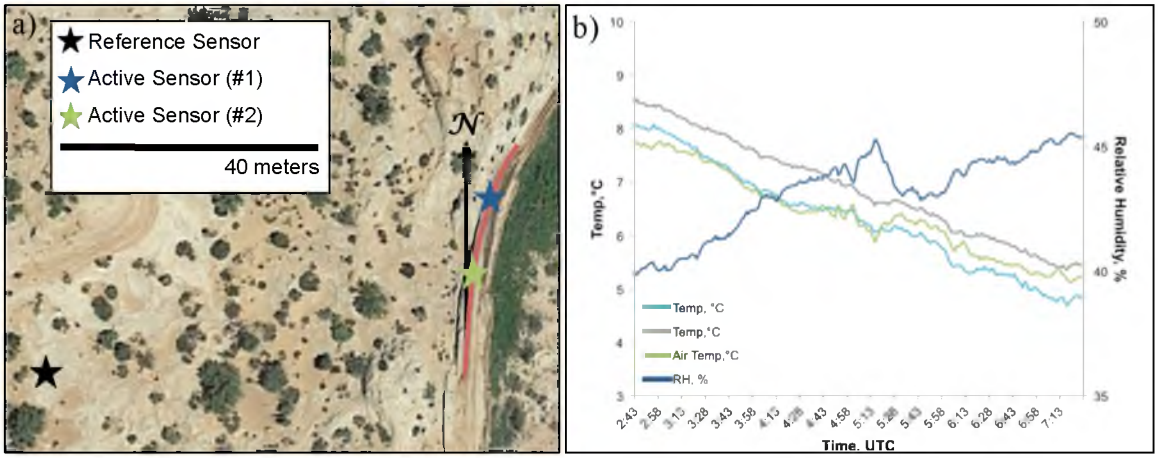

Figure A.20 Further analysis of Mesa Arch: a) Aerial view of Mesa Arch with the different locations of the active sensor and the reference sensor. The arch is north trending (second sensor location), but bends slightly to the east (first sensor location). b) Plot of the rock temperature, air temperature, and relative humidity for the entire test.

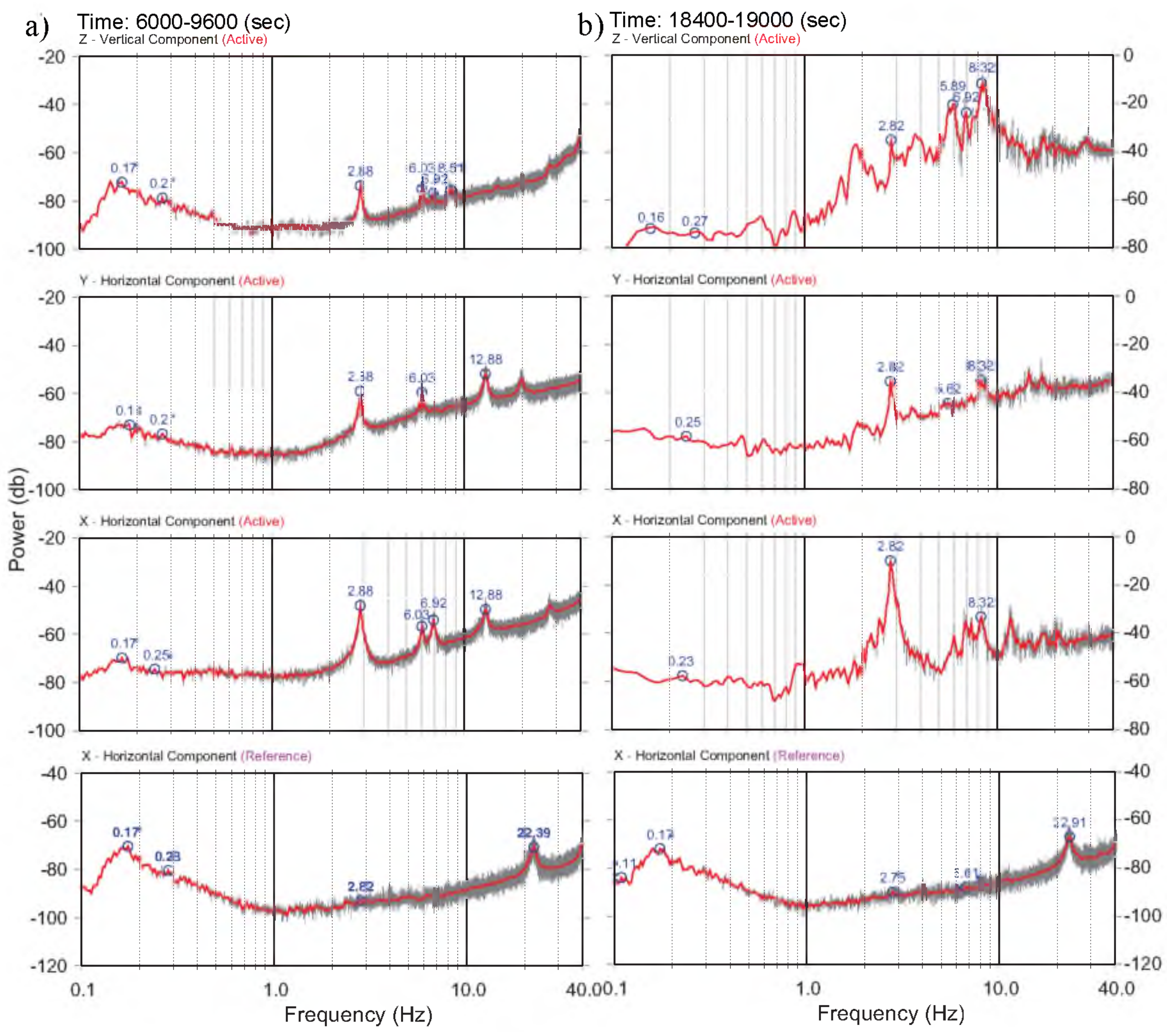

Figure A.21 Absolute power spectra for 3-component ambient vibration data. Z is vertical vibration, Y is north-south horizontal, X is east-west horizontal. The bottom plot is east-west component of data from the reference sensor. Gray traces show raw data, red are averaged. a) Data from 1 h from the first test. b) Data from 10 min from the second test.

Table A.6: Measured spectral peaks with predominant polarization orientation noted.

Measured Frequency (Hz)	Degree of Polarization	Dominant Azimuth* (°)	Incidence Angle** (°)
2.8	1.0	106	87
6.0	0.8	126	85
6.9	0.9	096	86
8.3	0.4	067	70

**Azimuth angle measured in degrees clockwise from magnetic North*

***Incidence angle measured from vertical. 0° = vertical motion, 90° = horizontal motion*

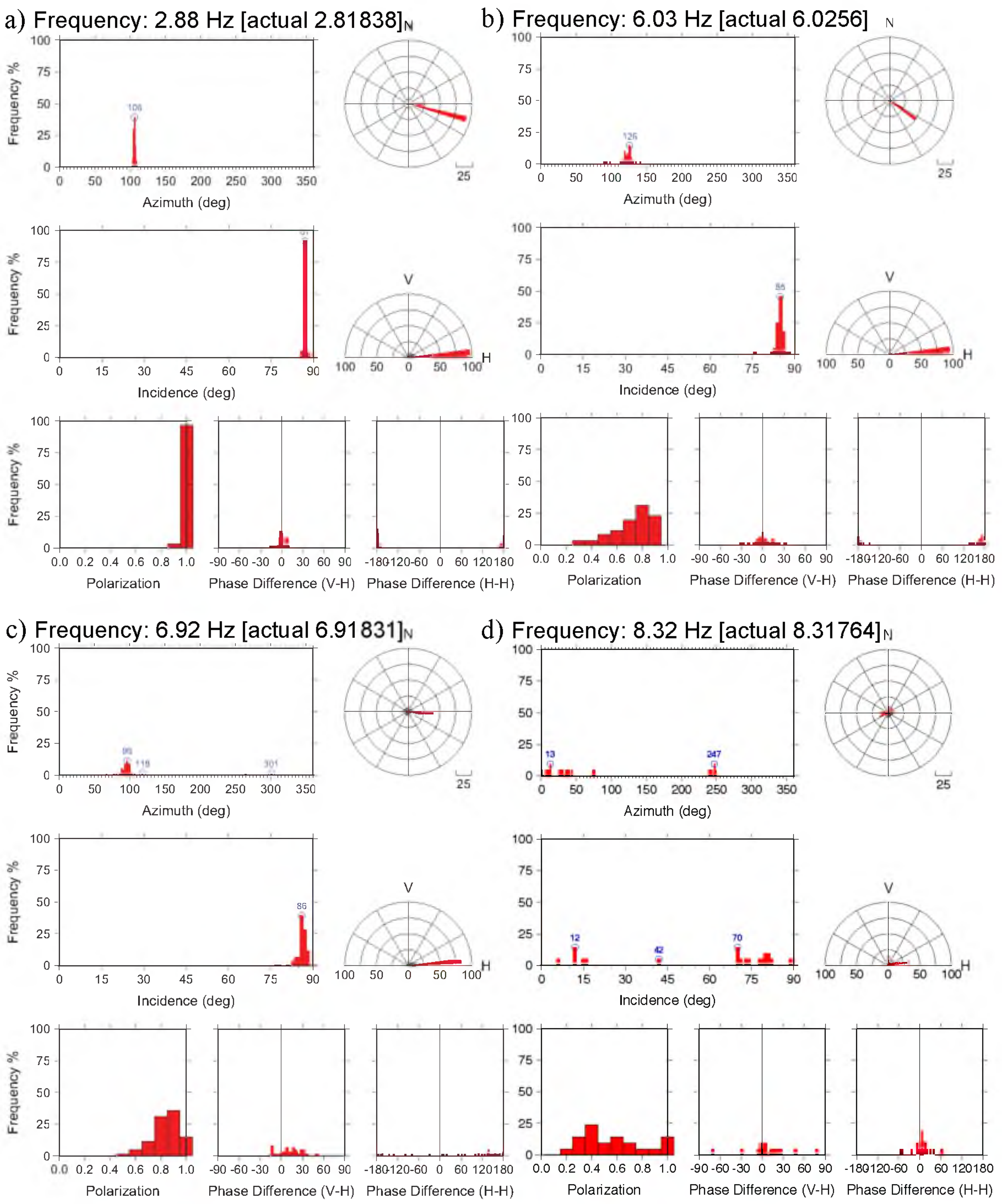

Figure A.22 Polarization plots for each measured frequency at Mesa Arch. a-c) Data from the hour-long segment (6000 s – 9600 s) from the first test. d) Data from the second test (0 – 1200 s). The plots display the azimuth, incidence angle, polarization, and phase difference between the vertical and horizontal and the two horizontal components.

December 13, 2013

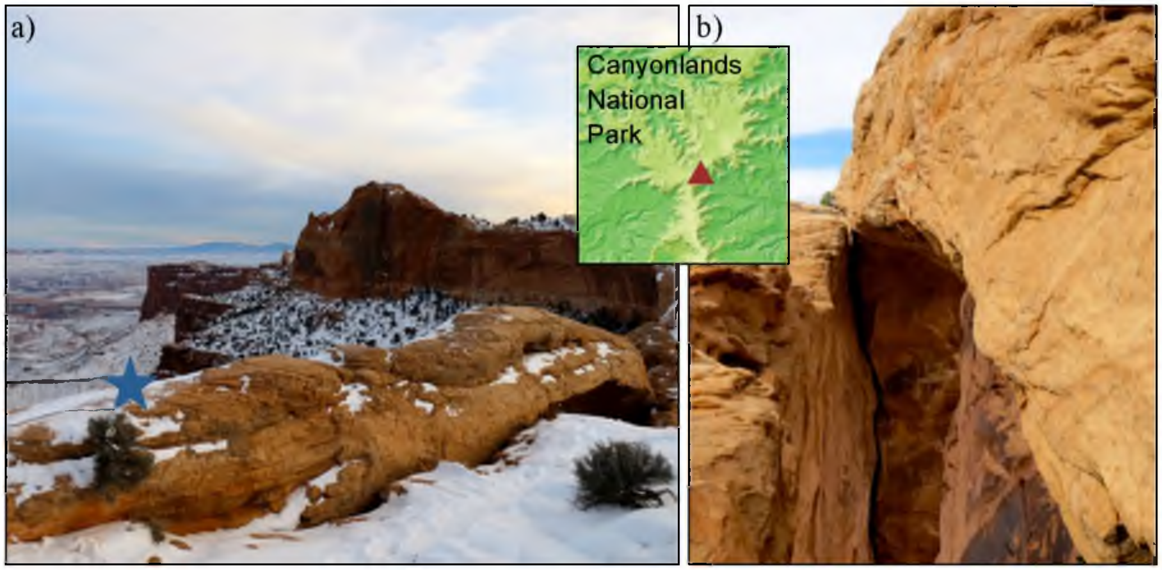

Figure A.23 Mesa Arch in Canyonlands National Park, Utah: a) Active sensor location atop the snow-covered arch indicated by the blue star. b) Side view of the arch showing it peeling away from the cliff.

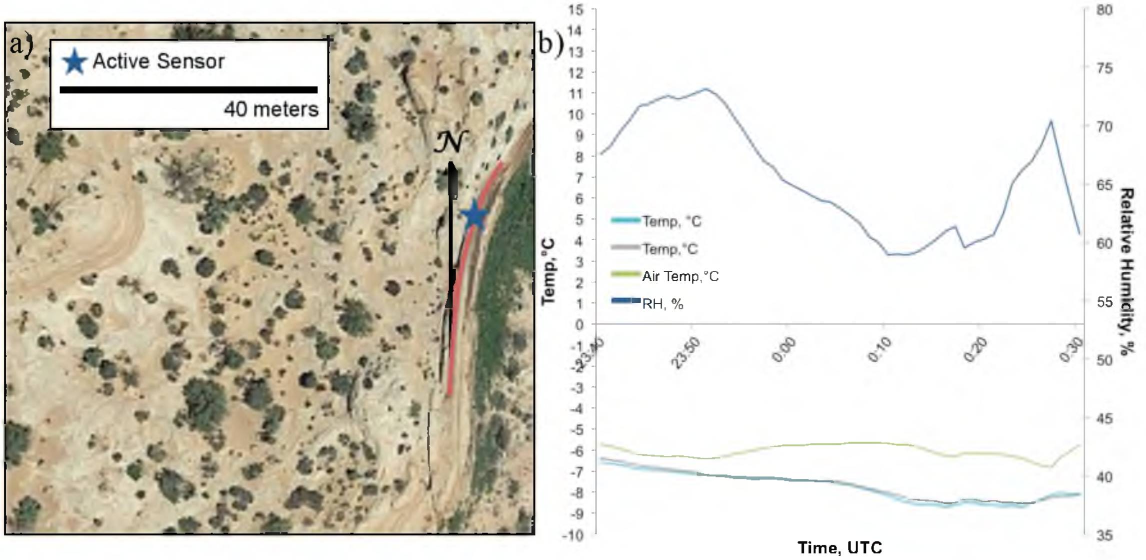

Figure A.24 Further analysis of Mesa Arch: a) Aerial view of Mesa Arch with the location of the active sensor. The arch is north trending, but bends slightly to the east. b) Plot of the rock temperature, air temperature, and relative humidity for the entire test.

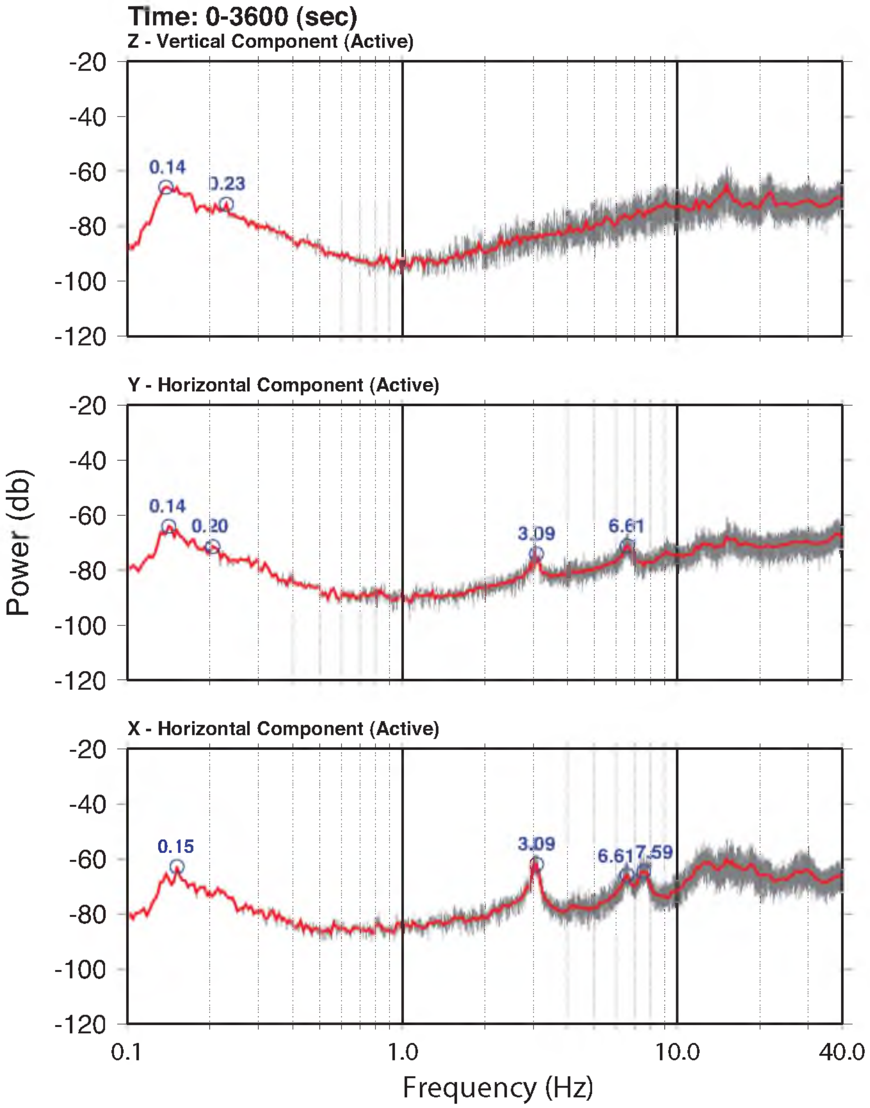

Figure A.25 Absolute power spectra for 1 h of 3-component ambient vibration data. Z is vertical vibration, Y is north-south horizontal, X is east-west horizontal. Gray traces show raw data, red are averaged.

Table A.7: Measured spectral peaks with predominant polarization orientation noted.

Measured Frequency (Hz)	**Degree of Polarization**	**Dominant Azimuth*** (°)	**Incidence Angle**** (°)
3.1	0.9	104	89
6.6	0.9	118	84
7.6	0.8	086	89

**Azimuth angle measured in degrees clockwise from magnetic North*

***Incidence angle measured from vertical. 0° = vertical motion, 90° = horizontal motion*

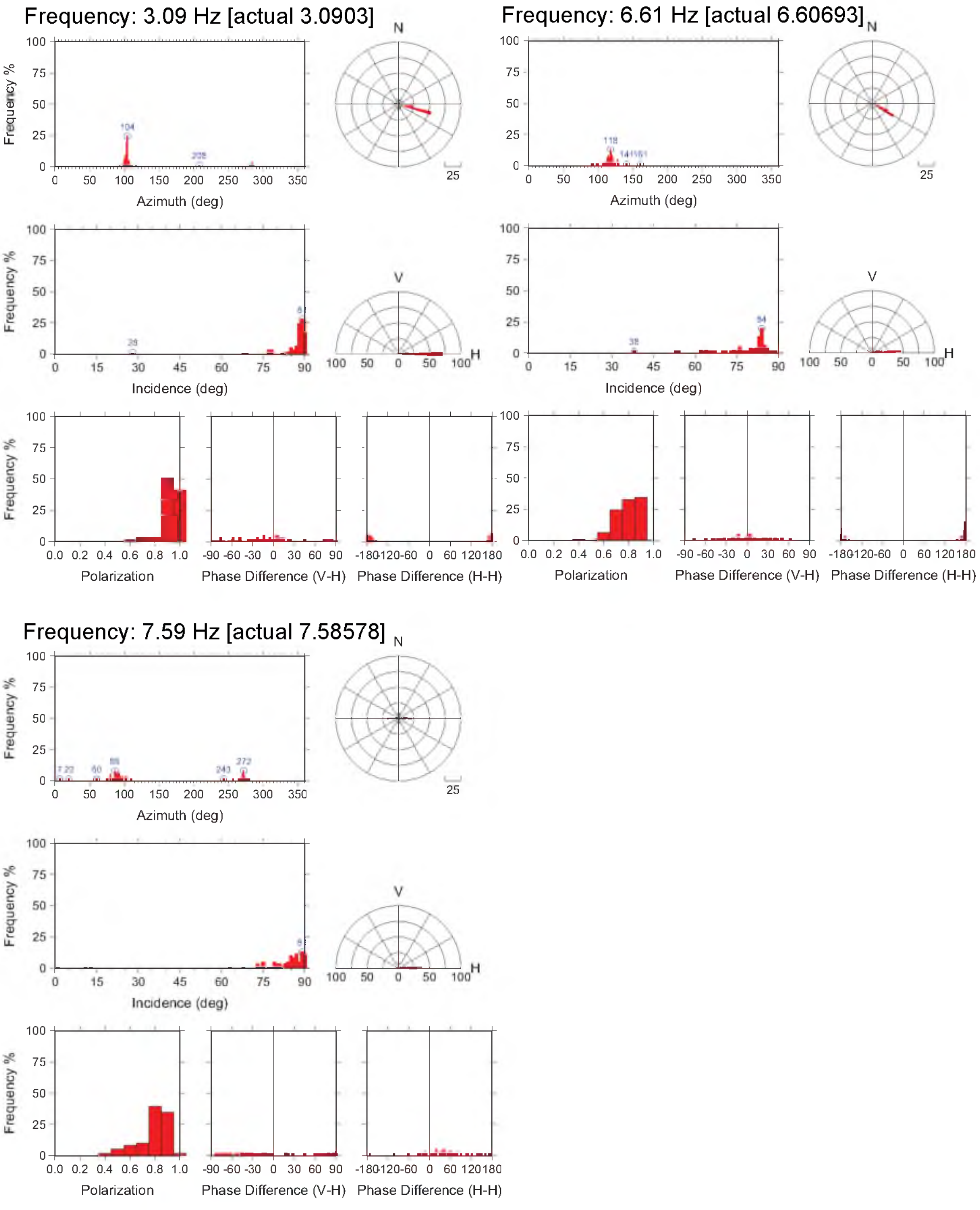

Figure A.26 Polarization plots for each measured frequency at Mesa Arch. Data from the hour-long segment (0 s – 3600 s). The plots display the azimuth, incidence angle, polarization, and phase difference between the vertical and horizontal and the two horizontal components.

February 20, 2014

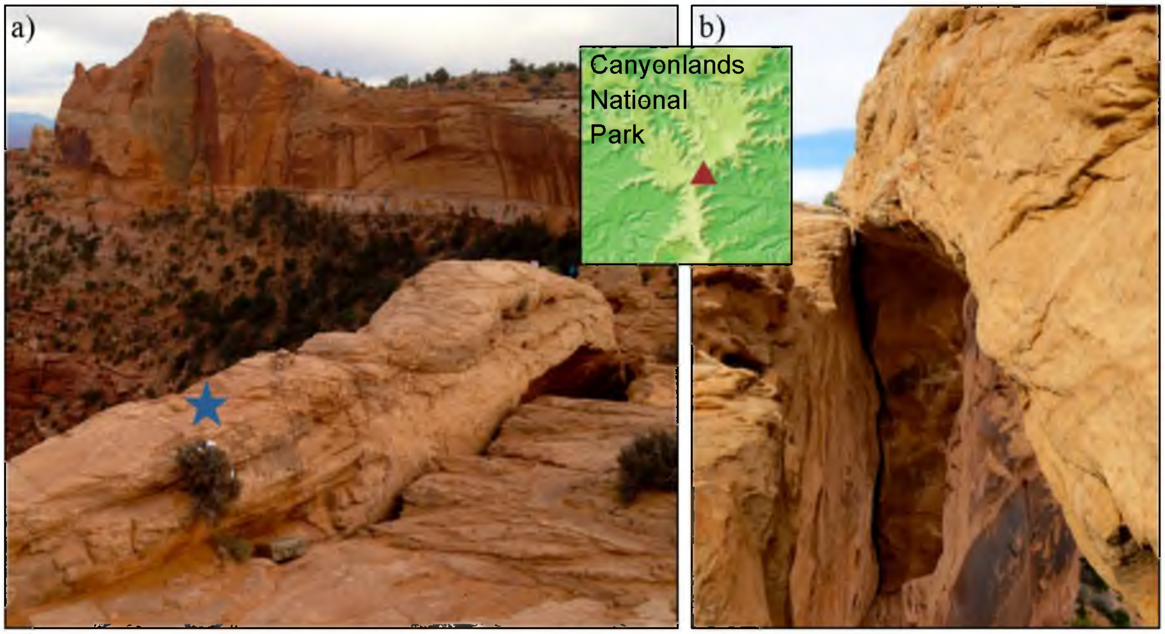

Figure A.27 Mesa Arch in Canyonlands National Park, Utah: a) Location of the active sensor (indicated by blue star) during the February 20, 2014 deployment. b) Side view of the arch showing it peeling away from the cliff.

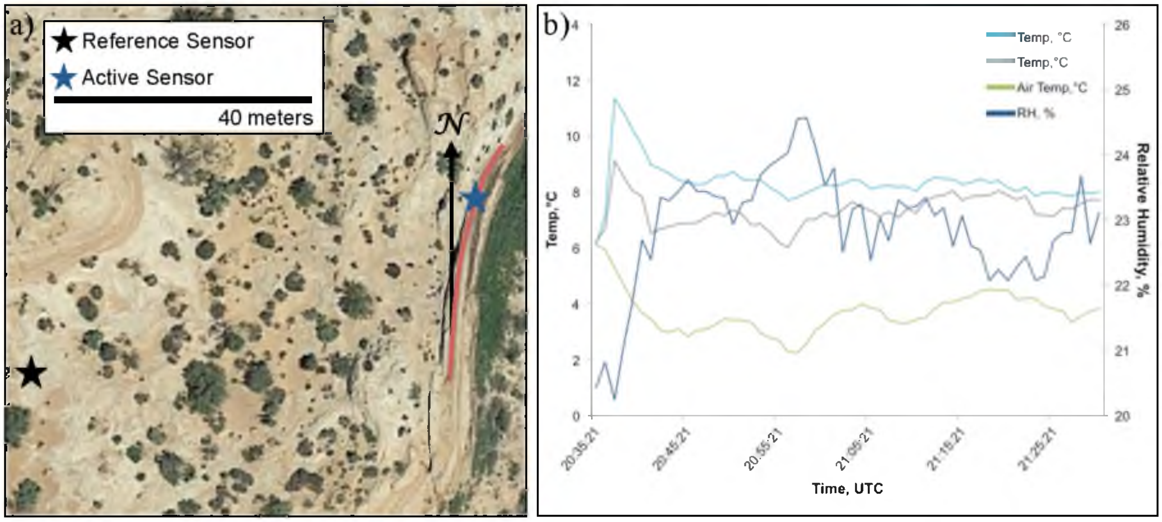

Figure A.28 Further analysis of Mesa Arch: a) Aerial view of Mesa Arch with the location of the active and reference sensors indicated by the stars. The arch is north trending, but bends slightly to the east. b) Plot of the rock temperature, air temperature, and relative humidity for the entire test.

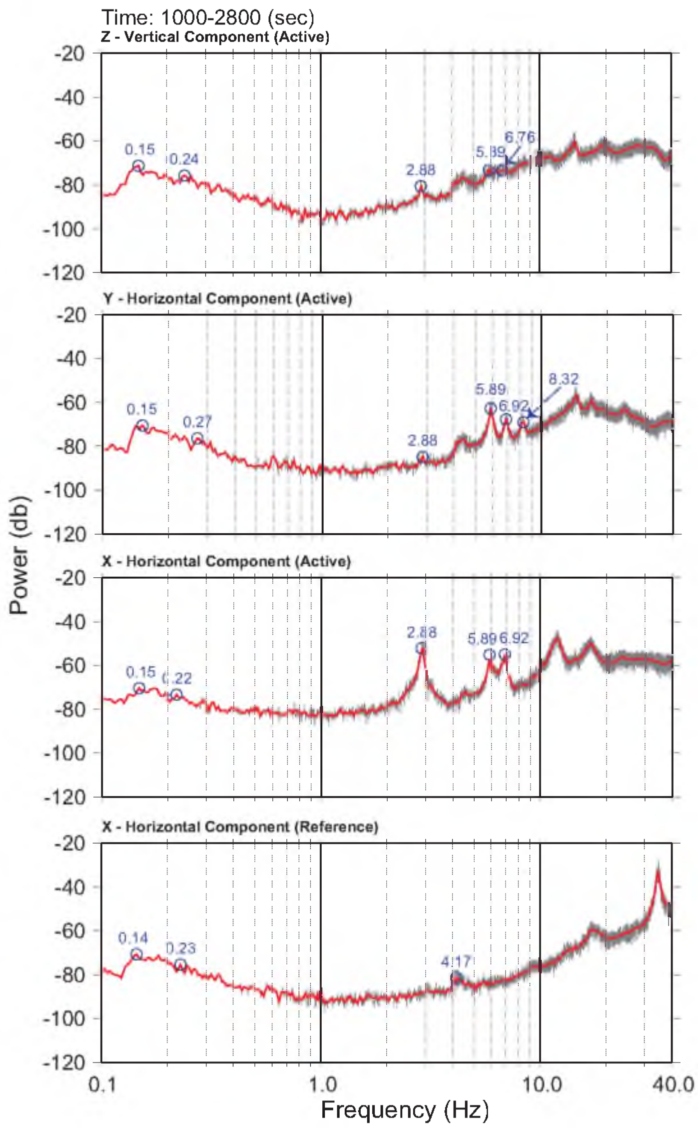

Figure A.29 Absolute power spectra for 30 min of 3-component ambient vibration. Z is vertical vibration, Y is north-south horizontal, X is east-west horizontal. The bottom plot is the east-west component of data from the reference sensor. Gray traces show raw data, red are averaged.

Table A.8: Measured spectral peaks with predominant polarization orientation noted.

Measured Frequency (Hz)	Degree of Polarization	Dominant Azimuth* (°)	Incidence Angle** (°)
2.9	1.0	089	88
5.9	0.9	111	86
6.9	1.0	083	88
8.3	0.4	062	68

**Azimuth angle measured in degrees clockwise from magnetic North*

***Incidence angle measured from vertical. 0° = vertical motion, 90° = horizontal motion*

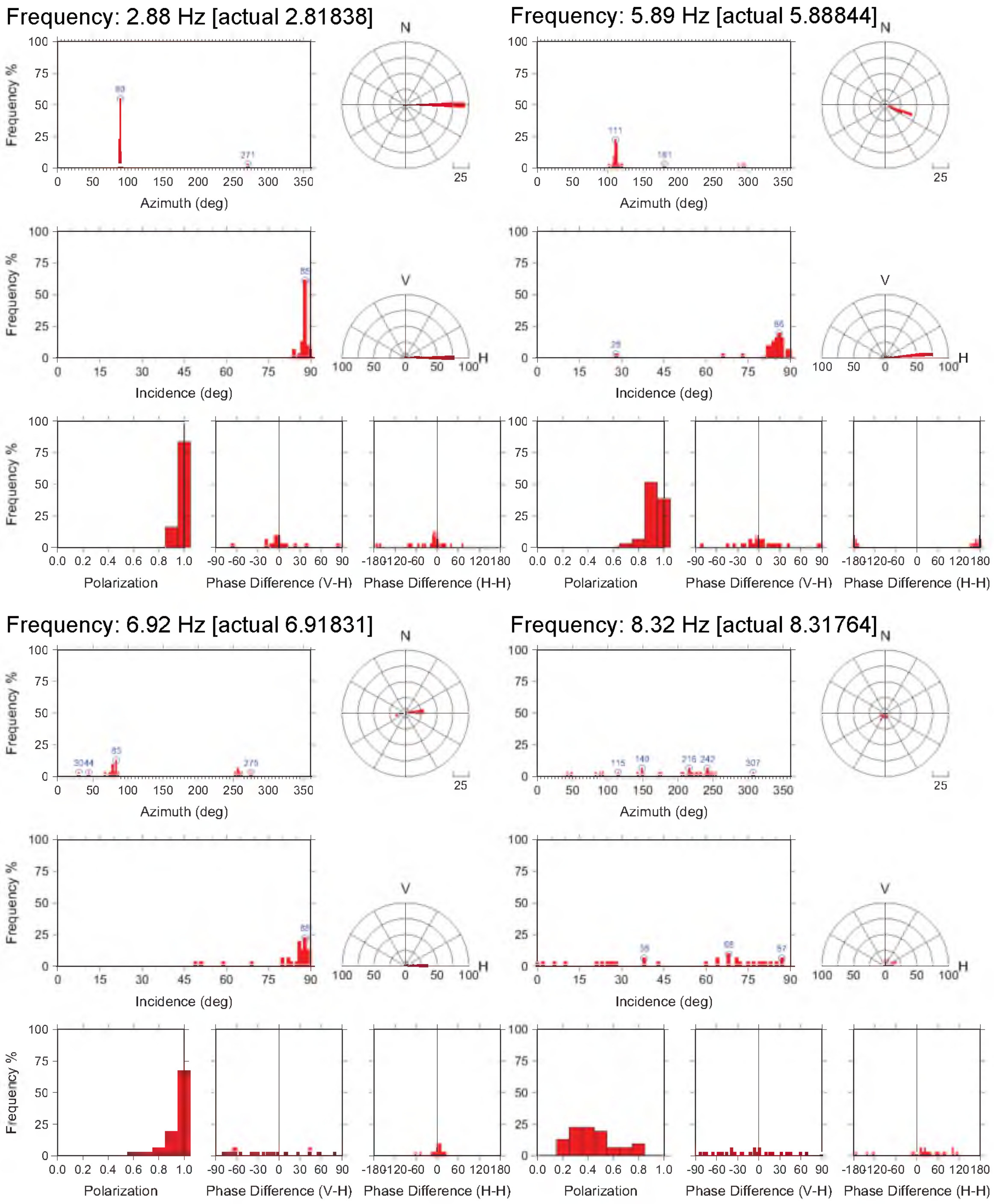

Figure A.30 Polarization plots for each measured frequency at Mesa Arch from the 30-minute segment (1000 s – 2800 s). The plots display the azimuth, incidence angle, polarization, and phase difference between the vertical and horizontal and the two horizontal components.

April 12 – 13, 2014

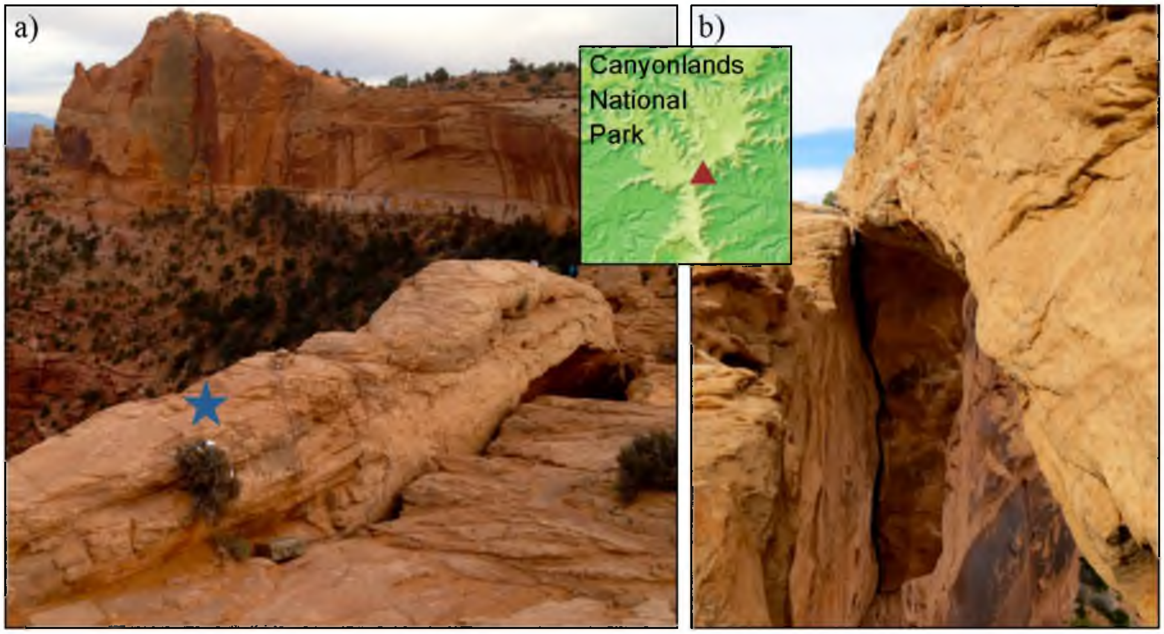

Figure A.31 Mesa Arch in Canyonlands National Park, Utah: a) Location of the sensor (indicated by blue star) during the April 12, 2014 deployment. b) Side view of the arch showing it peeling away from the cliff.

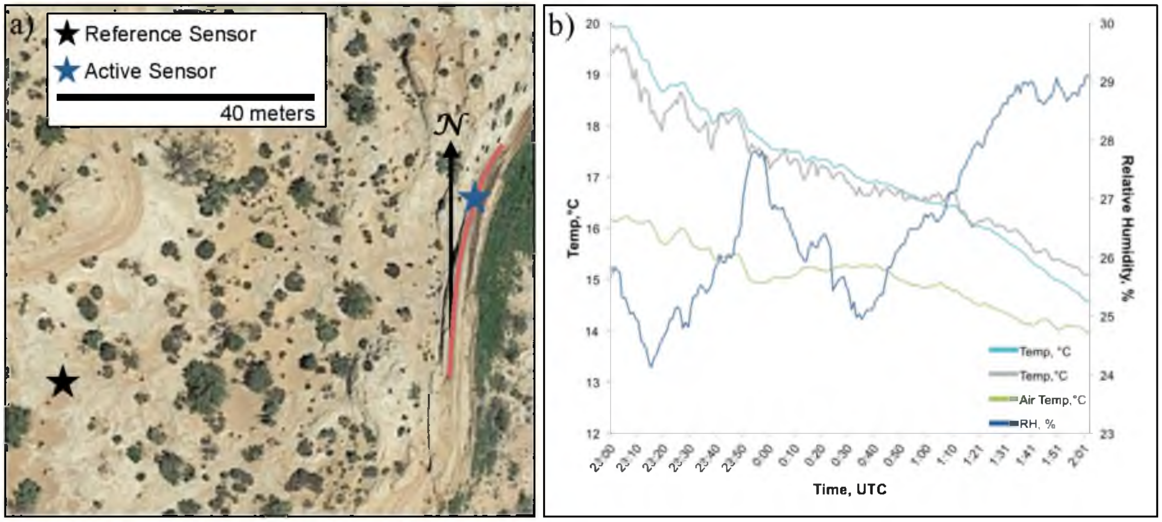

Figure A.32 Further analysis of Mesa Arch: a) Aerial view of Mesa Arch with the location of the active sensor and the reference sensor indicated by the stars. The arch is north trending but bends slightly to the east. b) Plot of the rock temperature, air temperature, and relative humidity for the entire test.

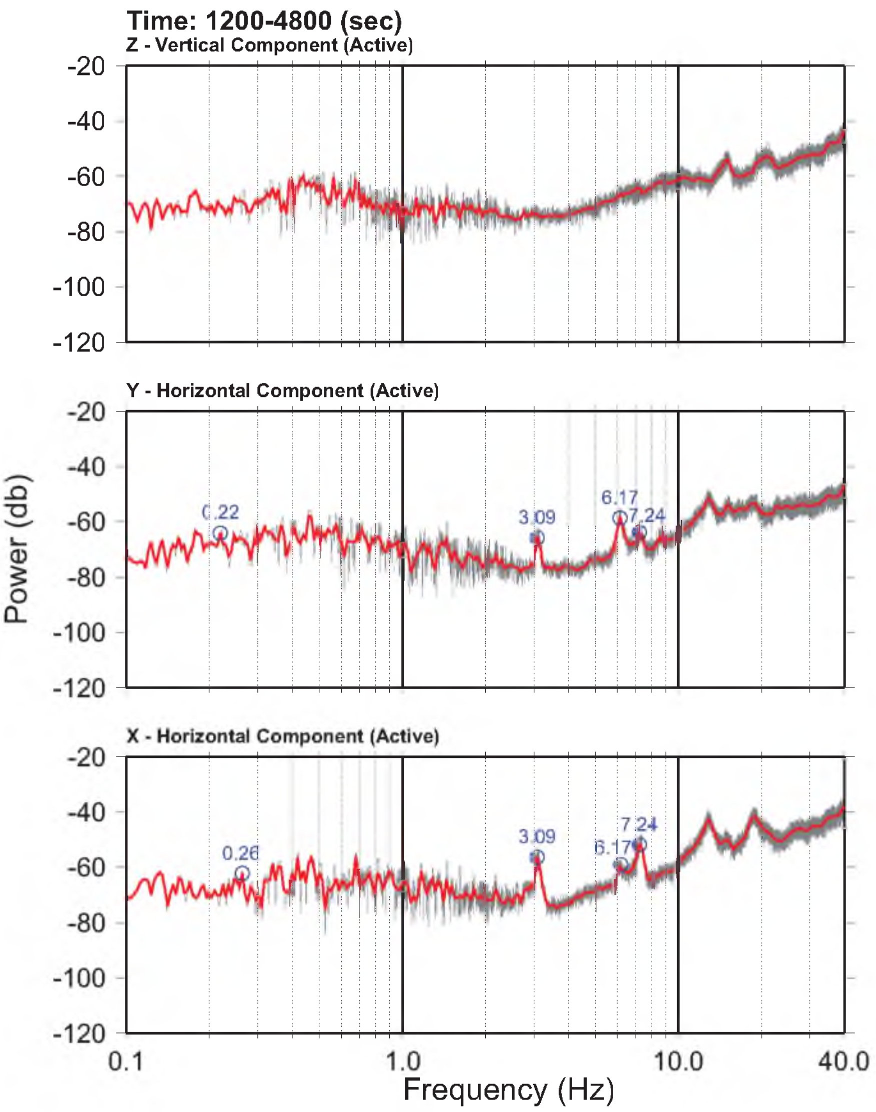

Figure A.33 Absolute power spectra for 1 h of 3-component ambient vibration. Z is vertical vibration, Y is north-south horizontal, X is east-west horizontal. Gray traces show raw data, red are averaged.

Table A.9: Measured spectral peaks with predominant polarization orientation noted.

Measured Frequency (Hz)	Degree of Polarization	Dominant Azimuth* (°)	Incidence Angle** (°)
3.1	0.9	110	89
6.2	0.7	135	80
7.2	0.9	102	80
8.7	0.4	047	68

**Azimuth angle measured in degrees clockwise from magnetic North*

***Incidence angle measured from vertical. 0° = vertical motion, 90° = horizontal motion*

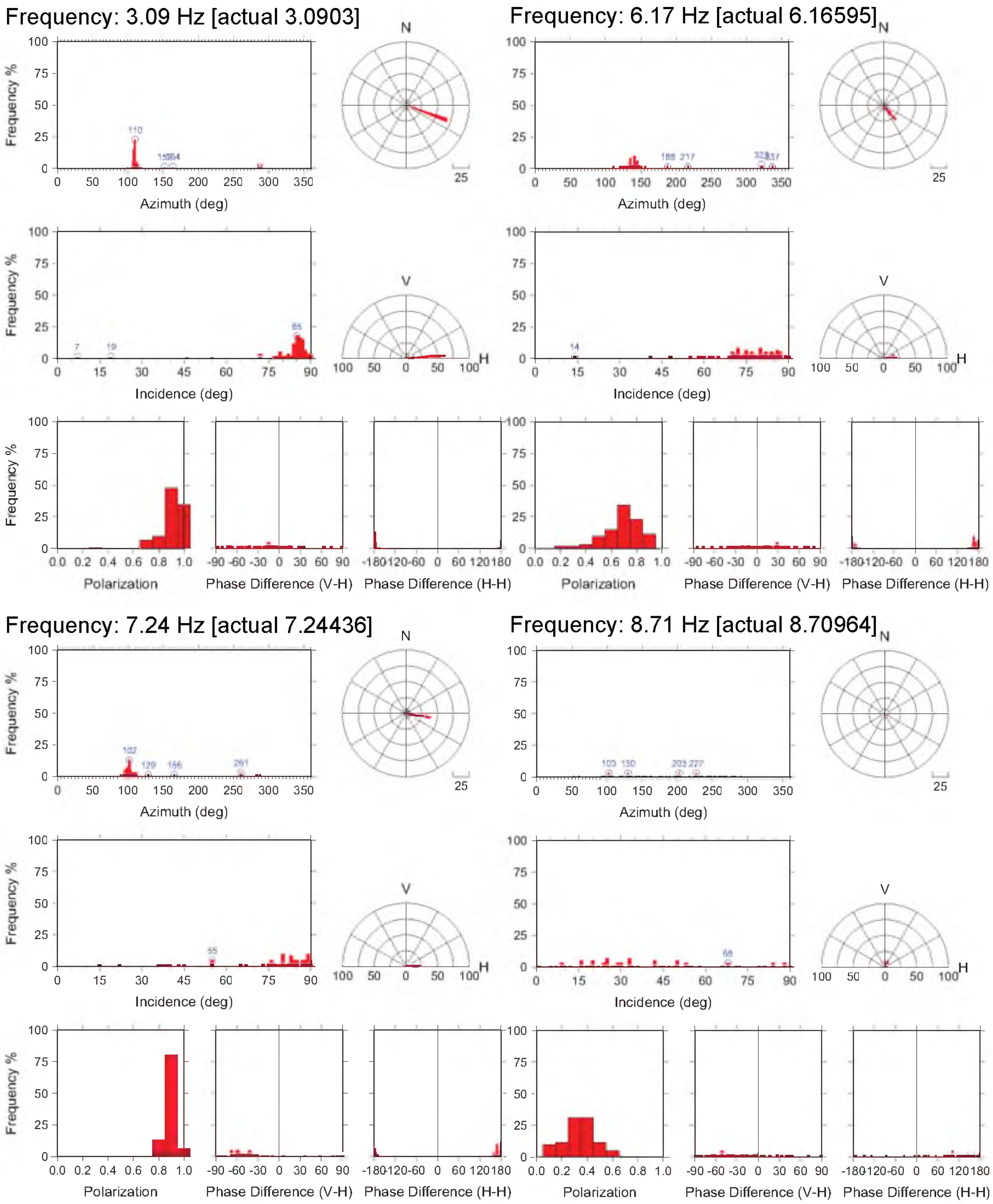

Figure A.34 Polarization plots for each measured frequency at Mesa Arch from the hour-long segment (1200 s – 4800 s). The plots display the azimuth, incidence angle, polarization, and phase difference between the vertical and horizontal and the two horizontal components.

May 5-8, 2014

Figure A.35 Mesa Arch in Canyonlands National Park, Utah: a) Location of the active sensor (indicated by blue star) and tiltmeter (green star) for the 3-day deployment. b) Side view of the arch showing it peeling away from the cliff.

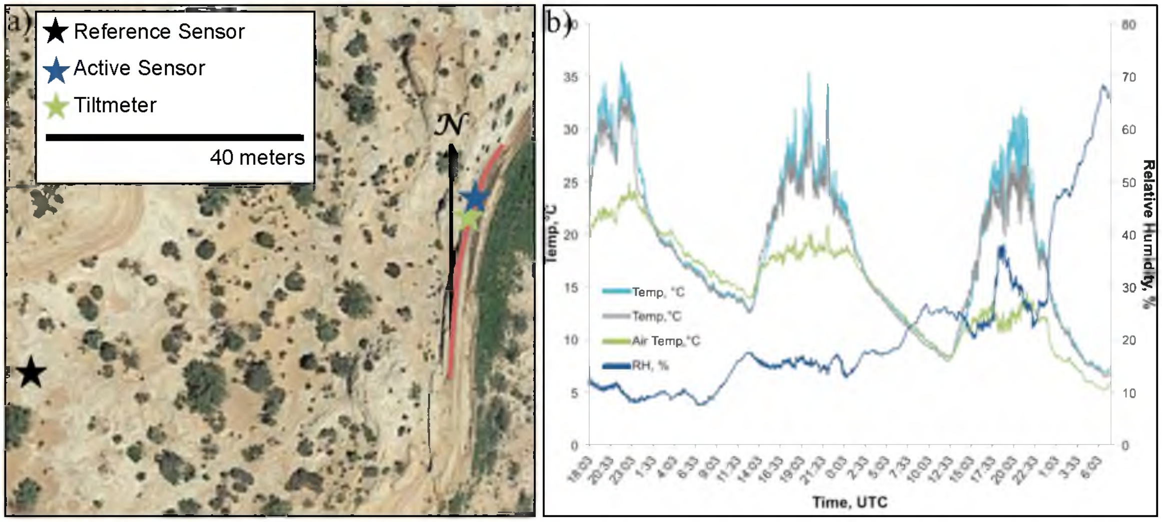

Figure A.36 Further analysis of Mesa Arch: a) Aerial view of Mesa Arch with the location of the active sensor, tiltmeter, and the reference sensor. The arch is north trending, but bends slightly to the east. b) Plot of the rock temperature, air temperature, and relative humidity for the entire test.

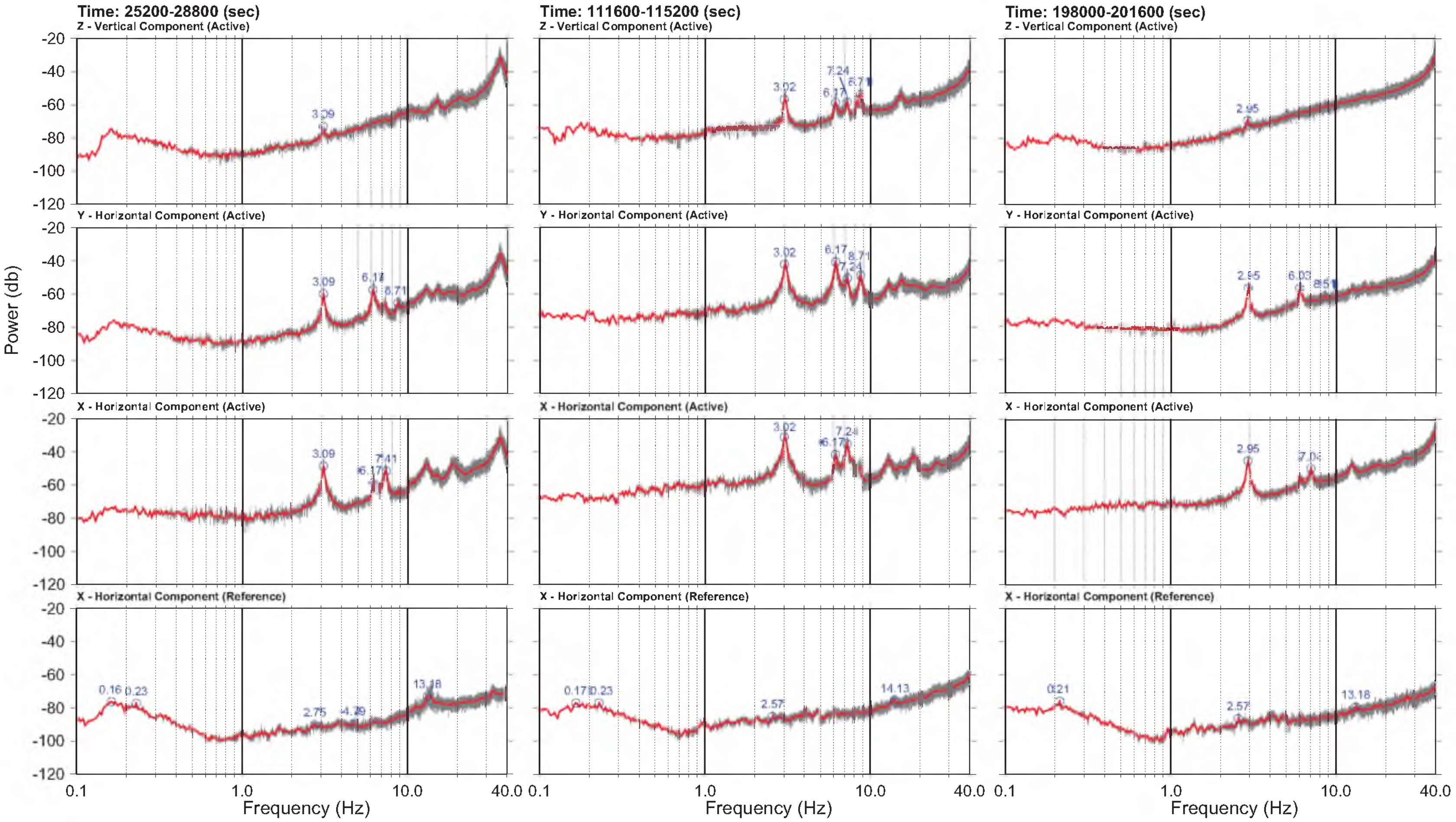

Figure A.37 Hour-long PSD plots from varying times during the 3-day test at Mesa Arch. The top three plots show the 3 components from the active sensor, while the bottom plot shows the east-west horizontal component from the reference sensor.

Table A.10: Measured spectral peaks with predominant polarization orientation noted.

Measured Frequency (Hz)	Degree of Polarization	Dominant Azimuth (°)	Incidence Angle (°)
3.1	1.0	105	87
6.2	1.0	138	85
7.2	1.0	099	86
8.7	0.8	033	65

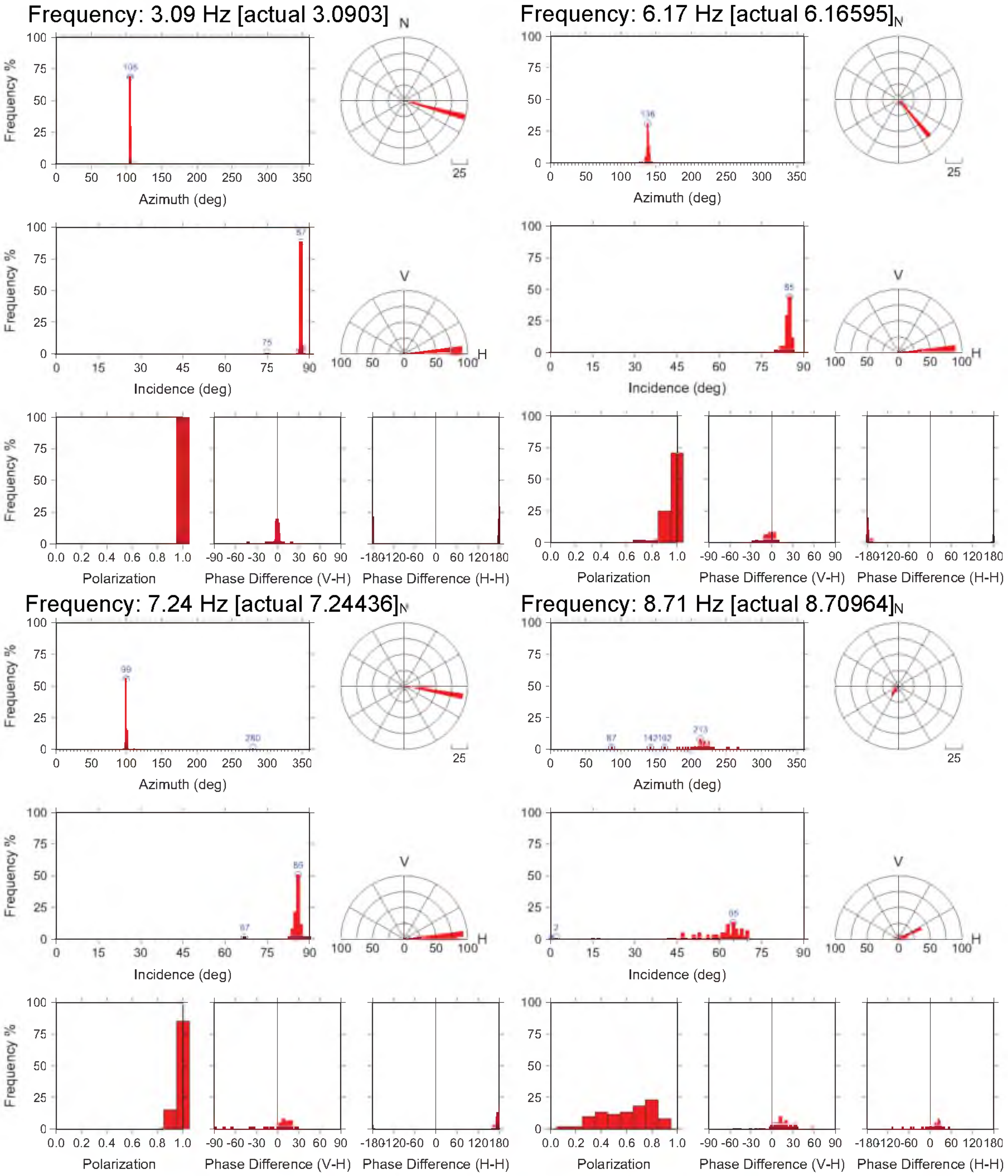

Figure A.38 Polarization plots for each measured frequency at Mesa Arch (100000 s – 103600 s). Analysis is representative of entire 3-day dataset.

June 16, 2014

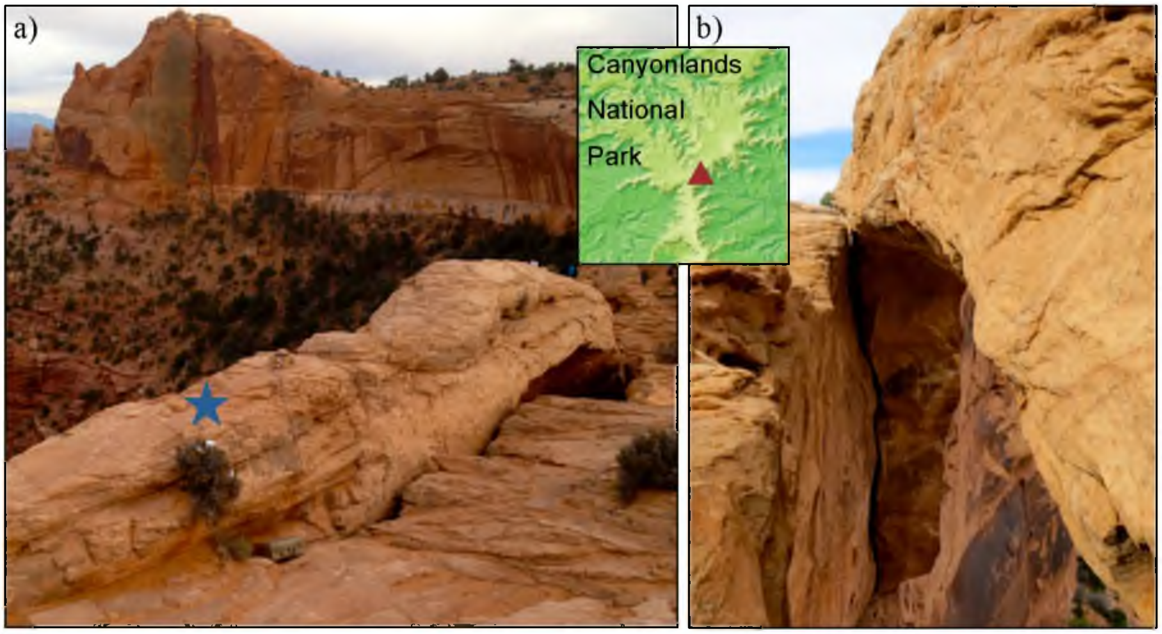

Figure A.39 Mesa Arch in Canyonlands National Park, Utah: a) Location of the active sensor (indicated by blue star) for the deployment. b) Side view of the arch showing it peeling away from the cliff.

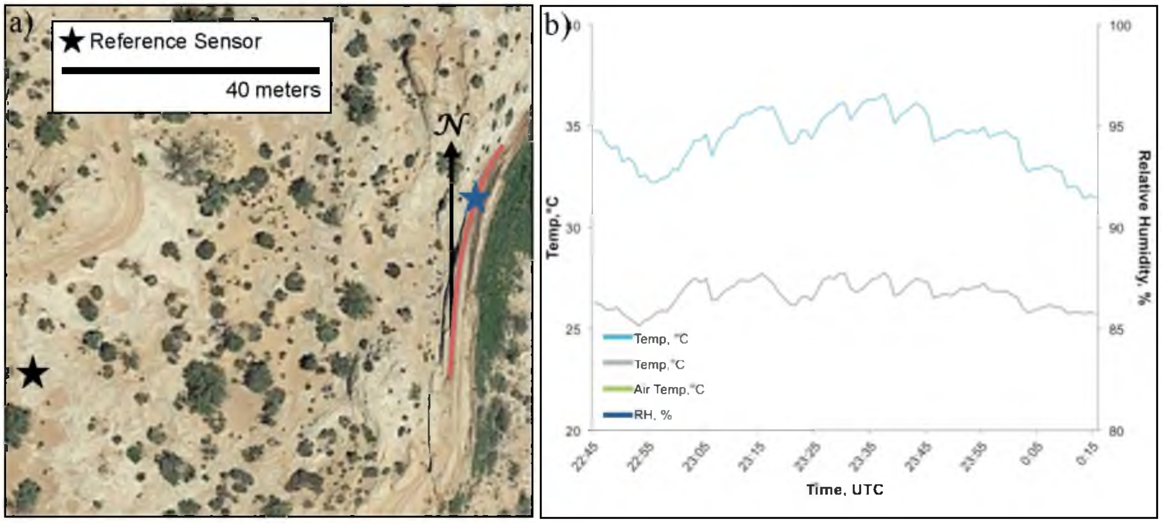

Figure A.40 Further analysis of Mesa Arch: a) Aerial view of Mesa Arch with the location of the active sensor and the stable reference sensor. The arch is north trending, but bends slightly to the east. b) Plot of the rock temperature, air temperature, and relative humidity for the entire test.

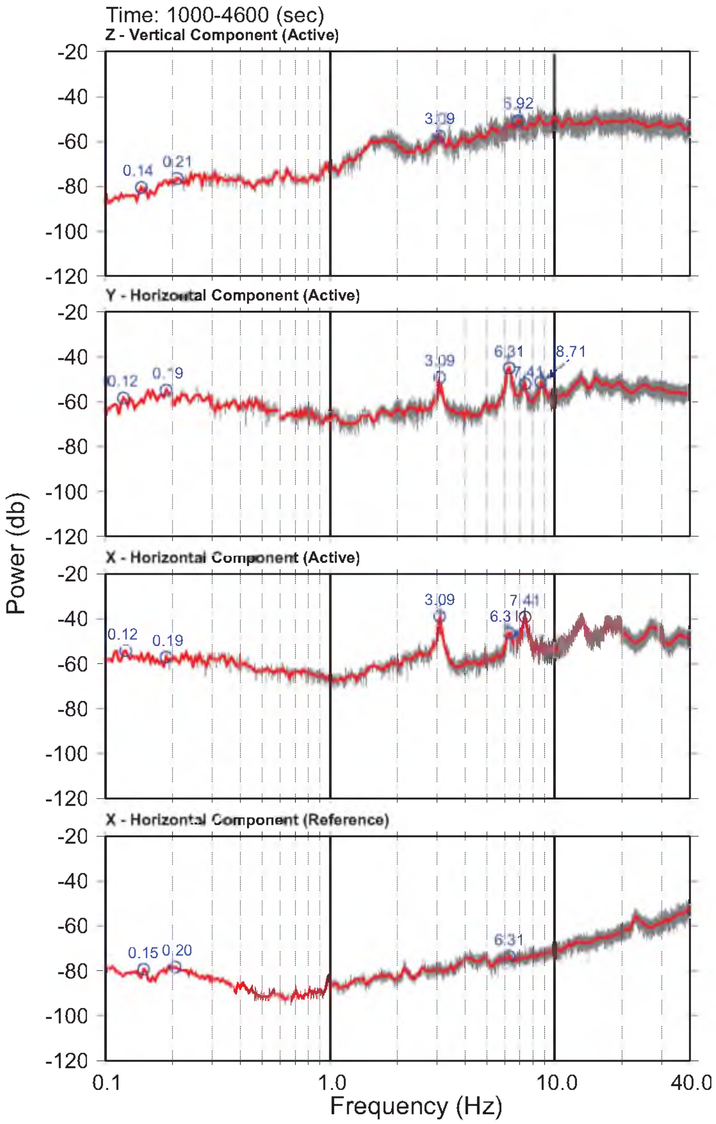

Figure A.41 Absolute power spectra for 1 h of 3-component ambient vibration data. Z is vertical vibration, Y is north-south horizontal, X is east-west horizontal. The bottom plot is east-west component of data from the reference sensor. Gray traces show raw data, red are averaged.

Table A.11: Measured spectral peaks with predominant polarization orientation noted.

Measured Frequency (Hz)	Degree of Polarization	Dominant Azimuth* (°)	Incidence Angle** (°)
3.1	1.0	108	86
6.3	0.7	142	83
7.4	1.0	101	85
8.7	0.5	040	60

**Azimuth angle measured in degrees clockwise from magnetic North*

***Incidence angle measured from vertical. 0° = vertical motion, 90° = horizontal motion*

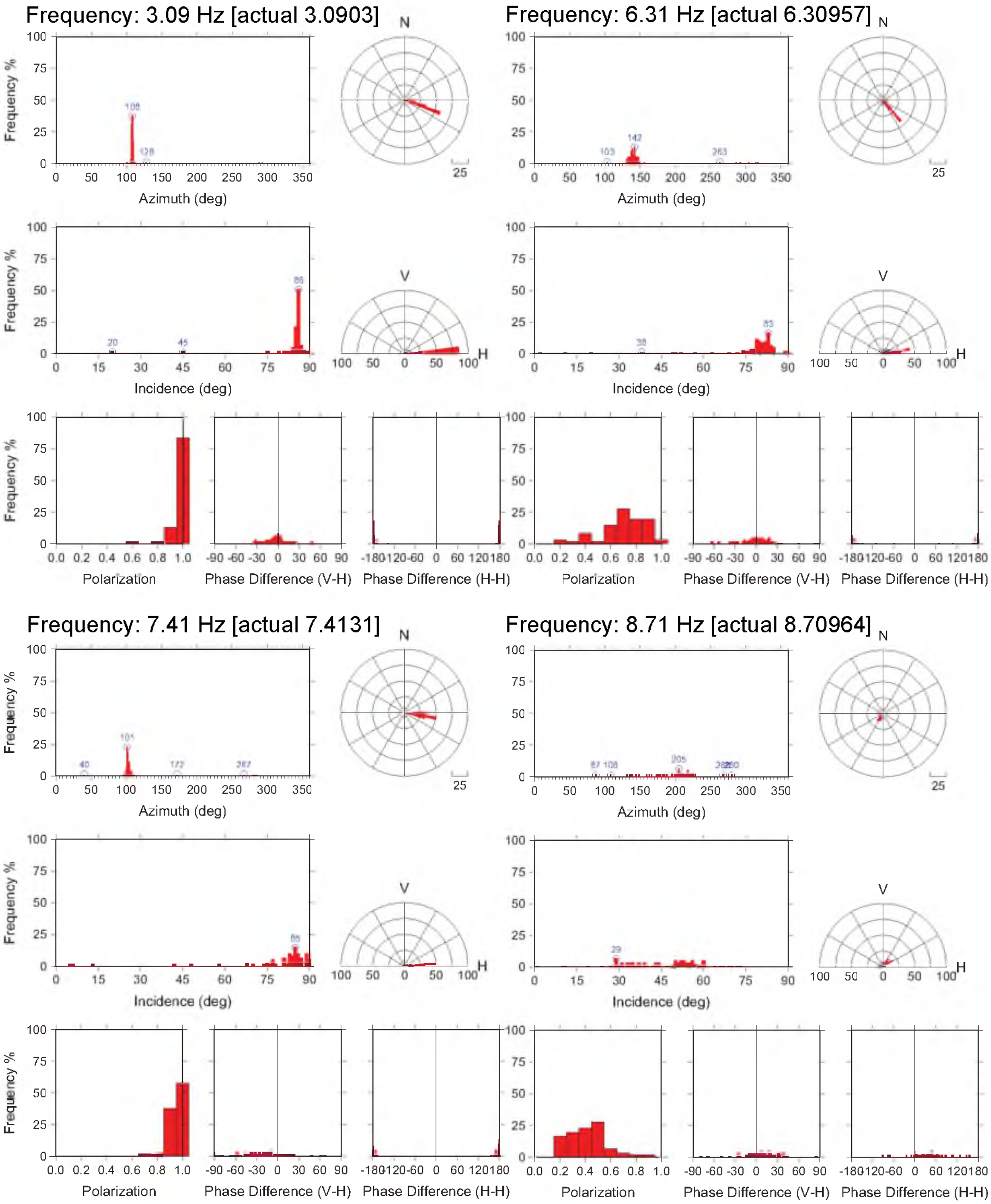

Figure A.42 Polarization plots for each measured frequency at Mesa Arch from the hour-long segment (100000 s – 103600 s). The plots display the azimuth, incidence angle, polarization, and phase difference between the vertical and horizontal and the two horizontal components.

August 20, 2014

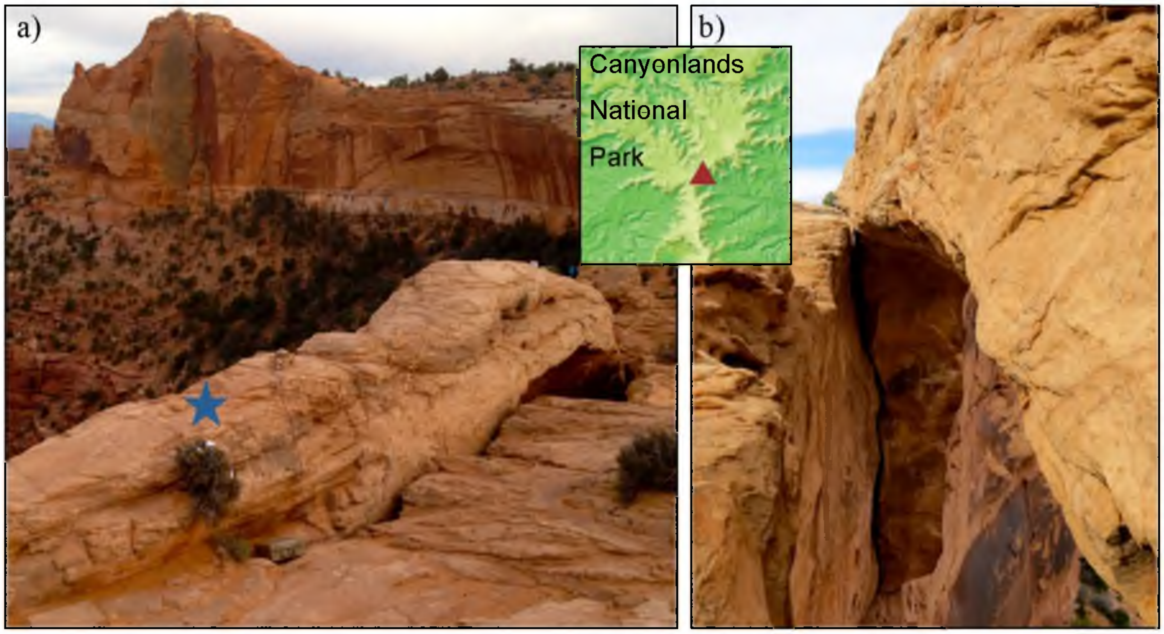

Figure A.43 Mesa Arch in Canyonlands National Park, Utah: a) Location of the active sensor (indicated by blue star). b) Side view of the arch showing it peeling away from the cliff.

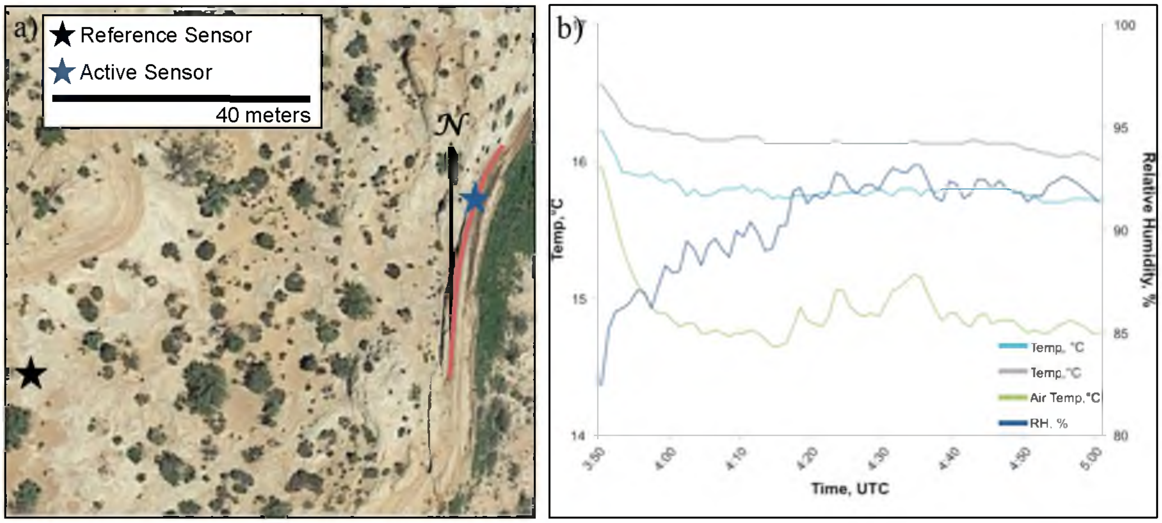

Figure A.44 Further analysis of Mesa Arch: a) Aerial view of Mesa Arch with the location of the active sensor and the reference sensor. The arch is north trending, but bends slightly to the east. b) Plot of the rock temperature, air temperature, and relative humidity for the entire test.

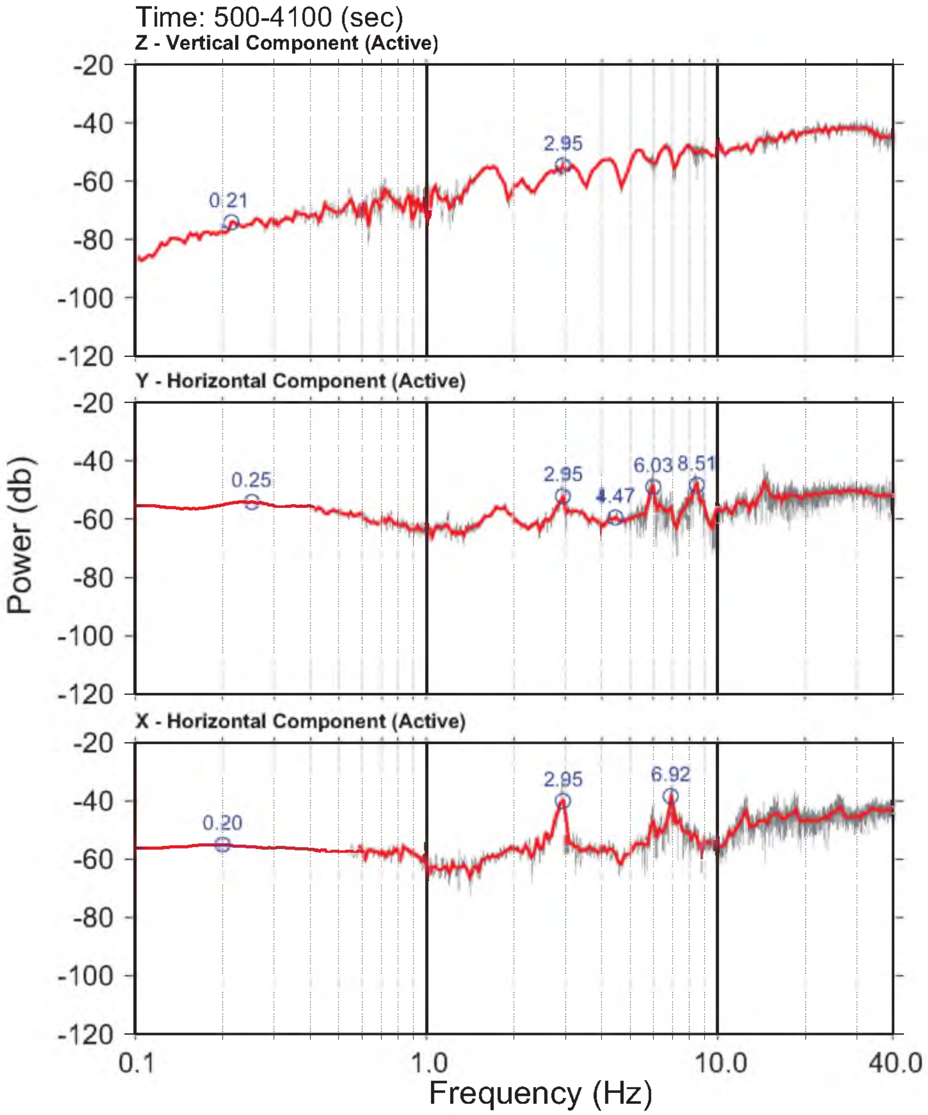

Figure A.45 Absolute power spectra for 1 h of 3-component ambient vibration data. Z is vertical vibration, Y is north-south horizontal, X is east-west horizontal. The bottom plot is east-west component of data from the reference sensor. Gray traces show raw data, red are averaged.

Table A.12: Measured spectral peaks with predominant polarization orientation noted.

Measured Frequency (Hz)	Degree of Polarization	Dominant Azimuth* (°)	Incidence Angle** (°)
3.0	1.0	099	86
6.0	0.8	128	82
6.9	1.0	093	52
8.5	0.3	040	62

**Azimuth angle measured in degrees clockwise from magnetic North*

***Incidence angle measured from vertical. 0° = vertical motion, 90° = horizontal motion*

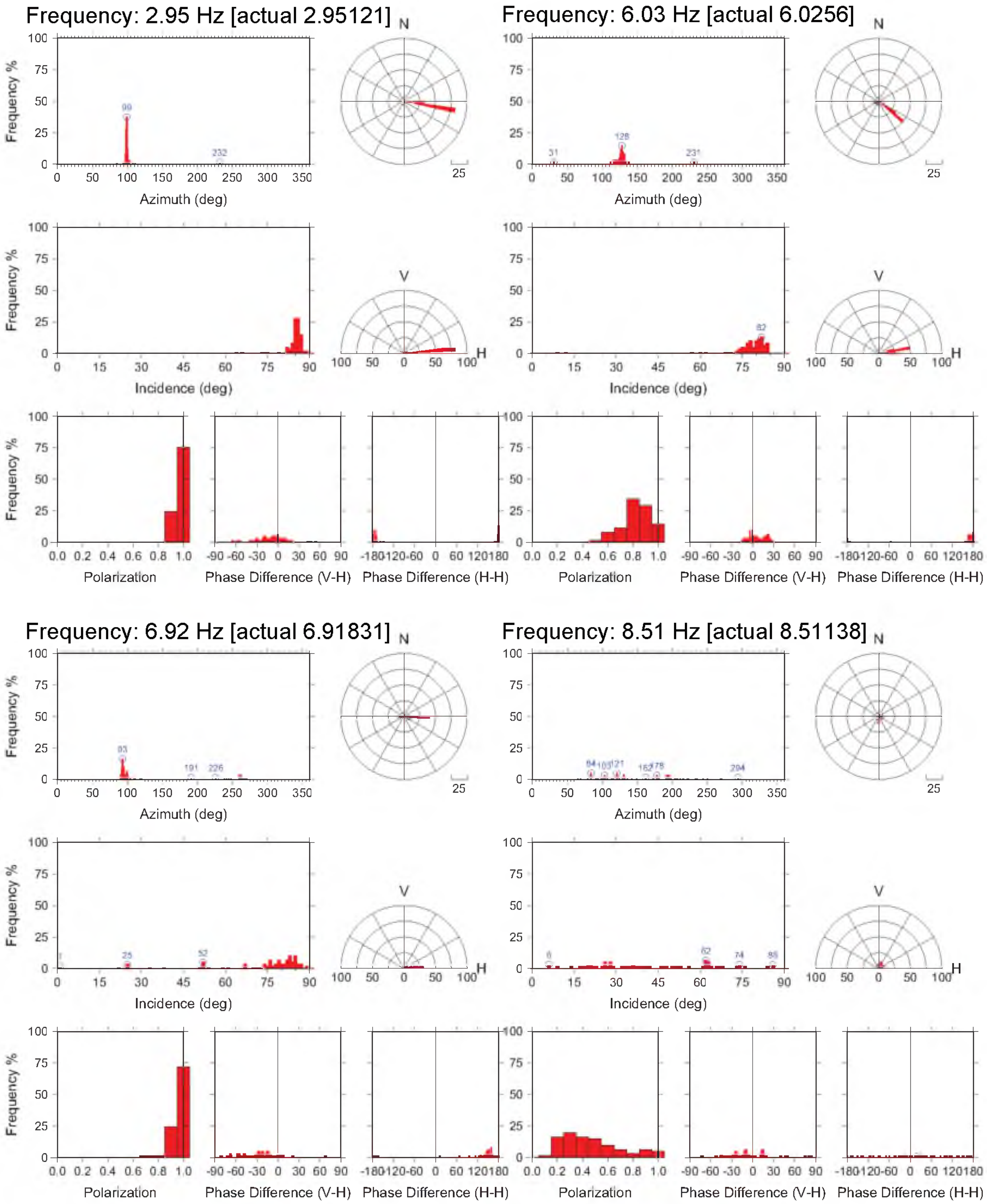

Figure A.46 Polarization plots for each measured frequency at Mesa Arch from the hour-long segment (500 s – 4100 s). The plots display the azimuth, incidence angle, polarization, and phase difference between the vertical and horizontal and the two horizontal components.

October 28, 2014

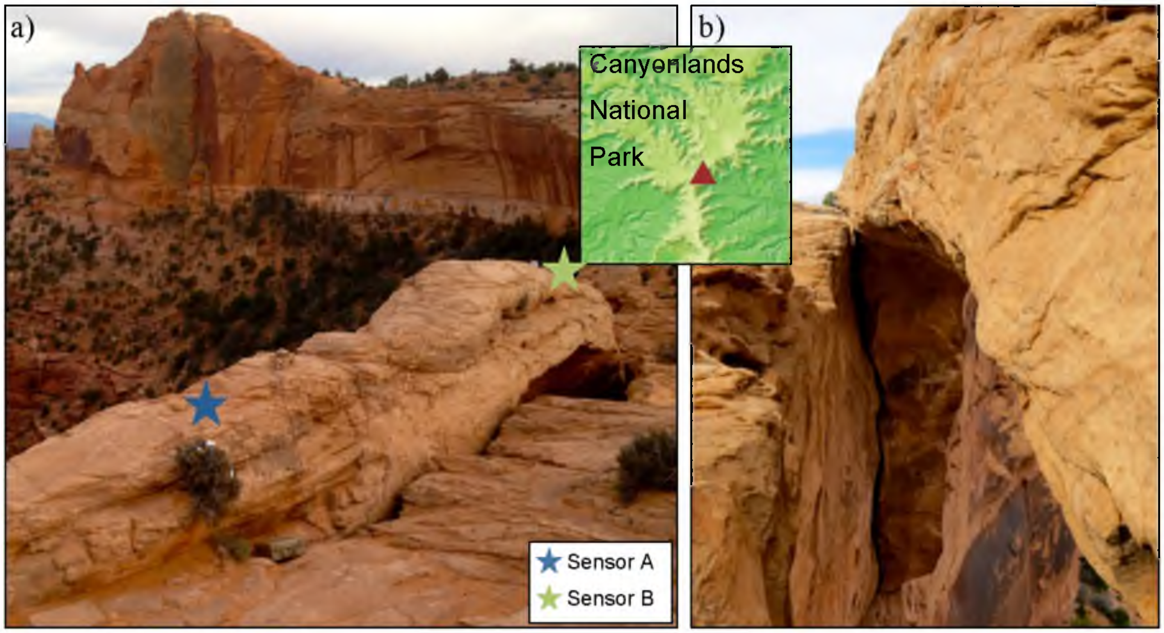

Figure A.47 Mesa Arch in Canyonlands National Park, Utah: a) Location of the two sensors (indicated by stars) during the October 28, 2014 deployment. b) Side view of the arch showing it peeling away from the cliff.

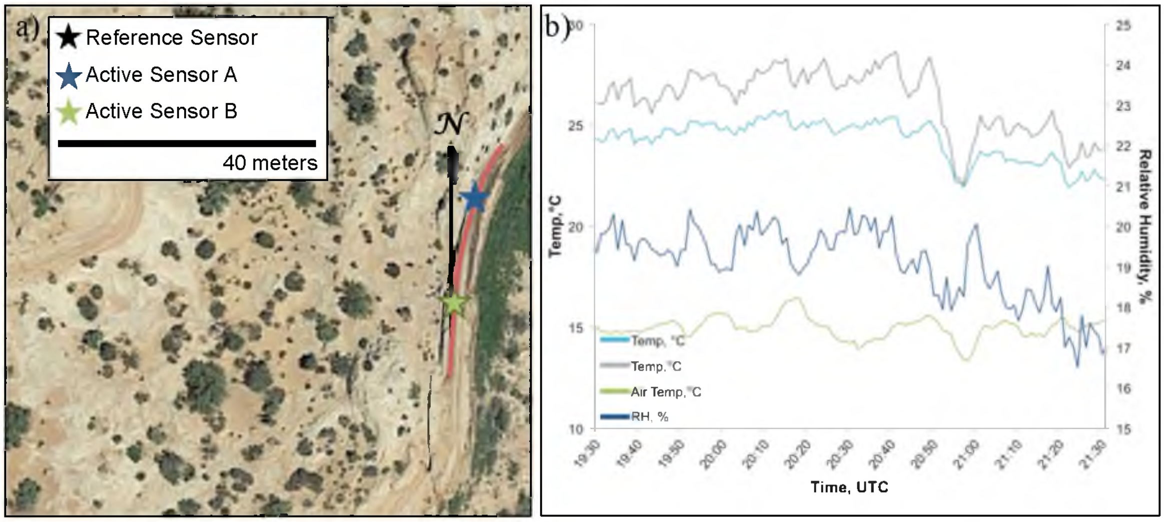

Figure A.48 Further analysis of Mesa Arch: a) Aerial view of Mesa Arch with the location of the sensors. The arch is north trending, but bends slightly to the east. b) Plot of the rock temperature, air temperature, and relative humidity for the entire test.

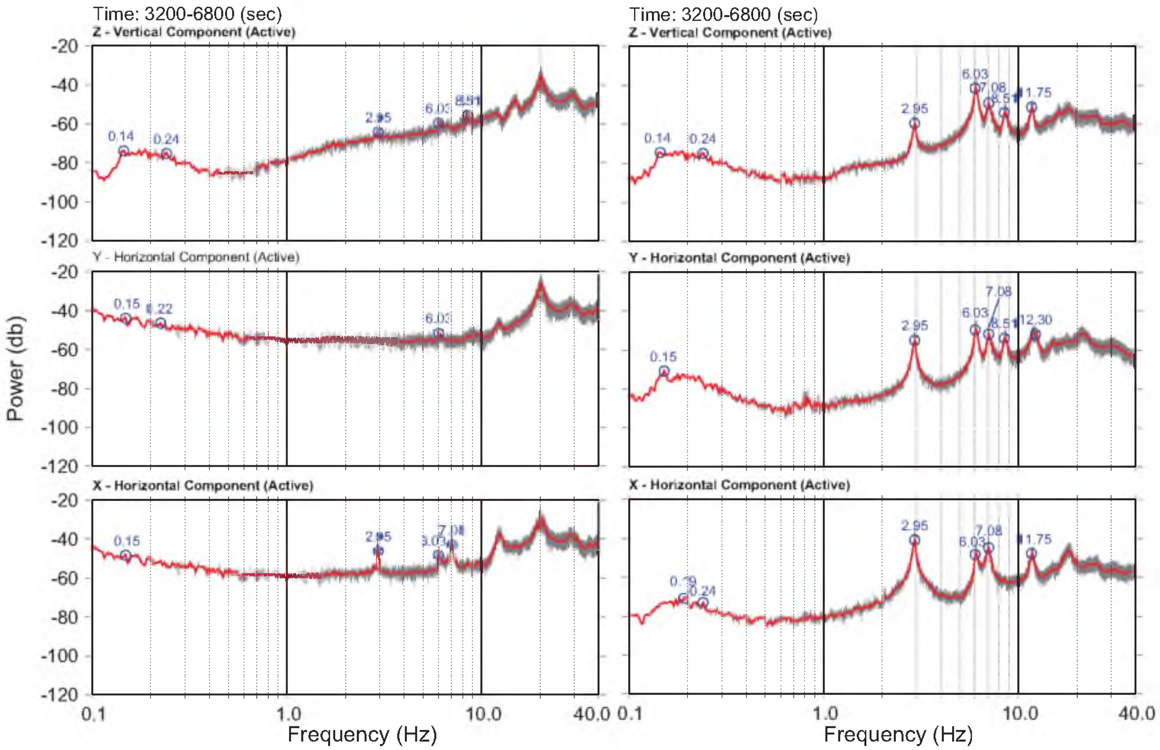

Figure A.49 Absolute power spectra for 1 h of 3-component ambient vibration data for the two sensors. Z is vertical vibration, Y is north-south horizontal, X is east-west horizontal. The bottom plot is east-west component of data from the reference sensor. Gray traces show raw data, red are averaged.

Table A.13: Measured spectral peaks with predominant polarization orientation noted.

Measured Frequency (Hz)	**Degree of Polarization**	**Dominant Azimuth*** (°)	**Incidence Angle**** (°)
3.0	1.0	102	83
6.0	1.0	049	31
7.1	0.9	115	61
8.5	0.9	166	45

**Azimuth angle measured in degrees clockwise from magnetic North*

***Incidence angle measured from vertical. 0° = vertical motion, 90° = horizontal motion*

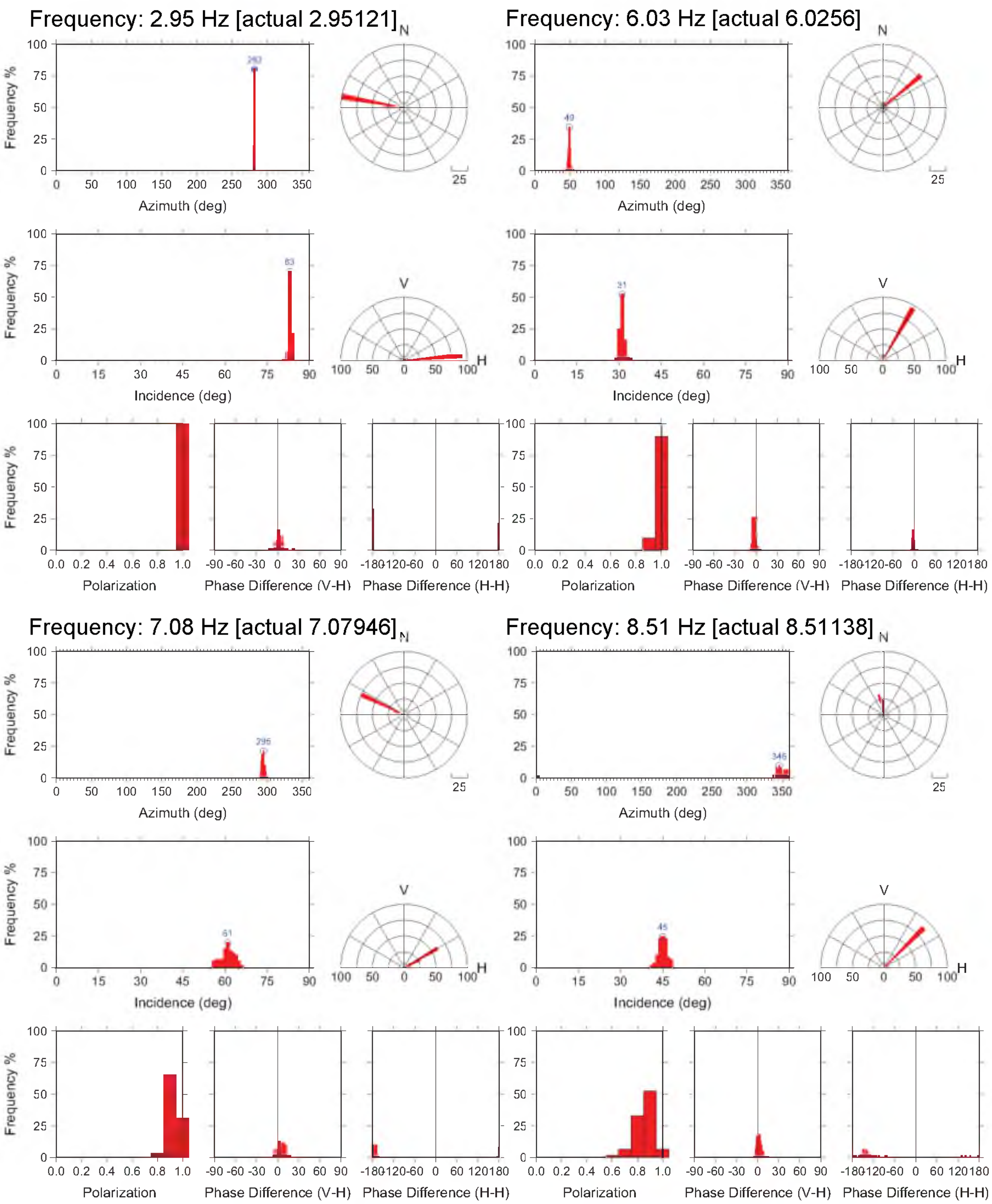

Figure A.50 Polarization plots for each measured frequency at Mesa Arch from the hour-long segment (3200 s – 6800 s). The plots display the azimuth, incidence angle, polarization, and phase difference between the vertical and horizontal and the two horizontal components.

A.5 Balanced Rock

A.5.1 Site Description

Balanced Rock is located in Arches National Park. Weathered in place, a large block of Slick Rock sandstone balances on top of a heavily cracked layer of the Dewey Bridge Member of the Carmel Formation that rests above Navajo sandstone (Graham, 2004). The massive balancing rock possesses a different appearance of precariousness from every angle, making it difficult to predict the direction of failure in the event of a collapse (Figure A.51a,b).

A.5.2 Measurement Overview

A single test was conducted at Balanced Rock on September 29, 2013 for a duration of over 5 h. Data were collected using the site-to-reference configuration: one active sensor and one reference sensor (Figure A.52a). Temperature and relative humidity were also collected for the duration of the test (Figure A.52b). Unfortunately, the top of Balanced Rock is inaccessible, so various locations along the base were tested.

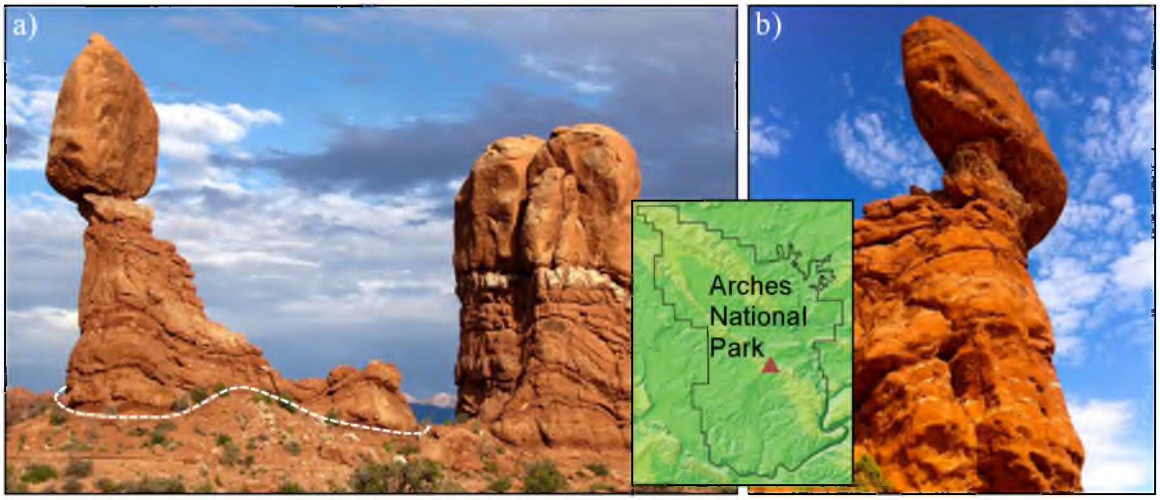

Figure A.51 Balanced Rock in Arches National Park, Utah: a) Side view with the sensor located along the base of the feature indicated by the white line. b) View of the balancing rock from beneath.

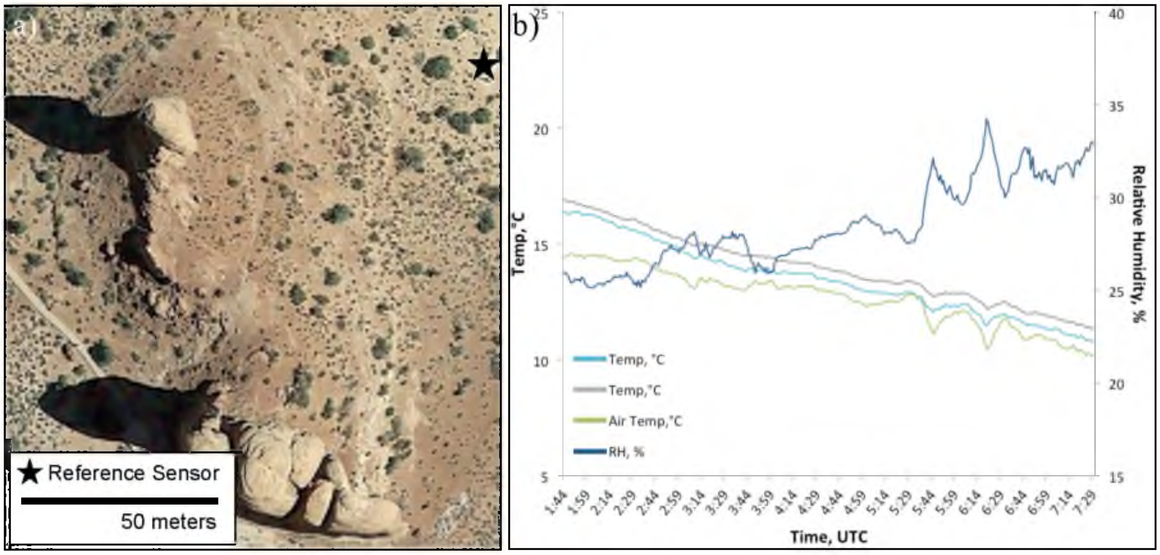

Figure A.52 Further analysis of Balanced Rock: a) Aerial view of Balanced Rock. b) Plot of the rock temperature, air temperature, and relative humidity for the entire test.

A.5.3 Ambient Vibration Spectra

Figure A.53 shows 3-component power spectra from the active sensor for 1 h. Results reveal a lack of pronounced spectral peaks in even the clearest ambient vibration data, rendering further analysis unnecessary.

A.5.4 Interpretation and Discussion

The lack of useful data generated at Balanced Rock is unfortunate, but it still provides valuable information in showing that it is difficult to obtain clear spectral peaks without placing the sensor directly on top of the structure. In future work, we hope to place the sensor at higher positions on the feature to obtain improved data.

A.6 Delicate Arch

A.6.1 Site Description

Delicate Arch is arguably the premier landmark of Arches National Park and an icon of the southwestern U.S., and is so-named owing to its fragile appearance; the full-

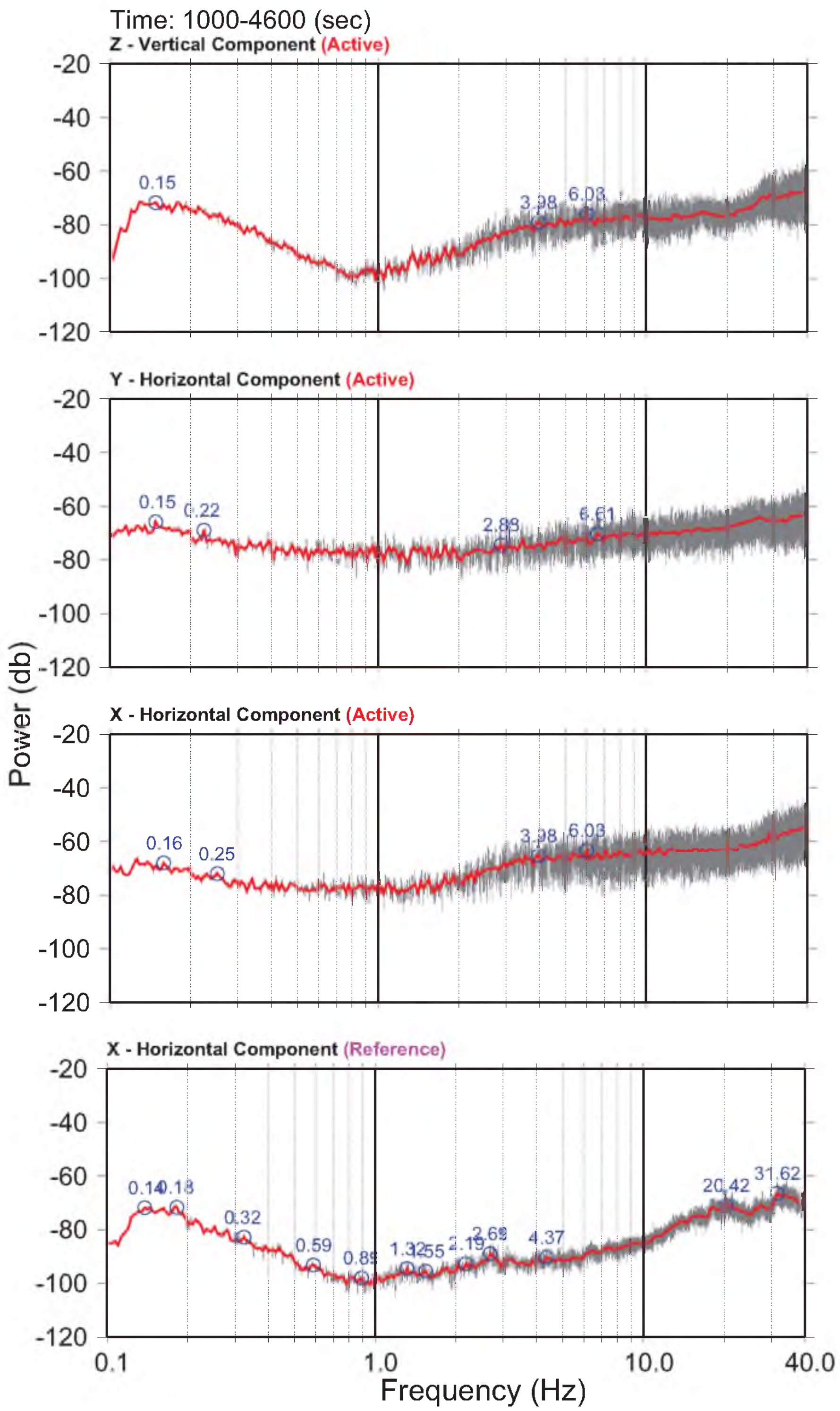

Figure A.53 Absolute power spectra for 1 h of 3-component ambient vibration data. Z is vertical vibration, Y is north-south horizontal, X is east-west horizontal. The bottom plot is east-west component of data from the reference sensor. Gray traces show raw data, red are averaged.

arc span rests atop a thin, sloping discontinuity and has a slender eastern support with a fractured rock cap. It is an east-west facing free-standing arch perched along the southern rim of a natural rock bowl. The basal discontinuity exhibits significant weathering.

A.6.2 Measurement Overview

Two tests were conducted at Delicate Arch, the first on October 25, 2013 and the second on February 20, 2014 during a windy night. Data were collected using the site-to-reference configuration: one active sensor placed in the same position for both tests and one reference sensor located in a stable position ~100 m from the arch (Figure A.54c). Unfortunately, the top of Delicate Arch is inaccessible so the active sensor was placed at the base of the arch. Temperature and relative humidity were also collected for the duration of the test (Figure A.55a,b).

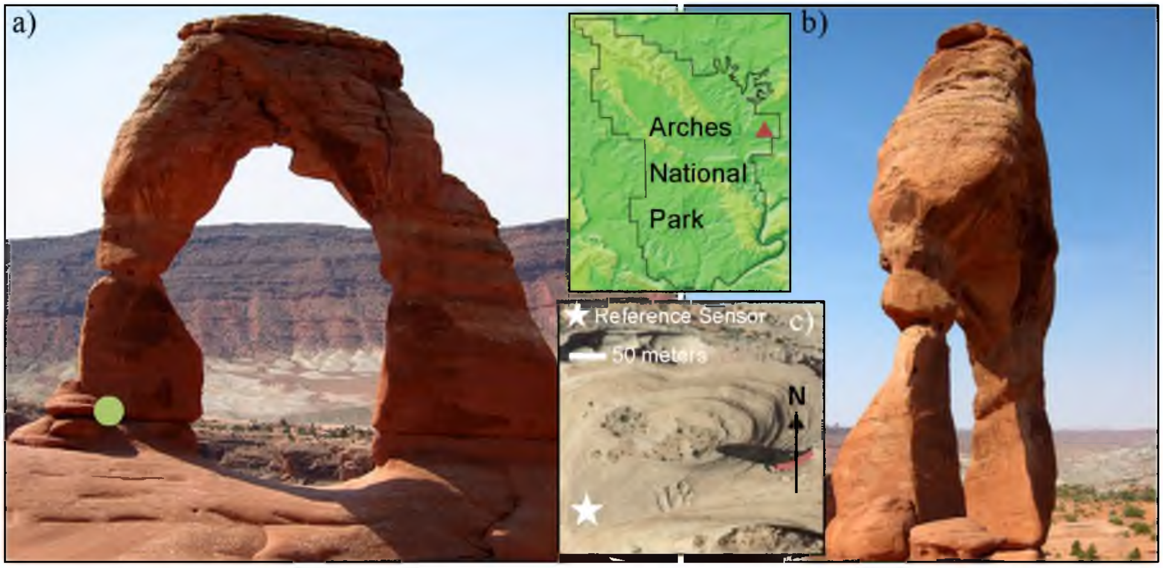

Figure A.54 Delicate Arch in Arches National Park, Utah: a) The arch with the sensor location denoted by the green dot. b) Side view of the arch c) Aerial view of the arch showing that it is east-west trending.

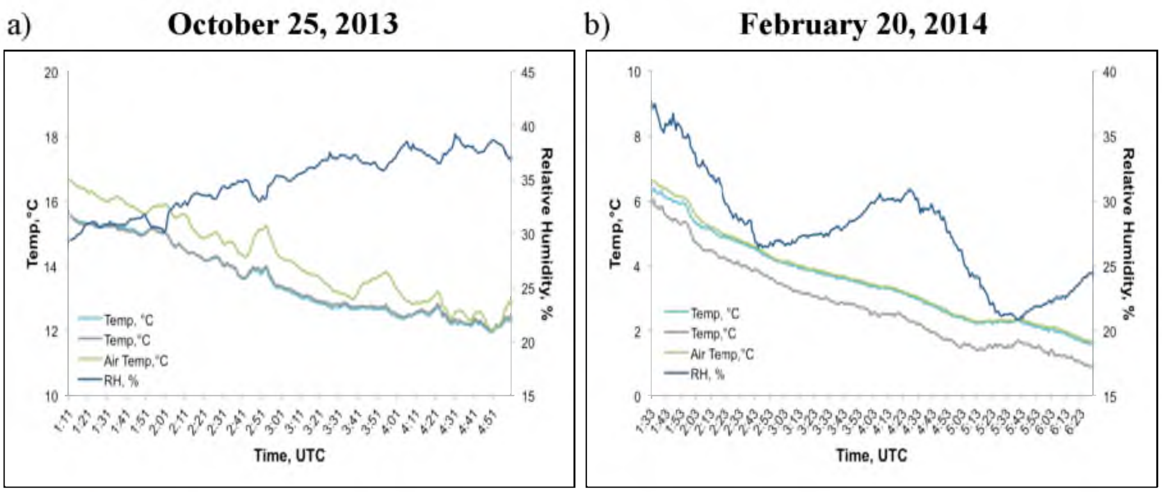

Figure A.55 Plot of the rock temperature, air temperature, and relative humidity for the entire test: a) on October 25, 2013, b) on February 20, 2014.

A.6.3 Ambient Vibration Spectra

Figure A.56a shows 3-component power spectra from the active sensor for 1 h from the October test and Figure A.56b shows 3-component power spectra from the active sensor for 1 h from the February test. Results reveal a lack of pronounced spectral peaks in even the clearest ambient vibration data, rendering further analysis unnecessary.

A.6.4 Interpretation and Discussion

We were surprised to see that the quality of the data decreased with the windy test. We had hypothesized that the lack of spectral peaks was due to low amplitude vibration from the arch. Therefore, we anticipated that strong winds would excite the feature and provide us with useable data. Unfortunately, this was not the case. Interestingly, the reference sensor shows the appearance of strong spectral peaks from a large sandstone tower roughly 20 m away. This makes the lack of peaks on the active sensor even more peculiar. We hypothesize that the weathered basal discontinuity may limit transmission of vibrations to the underlying bedrock where we measure.

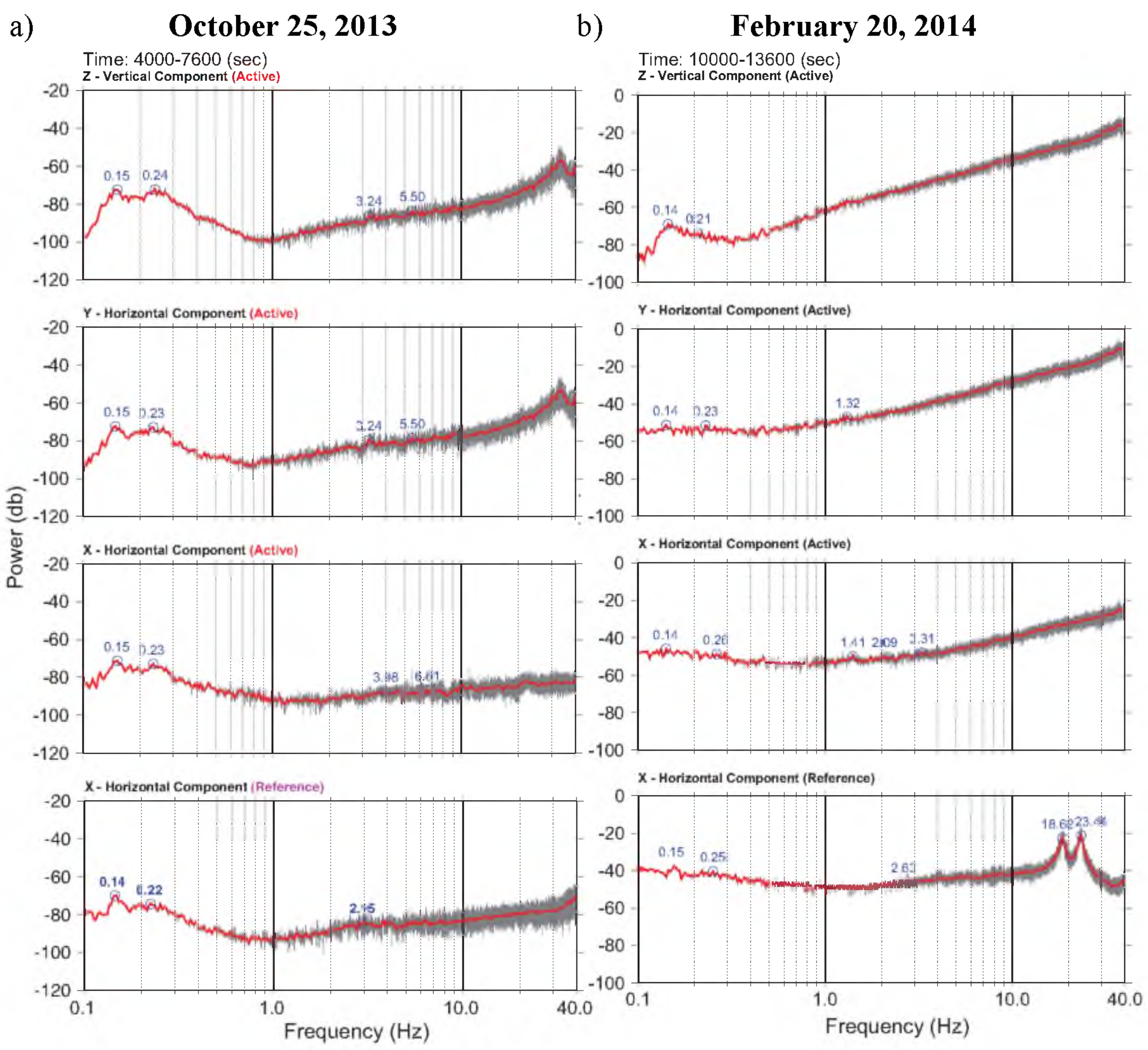

Figure A.56 Absolute power spectra for 1 h of 3-component ambient vibration data: a) from October 25, 2013, b) from February 20, 2014. Z is vertical vibration, Y is north-south horizontal, X is east-west horizontal.

A.7 Double Arch

A.7.1 Site Description

Double Arch is pair of rock shelter type natural arches, which share the same foundation at both of their outer legs (Figure A.57a). This double pothole arch formed by water erosion from atop the Entrada sandstone and is located in the Windows section of Arches National Park. The arch of interest is the east-west facing span and has developed

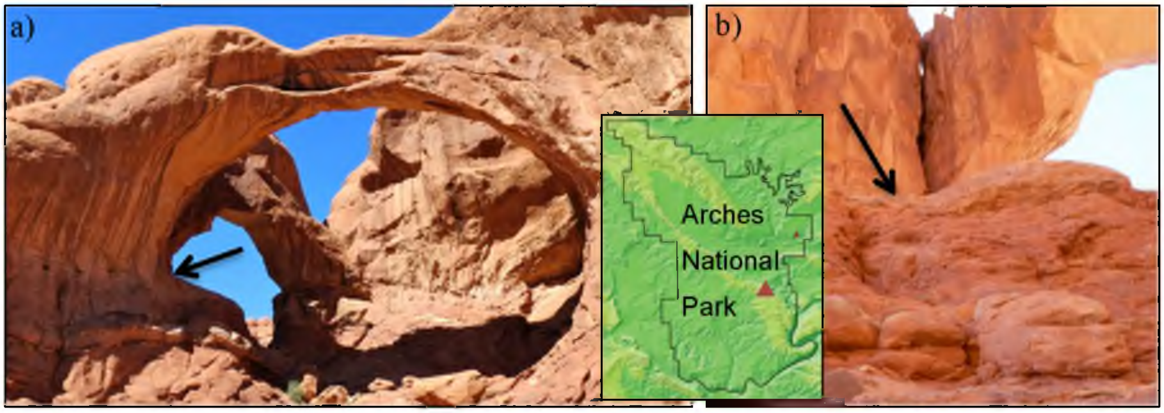

Figure A.57 Double Arch in Arches National Park, Utah: a) View of the arch with the active sensor location indicated by the black arrow. b) View of sensor location.

a large crack, causing the lower portion to sag. The crack is so large that light shines through to the other side. This crack is likely to continue to expand and eventually completely separate the slab from the arch.

A.7.2 Measurement Overview

A single test was conducted at Double Arch on November 9, 2013 for over 1.5 h. Data were collected using the site-to-reference configuration: one active sensor placed in the same position for both tests and one reference sensor located in a stable position ~100 m from the arch. Unfortunately, the top of Double Arch is inaccessible so the active sensor was placed at the base of the two spans, on top of the spire that forms the foundation (Figure A.57b). Temperature and relative humidity were also collected for the duration of the test (Figure A.58b).

A.7.3 Ambient Vibration Spectra

Figure A.59 shows 3-component power spectra from the active sensor for 1 h of the test. Results reveal several spectral peaks, but it is difficult to confidently say which feature the peaks belong to with the complexity of the double structure and being placed

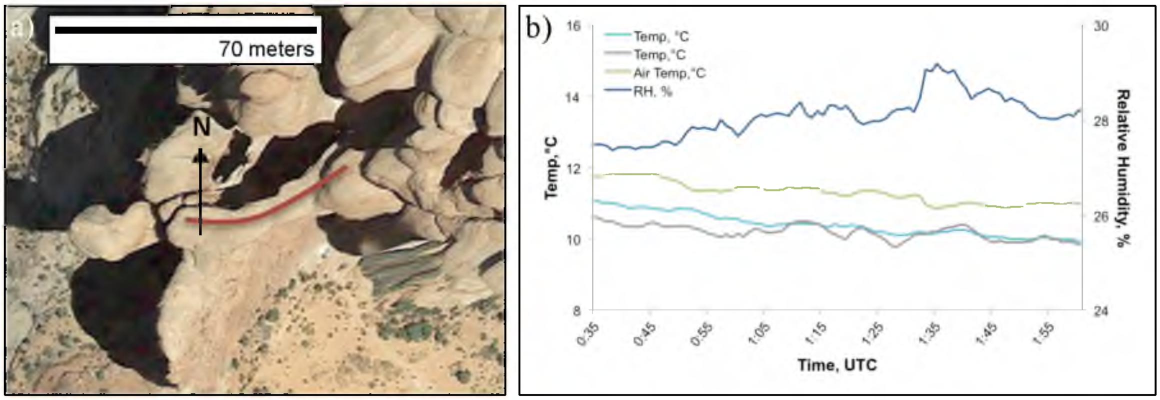

Figure A.58 Further analysis of Double Arch: a) Aerial view of Double Arch. The larger span of the arch is east-west to north-east trending. b) Plot of the rock temperature, air temperature, and relative humidity for the entire test.

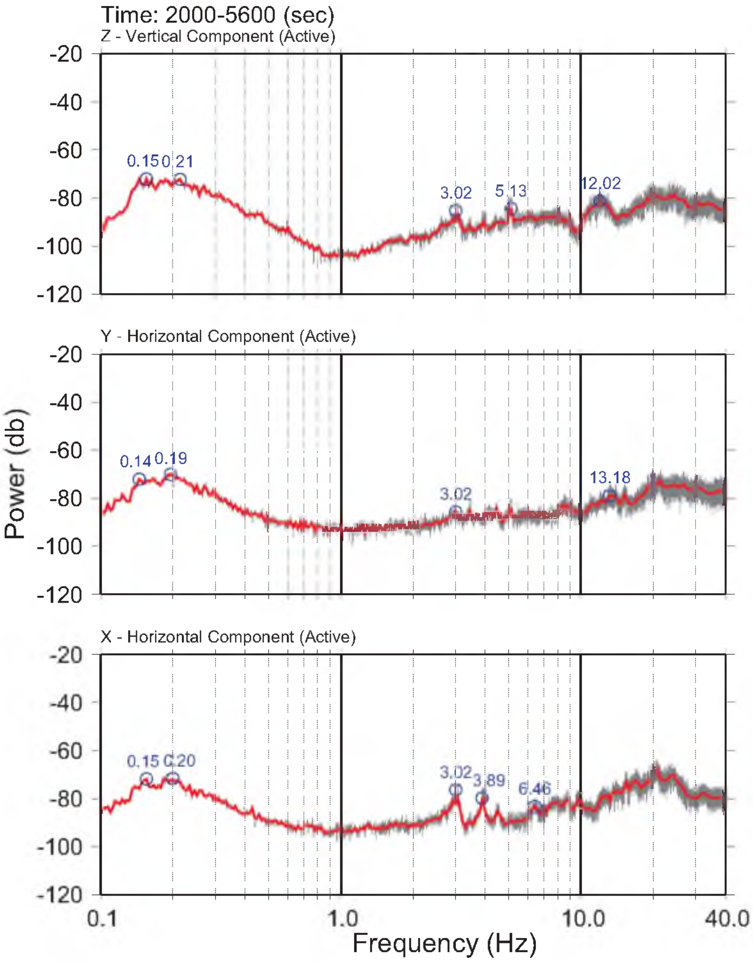

Figure A.59 Absolute power spectra for 1 h of 3-component ambient vibration data. Z is vertical vibration, Y is north-south horizontal, X is east-west horizontal. The bottom plot is east-west component of data from the reference sensor. Gray traces show raw data, red are averaged.

on a tower-like feature. Analysis shows a peak at 3.02 Hz on all components, being strongest on the east-west horizontal. This is interpreted as the first fundamental frequency. The second peak of 3.89 Hz shows up predominantly on the east-west horizontal component. The following peaks at 5.13 Hz and 6.46 Hz are less defined, with 5.13 Hz showing up on the vertical and slightly on the north-south horizontal and 6.46 Hz displayed on the east-west horizontal.

A.7.4 Polarization Results

Polarization analysis shown in Table A.14 makes it difficult to validate that the spectral peaks are representative of the feature of interest (Figure A.60). The first fundamental frequency shows up predominantly on the east-west component, but the incidence angle of 69° means that the motion leans more towards the vertical. The polarization is similar for the second frequency as well, while the third and fourth peaks do not show strong polarization.

A.7.5 Interpretation and Discussion

Double Arch is a complicated feature. The sensor location is not ideal and the additional interference causes errors and uncertainties in our data. To fully understand the resonance of this arch, it would be necessary to place a sensor directly on top. Therefore, further tests are needed before any further interpretation can be conducted.

Table A.14: Measured spectral peaks with predominant polarization orientation noted.

Measured Frequency (Hz)	Degree of Polarization	Dominant Azimuth (°)	Incidence Angle (°)
3.0	0.8	100	69
3.9	0.7	083	73
5.1	0.5	017	22
6.5	0.6	080	84

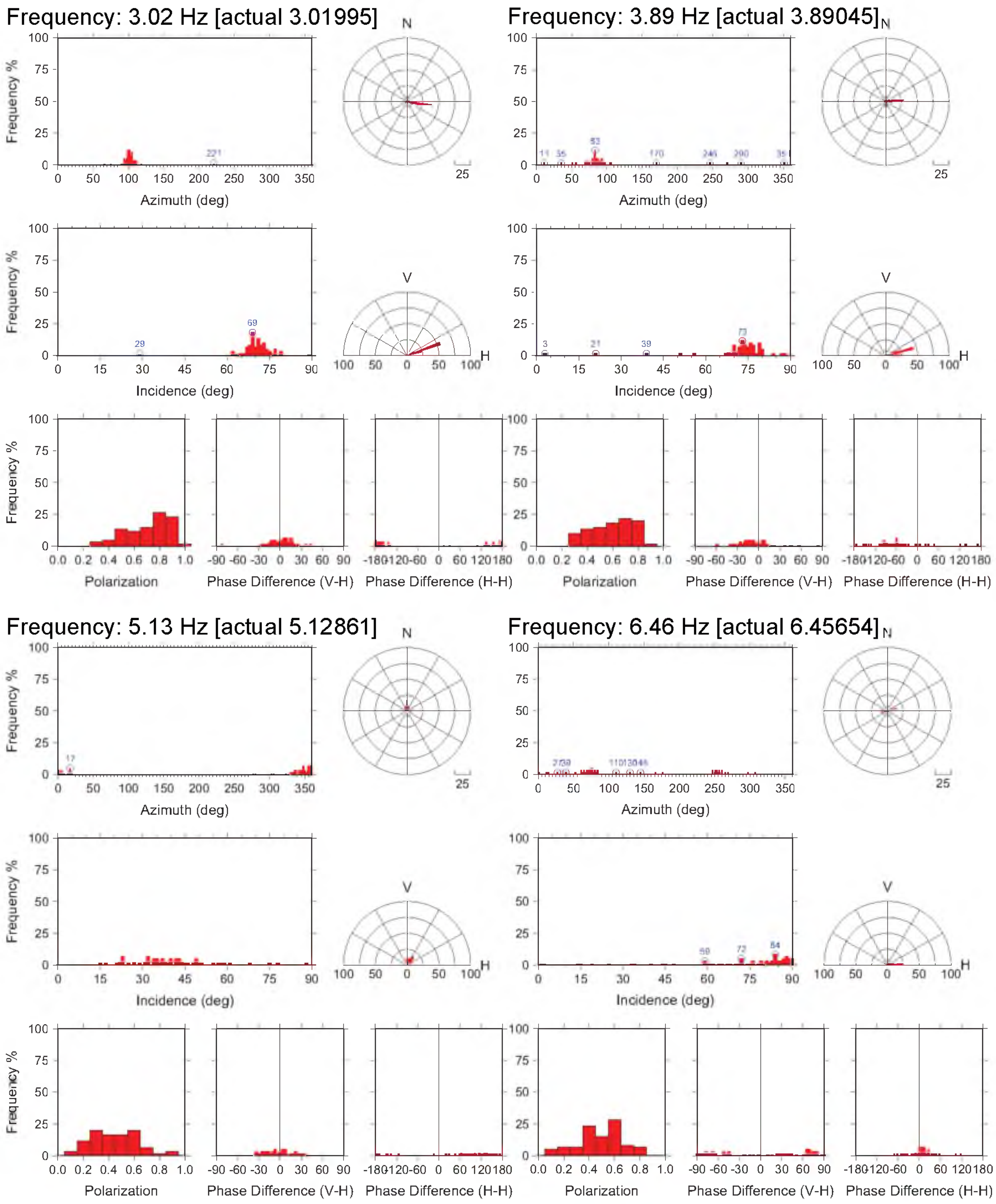

Figure A.60 Polarization plots for each measured frequency at Double Arch from the hour-long segment (2000 s – 5600 s). The plots display the azimuth, incidence angle, polarization, and phase difference between the vertical and horizontal and the two horizontal components.

A.8 Gemini Bridges

A.8.1 Site Description

Gemini Bridges is a pair of northwest trending (~315°) cave type natural arches formed by weathering through a crack into a cave (Figure A.61a,b). This formed the first opening and subsequent collapse of the cave roof formed the second opening. The feature is located on BLM land just outside of Canyonlands National Park. Contrary to the name, they are classified as natural rock arches, not natural rock bridges. Natural rock bridges are defined as features formed from the erosive action of running water and have (or once had) a flowing river present beneath the span. Gemini Bridges is situated on BLM land, and does not see the same protection as offered in the national parks. Unfortunately, people take advantage of this and a quick Internet search shows everything from people on bikes to people driving cars across the span.

A.8.2 Measurement Overview

A single test was conducted on the eastern arch of Gemini Bridges on June 18, 2014 for 1 h. Data were collected using a single active sensor placed in the center of the eastern-most span (Figure A.62a). Temperature and relative humidity were also collected for the duration of the test (Figure A.62b).

A.8.3 Ambient Vibration Spectra

Figure A.63 shows 3-component power spectra from the active sensor for 30 min of the test. Results reveal several spectral peaks on the two horizontal components, lacking any visible peaks on the vertical. Analysis shows a peak at 2.5 Hz on the two horizontals. This is interpreted as the first fundamental frequency of the eastern span.

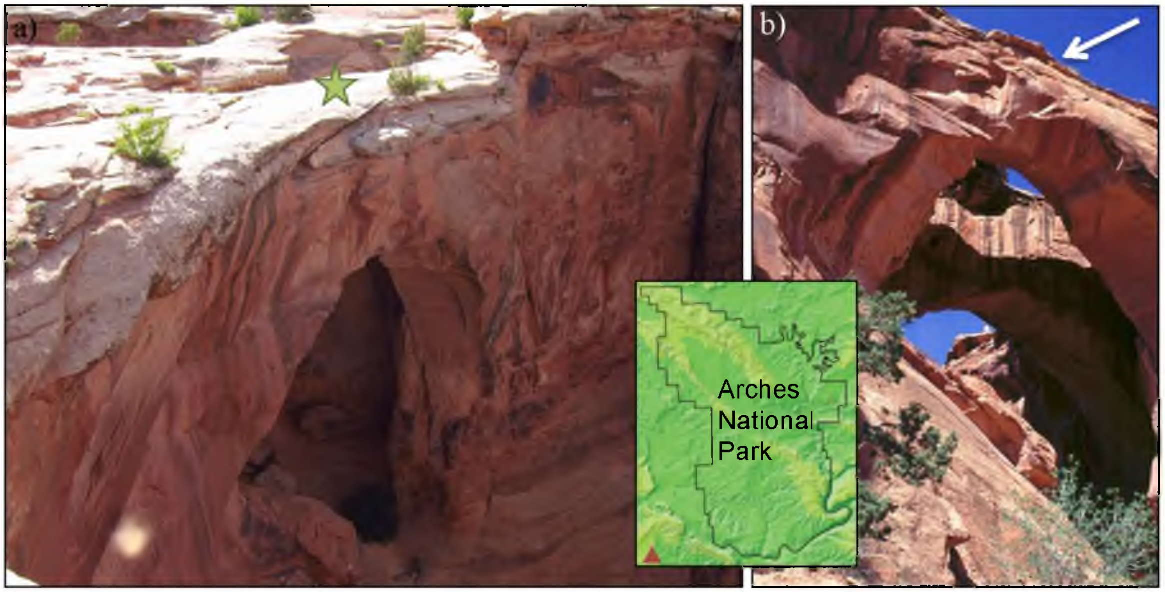

Figure A.61 Gemini Bridges on BLM land in Moab, Utah: a) The sensor is located in the middle of the natural rock arches (indicated by the blue star). b) View from underneath the arches (Berry, 2004).

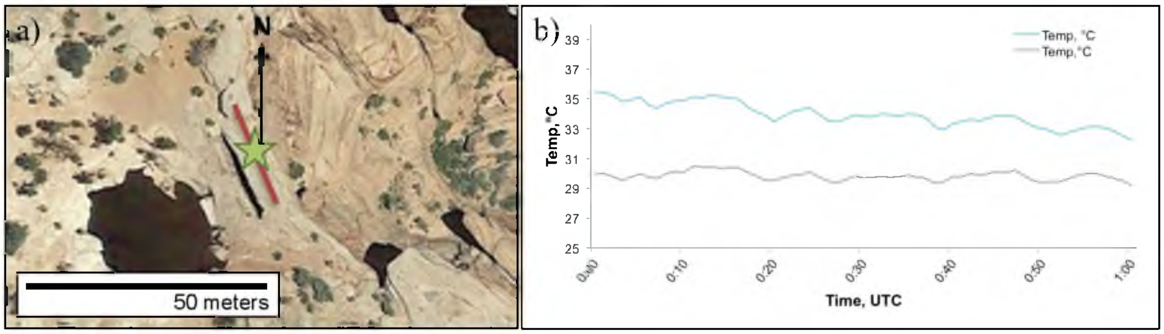

Figure A.62 Further analysis of Gemini Bridges: a) Aerial view of Gemini Bridges with the active sensor location indicated by the green star. b) Plot of the rock temperature, air temperature, and relative humidity for the entire test.

A.8.4 Polarization Results

Polarization analysis shows all four peaks have predominantly horizontal motion ranging from 80° – 89°, with azimuths ranging from 50° – 63° (Table A.15). Degree of polarization varies, with the higher frequencies (3.4 Hz, 4.2 Hz, and 6.9 Hz) having generally stronger polarization (Figure A.64).

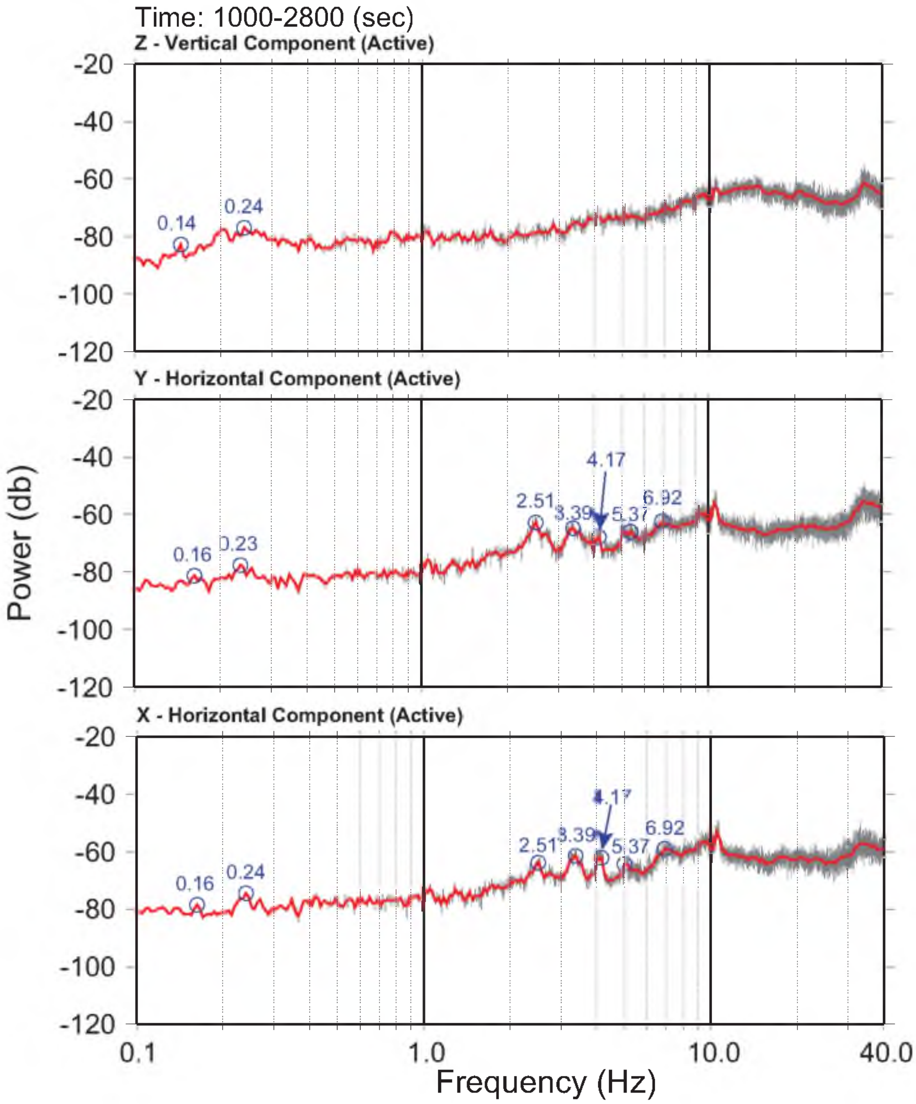

Figure A.63 Absolute power spectra for 30 min of 3-component ambient vibration data. Z is vertical vibration, Y is north-south horizontal, X is east-west horizontal. Gray traces show raw data, red are averaged.

Table A.15: Measured spectral peaks with predominant polarization orientation noted.

Measured Frequency (Hz)	Degree of Polarization	Dominant Azimuth* (°)	Incidence Angle** (°)
2.5	0.75	052	89
3.4	0.9	050	85
4.2	0.8	063	80
6.9	0.8	057	85

**Azimuth angle measured in degrees clockwise from magnetic North*

***Incidence angle measured from vertical. 0° = vertical motion, 90° = horizontal motion*

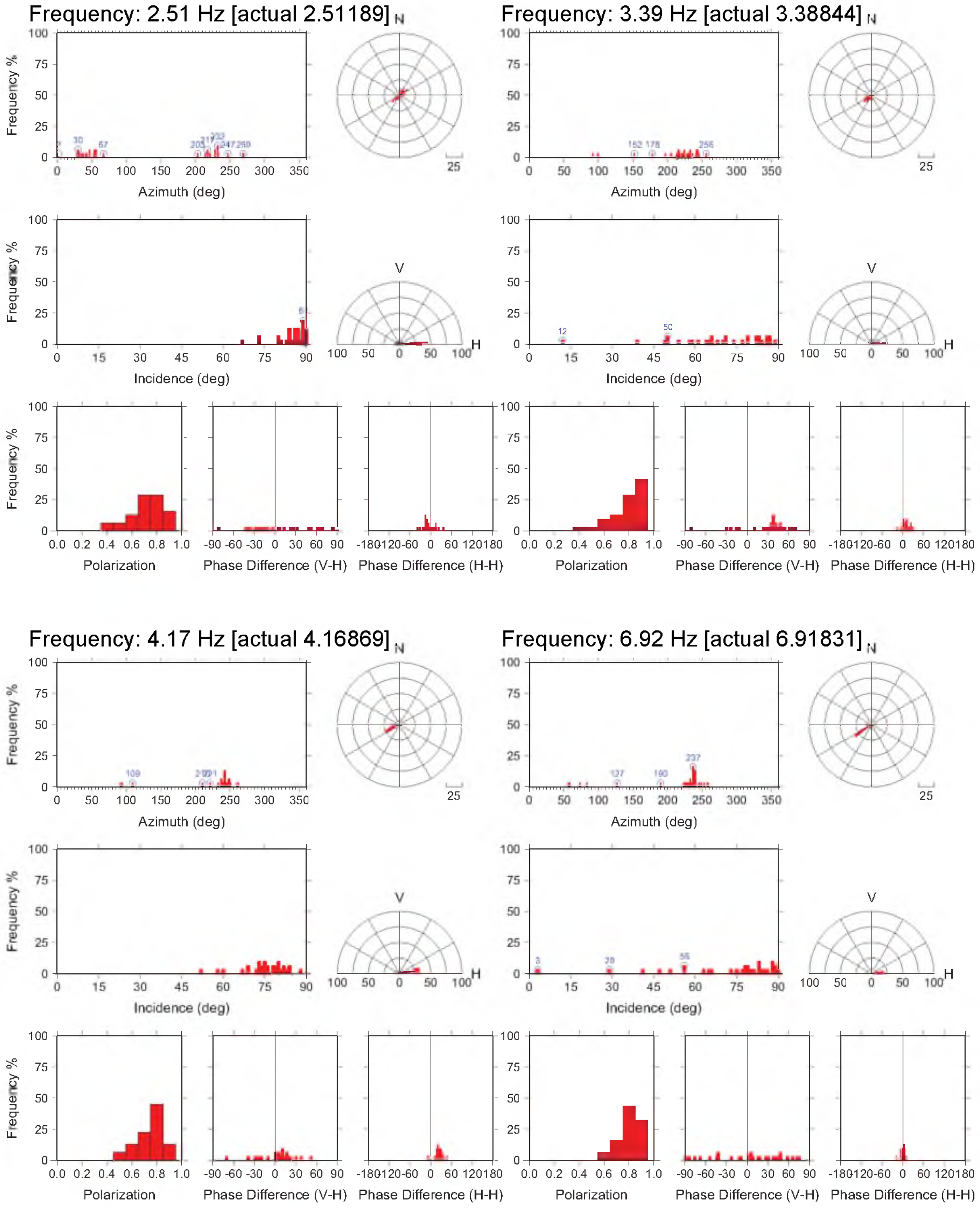

Figure A.64 Polarization plots for each measured frequency at Gemini Bridges from the 30-minute segment (1000 s – 2800 s). The plots display the azimuth, incidence angle, polarization, and phase difference between the vertical and horizontal and the two horizontal components.

A.8.5 Interpretation and Discussion

The lack of vertical peaks is not surprising with the structural nature of Gemini Bridges. The span is very thick and is connected directly to the cliff, unlike other features we measured that are freestanding or connected to a fin. Further deployments are necessary to fully understand the dynamics of this arch, but the preliminary data are promising.

A.9 North Window Arch

A.9.1 Site Description

North Window Arch is a northwest trending (~315°) rock shelter type natural arch in Arches National Park (Figure A.65). While access to the top of the arch is not permitted and sensor placement is restricted, this arch is intriguing because it is a popular destination for visitors who commonly pause and rest directly underneath the span. While the massive arch from appears stable from afar, there is a large vertical crack that cuts the fin in half and is exposed along the underside of the arch where it has trapped a few large boulders (Figure A.65). During our initial visit to the arch in July 2013, we noticed a precarious boulder that appeared likely to fall.

A.9.2 Measurement Overview

A single test was conducted at North Window Arch on November 9, 2013 for 1 h. Data were collected using the site-to-reference configuration with one seismometer placed at the base of the northern-most side of the structure and the other placed in a stable position at a distance of ~100 m for reference (Figure A.66a). Temperature and relative humidity were also collected for the duration of the test (Figure A.66b).

Figure A.65 North Window Arch in Arches National Park, Utah with the active sensor location indicated by the black arrow. A loose boulder is circled.

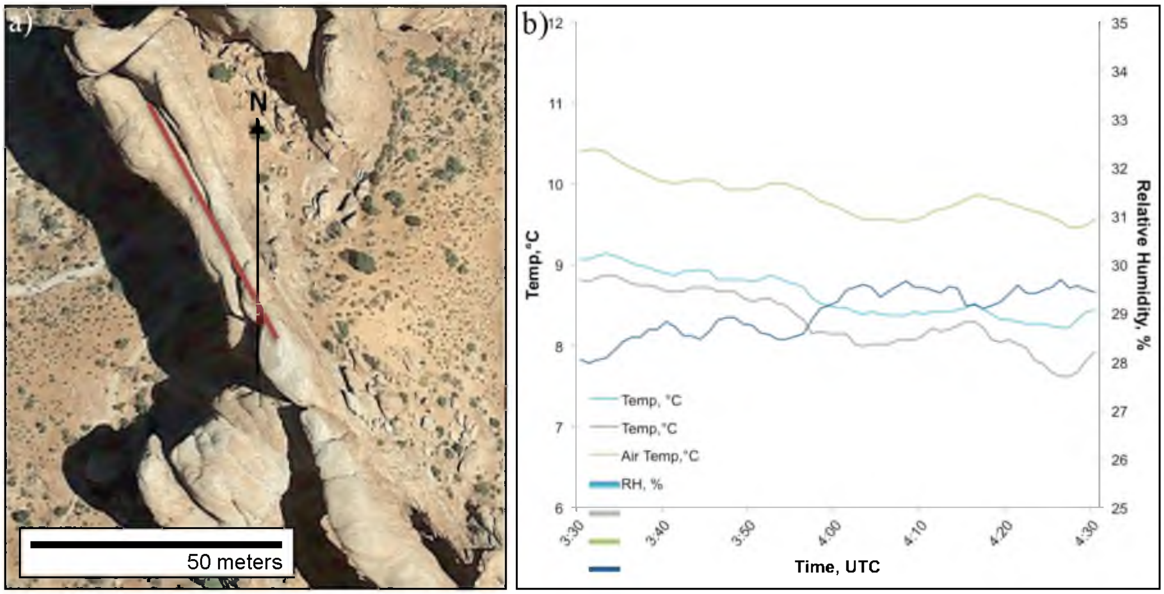

Figure A.66 Further analysis of North Window Arch: a) Aerial view of North Window Arch. It is primarily north-west trending. b) Plot of the rock temperature, air temperature, and relative humidity for the entire test.

A.9.3 Ambient Vibration Spectra

Figure A.67 shows 3-component power spectra from the active sensor for the complete hour of the test. Results reveal several weak spectral peaks on the two horizontal components, lacking any visible peaks on the vertical with strong noise ruining the data. Analysis shows peaks at 1.9 Hz and 4.5 Hz on the two horizontals.

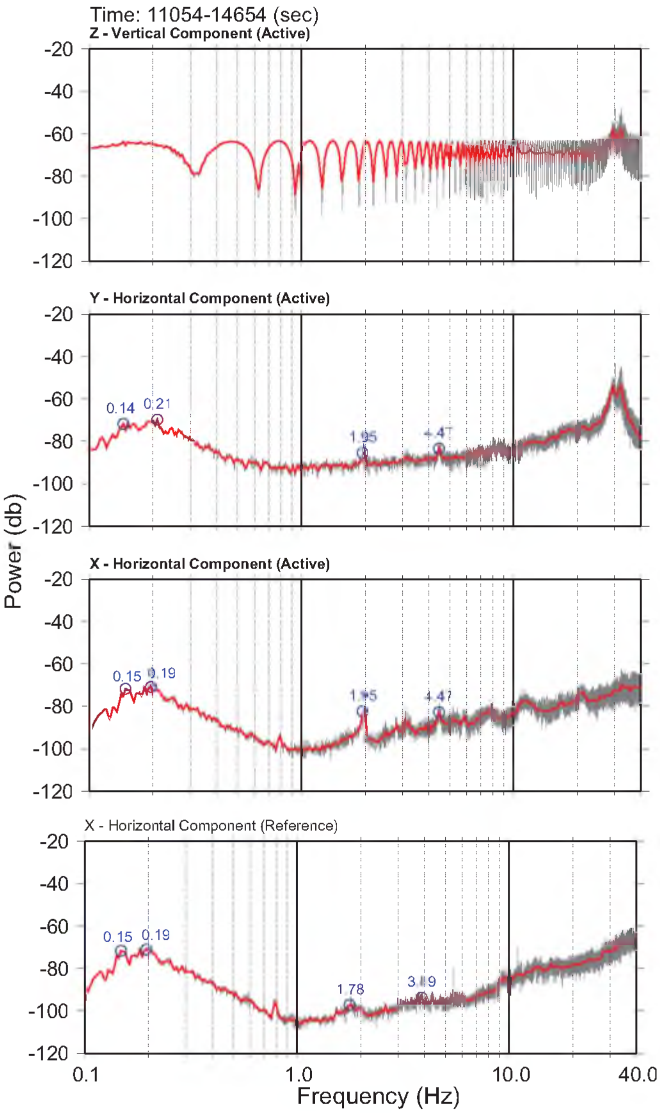

Figure A.67 Absolute power spectra for 1 h of 3-component ambient vibration data. Z is vertical vibration, Y is north-south horizontal, X is east-west horizontal. The bottom plot is east-west component of data from the reference sensor. Gray traces show raw data, red are averaged.

A.9.4 Polarization Results

The polarization plots show poor results, but are consistent with the spectra, showing the two peaks with predominantly horizontal motion of 78° and 87°, with azimuths of 057° and 051°, respectively (Table A.16 and Figure A.68).

Table A.16: Measured spectral peaks with predominant polarization orientation noted.

Measured Frequency (Hz)	Degree of Polarization	Dominant Azimuth* (°)	Incidence Angle** (°)
1.9	0.8	057	78
4.5	0.75	051	87

**Azimuth angle measured in degrees clockwise from magnetic North*

***Incidence angle measured from vertical. 0° = vertical motion, 90° = horizontal motion*

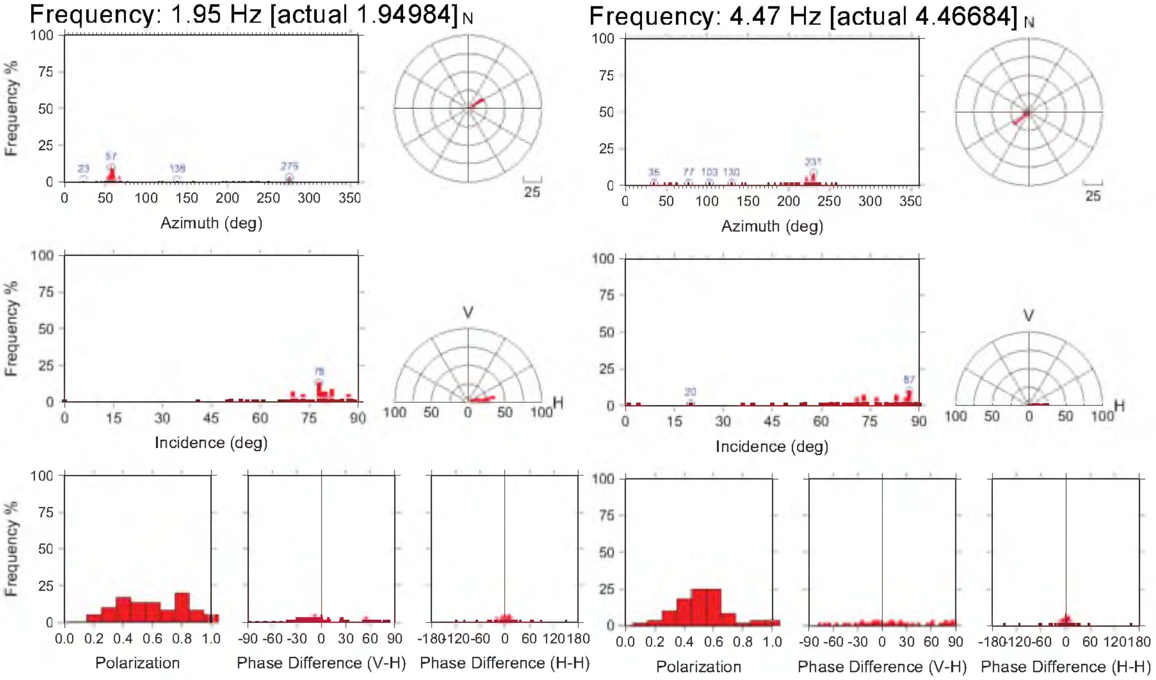

Figure A.68 Polarization plots for each measured frequency at North Window Arch from the hour-long segment (11054 s – 14654 s). The plots display the azimuth, incidence angle, polarization, and phase difference between the vertical and horizontal and the two horizontal components.

A.9.5 Interpretation and Discussion

The arch span is very thick and is part of a massive fin. It is likely that the measured peaks are representative of the fin and arch, rather than the arch alone. It is thus necessary to conduct further deployments at different locations to fully understand the dynamics of this feature. The thick geometry of the arch, however, may limit results, and different in-situ monitoring techniques along the underside crack could be more beneficial in providing data on rockfall hazards.

A.10 Surprise Arch

A.10.1 Site Description

Surprise Arch is a northwest trending (~315°) alcove type natural arch situated between two large fins in the Fiery Furnace section of Arches National Park. It appears as though this was once possibly a triple arch, with only one span currently remaining (Figure A.69a). Collapse may occur through sagging of the central span, though recent rockfall from the abutments indicates these are also susceptible to failure.

A.10.2 Measurement Overview

A single test was conducted at Surprise Arch on November 9, 2013 for over 4 h. The high concentration of fins surrounding the feature left no suitable position for a reference sensor. Therefore, data were collected using two active sensors placed along the span (Figure A.69b). Temperature and relative humidity were also collected for the duration of the test (Figure A.70b).

Figure A.69 Surprise Arch in Arches National Park, Utah: a) View of Surprise Arch from above. b) Deployment with Sensor A indicated by the blue star and Sensor B indicated by the green star.

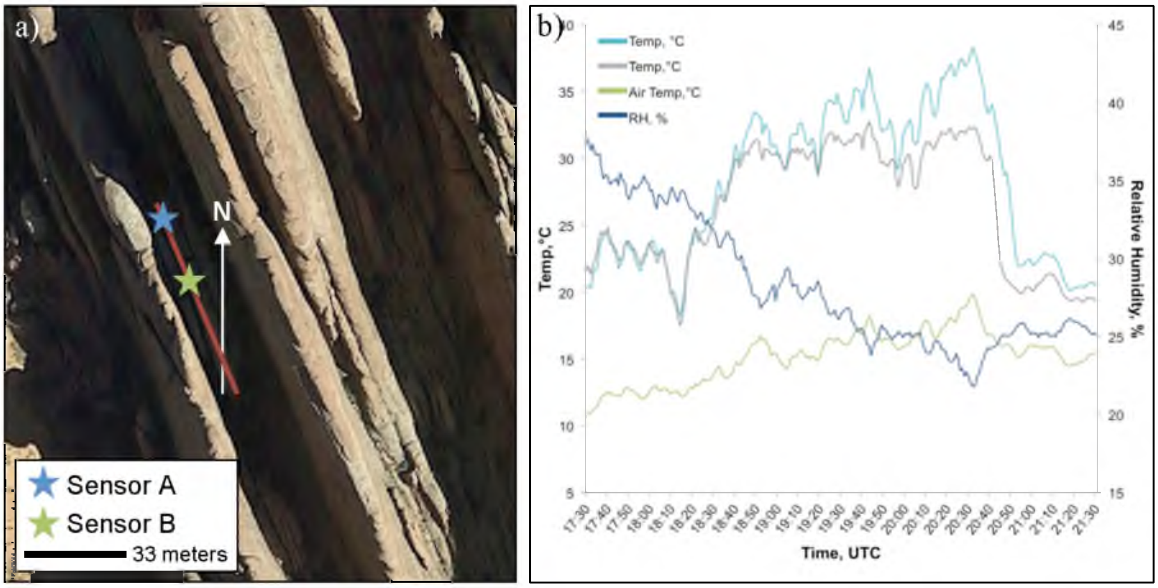

Figure A.70 Further analysis of Surprise Arch: a) Aerial view of Surprise Arch. It is primarily north-west trending. b) Plot of the rock temperature, air temperature, and relative humidity for the entire test.

A.10.3 Ambient Vibration Spectra

Figure A.71 shows 3-component power spectra from both sensors for 1 h of the test. Sensor B was placed in the center of the span and shows the clearest peaks (Figure A.71). Results reveal several spectral peaks on the two horizontal components, lacking any visible peaks on the vertical. Analysis shows a peak at 3.2 Hz on the two horizontals. This is interpreted as the fundamental frequency of the arch. Subsequent spectral peaks at 3.9 Hz, 6.3 Hz, and 8.9 Hz all show up on the two horizontal components as well.

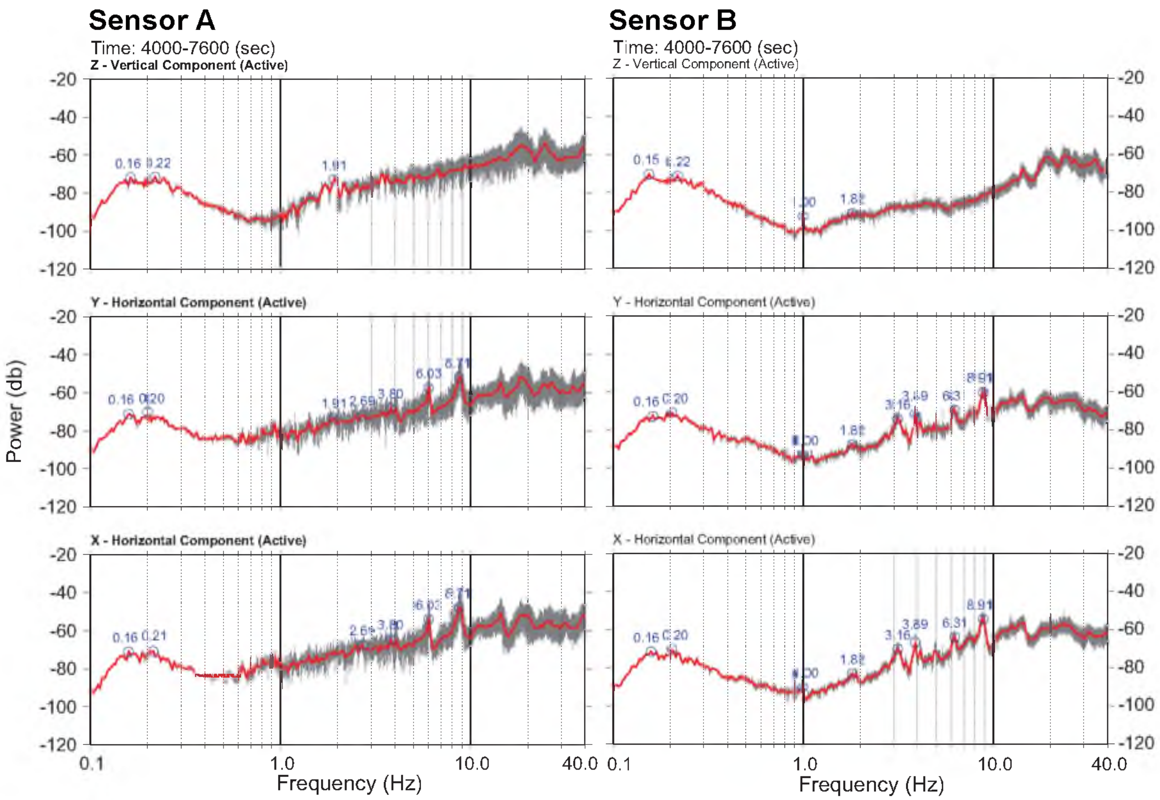

Figure A.71 Absolute power spectra for 1 h of 3-component ambient vibration data from Sensor A and Sensor B. Z is vertical vibration, Y is north-south horizontal, X is east-west horizontal. The bottom plot is east-west component of data from the reference sensor. Gray traces show raw data, red are averaged.

A.10.4 Polarization Results

Polarization analysis was computed for 1 h at Sensor B, but is representative of the entire dataset (Table A.17). Results validate the spectra, showing all four peaks with entirely horizontal motion ranging from 87° – 90°, with azimuths ranging from 058° – 063° (Figure A.72).

A.10.5 Interpretation and Discussion

The results at Surprise Arch suggest that the spectra are highly influenced by the surrounding rock fins. The lack of vertical motion that one would expect to see at this thin structure may result from the fins overwhelming the data with their predominantly horizontal motion. Future tests on a calm day with multiple sensors recording along the span of the arch may improve our interpretation and allow for further analysis.

Table A.17: Measured spectral peaks with predominant polarization orientation noted.

Measured Frequency (Hz)	**Degree of Polarization**	**Dominant Azimuth*** (°)	**Incidence Angle**** (°)
3.2	0.9	058	87
3.9	0.1	061	87
6.3	0.1	063	90
8.9	0.1	063	89

**Azimuth angle measured in degrees clockwise from magnetic North*
***Incidence angle measured from vertical. 0° = vertical motion, 90° = horizontal motion*

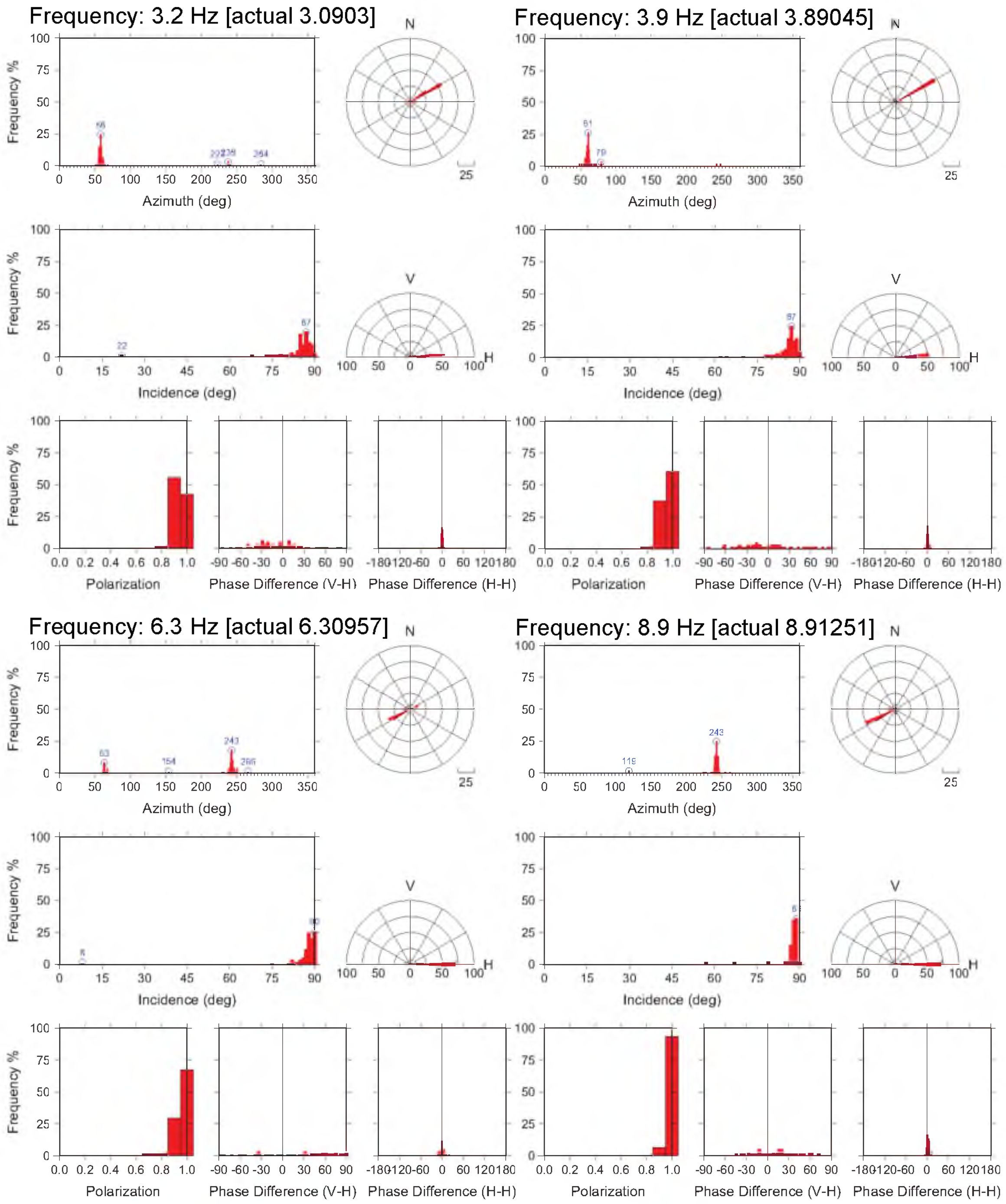

Figure A.72 Polarization plots for each measured frequency at Surprise Arch from the hour-long segment (4000 s – 7600 s) from Sensor B. The plots display the azimuth, incidence angle, polarization, and phase difference between the vertical and horizontal and the two horizontal components.

APPENDIX B

MEASUREMENT DETAILS AND METEOROLOGICAL CONDITIONS

Table B.1: Complete table with measurement details and meteorological conditions for every deployment from 2013 – 2014.

Site Name	*Measurement Start Date/Time (UTC)*		*Duration (H:M:S)*	*Reference Y/N?*	*Data File Name Active/Reference*		*Mean Rock Temp (°C)*	*Mean Air Temp (°C)*	*Meteo. Conditions*
Corona Arch	8/16/13	13:09:38	4:50:21	Y	A1COR_20130816	B1COR_20130816	N/A	27	Hot, clear skies
Corona Arch	8/17/13	2:41:27	12:18:32	Y	A1COR_20130817	B1COR_20130817	N/A	21	Clear, warm
Mesa Arch	9/28/13	2:43:15	5:21:57	Y	A1MA_20130928	B1MA_20130928	6.59	6.37	Clear, wind gusts
Balanced Rock	9/29/13	1:44:21	5:45:38	Y	A1BR_20130929	B1BR_20130929	13.7	12.67	Calm
Delicate Arch	10/25/13	1:11:57	3:48:02	Y	A1DEL_20131025	B1DEL_20131025	13.26	14.24	Calm, warm, clear
Double O Arch	10/25/13	21:41:34	2:48:25	ON ARCH	EDUBO_20131025	WDUBO_20131025	20.79	17.72	Calm, hot, clear
Double Arch	11/9/13	0:25:45	1:34:14	Y	ADUB_20131109	BDUB_20131109	10.51	11.48	Calm, cool
N. Window Arch	11/9/13	3:29:59	1:00:00	Y	AWIN_20131109	BWIN_20131109	8.47	9.85	Calm, cool
Surprise Arch	11/9/13	17:12:29	4:17:30	Y	ASUR_20131109	BSUR_20131109	26.36	14.74	Calm, warm, sunny
Mesa Arch	12/13/13	23:30:00	1:00:00	Y	AMA_20131213	BMA_20131213	12.77	-5.98	Cold, snow-covered
Delicate Arch	2/20/14	1:33:43	4:56:16	Y	ADEL_20140220	BDEL_20140220	3.15	3.58	Very windy
Mesa Arch	2/20/14	20:36:00	0:53:59	Y	AMA_20140220	BMA_20140220	7.83	3.68	Calm
Mesa Arch	4/13/14	1:20:00	0:42:00	ON ARCH	AMACC_20140413	BMACC_20140413	15.51	14.2	Calm
Mesa Arch	5/5/14	18:03:33	61:26:26	Y	AMA3_20140505	BMA3_20140505	18.23	14.85	---
Double O Arch	5/20/14	19:16:00	2:25:00	N	WDUBO_20140520	N/A	35.99	27.48	Sunny
Landscape Arch	5/21/14	18:01:00	3:28:00	N	LAND_20140521	N/A	29.59	24.59	Sunny
Mesa Arch	6/16/14	22:42:00	1:33:00	Y	AMA_20140616	BMA_20140616	34.35	20	Sunny
Gemini Bridges	6/18/14	0:00:00	1:00:00	N	GEME_20140618	N/A	N/A	20	Sunny, windy
Mesa Arch	8/20/14	3:50:00	1:10:00	N	AMAS_20140820	N/A	15.97	14.9	Saturated, earthquake
Mesa Arch	10/28/14	19:30:00	2:00:00	ON ARCH	AMA_20141028	BMA_20141028	25.24	14.96	Calm, sunny

REFERENCES

Arches National Park, 2007: <http://www.viamagazine.com/destinations/arches-national-park> (accessed February 20, 2015).

Baars, D. L., 1993, Canyonlands Country: Geology of Canyonlands and Arches National Parks: Salt Lake City, p. 138.

Berry, G., 2004, Gemini Bridges: <http://www.naturalarches.org> (accessed February 20, 2015).

Bottelin, P., C. Lévy, L. Baillet, D. Jongmans, and P. Guéguen, 2013, Modal and thermal analysis of les arches unstable rock column (vercors massif, french alps): Geophysical Journal International, v. 194, p. 849–858, doi:10.1093/gji/ggt046.

Burjánek, J., G. Gassner-Stamm, V. Poggi, J. R. Moore, and D. Fäh, 2010, Ambient vibration analysis of an unstable mountain slope: Geophysical Journal International, v. 180, p. 820–828, doi:10.1111/j.1365-246X.2009.04451.x.

Clinton, J. F., S. C. Bradford, T. H. Heaton, and J. Favela, 2006, The observed wander of the natural frequencies in a structure: Bulletin of the Seismological Society of America, v. 96, no. 1, p. 237–257, doi:10.1785/0120050052.

Connors, T., 2008, Fallen Arch: <http://www.geotimes.org> (accessed September 3, 2013).

Cruikshank, K. M., and A. Aydin, 1995, Unweaving the joints in Entrada Sandstone, Arches National Park, Utah, U.S.A.: Journal of Structural Geology, v. 17, no. 2, p. 409–421, doi:10.1016/0191-8141(94)00061-4.

Foos, A., 1999, Geology of the moab region: Geology.

Graham, J., 2004, Geologic Resource Evaluation Report: Denver, 55 p.

Koper, K. D., and V. L. Hawley, 2010, Frequency dependent polarization analysis of ambient seismic noise recorded at a broadband seismometer in the central United States: Earthquake Science, v. 23, p. 439–447, doi:10.1007/s11589-010-0743-5.

Lévy, C., L. Baillet, D. Jongmans, P. Mourot, and D. Hantz, 2010, Dynamic response of the Chamousset rock column (Western Alps, France): Journal of Geophysical Research: Earth Surface, v. 115, no. November 2009, p. 1–13, doi:10.1029/2009JF001606.

Matthews, N. a., 2008, Aerial and Close-Range Photogrammetric Technology: Providing Resource Documentation, Interpretation, and Preservation: Technical Note 428, p. 42.

Moore, J. R., V. Gischig, J. Burjanek, S. Loew, and D. Fäh, 2011, Site effects in unstable rock slopes: Dynamic behavior of the Randa instability (Switzerland): Bulletin of the Seismological Society of America, v. 101, no. 6, p. 3110–3116, doi:10.1785/0120110127.

Park, J., F. L. Vernon, and C. R. Lindberg, 1987, Frequency dependent polarization analysis of high-frequency seismograms: Journal of Geophysical Research, v. 92, no. 12, p. 664–674.

Sohn, H., C. R. Farrar, F. Hemez, and J. Czarnecki, 2002, A Review of Structural Health Monitoring Literature 1996 – 2001: Third World Conference on Structural Control, p. 1–7.

Stokes, W. L., 1986, Geology of Utah: 305 p.

Stubbs, I. R., and V. R. McLamore, 1973, The abient vibration survey, *in* Proceedings of Fifth World Conference on Earthquake Engineering: p. 286–289.

Sufri, O., K. D. Koper, R. Burlacu, and B. de Foy, 2013, Microseisms from Superstorm Sandy: Earth and Planetary Science Letters, v. 402, p. 324–336, doi:10.1016/j.epsl.2013.10.015.

Vreeland, R. H., 1977, Nature's Bridges and Arches: Arches National Park, Utah: v. 2, p. 124.

Vreeland, R. H., 1987, Nature's Bridges and Arches: Central Canyonlands National Park, Utah: 87 p.

Vreeland, R. H., 1976, Nature's Bridges and Arches: Vicinity of Moab, Utah: 99 p.

Wilbur, J. H., n.d., Landscape Arch: <http://www.naturalarches.org> (accessed February 22, 2015).

Zhang, J., P. Gerstoft, and P. M. Shearer, 2009, High-frequency P-wave seismic noise driven by ocean winds: Geophysical Research Letters, v. 36, no. April, p. 1–5, doi:10.1029/2009GL037761.